

3D multi-scale finite element analysis of the crustal state of  
stress in the Western US and the Eastern California Shear  
Zone, and implications for stress – fluid flow interactions for  
the Coso Geothermal Field

Zur Erlangung des akademischen Grades eines  
**DOKTORS DER NATURWISSENSCHAFTEN**

von der Fakultät für Physik der  
Universität Karlsruhe (TH)  
genehmigte

**DISSERTATION**

von  
Dipl.-Geophys. Andreas Eckert  
aus Würzburg

Tag der mündlichen Prüfung:

9. November 2007

Referent:

Prof. Dr. Friedemann Wenzel

Korreferent:

Prof. Dr. Karl Fuchs



---

## Table of contents

Table of contents .....	III
I. Terminology .....	VI
I.i. Technical abbreviations .....	VI
I.ii. Regional abbreviations.....	VI
II. Acknowledgements.....	VII
III. Abstract .....	IX
IV. Deutsche Zusammenfassung.....	XI
1. Introduction .....	1
1.1. Purpose of the work .....	1
1.2. Questions to be addressed .....	1
1.3. Approach used .....	1
1.3.1. Multi-scale modeling – Submodeling approach.....	1
1.3.2. Loading procedure and model calibration .....	3
1.3.3. Fault modeling .....	3
1.3.4. Modeling processes - Software used .....	4
1.3.5. Computation .....	4
2. Theory .....	7
2.1. The stress tensor .....	7
2.2. Principal stresses .....	8
2.3. Mean stress .....	8
2.4. Differential stress.....	8
2.5. Mohr circle of stress .....	8
2.6. Fracture Potential (FP) .....	10
2.6.1. Fracture potential in the shear regime (sFP).....	11
2.6.2. Fracture potential in the tensile regime (tFP) .....	12
2.7. Regime-Stress-Ratio (RSR).....	12
2.8. Finite Element modeling .....	13
2.8.1. Equations of equilibrium .....	13
3. Finite Element modeling of tectonic stresses .....	17
3.1. Introduction .....	17
3.2. Analysis and prediction of the horizontal state of crustal stress.....	17
3.3. Numerical modeling of in-situ stresses .....	19
3.3.1. Technical problems .....	20
3.3.2. Solution proposed for the limitations of a 3D rectangular box model .....	22
3.3.3. Summary of the pre-stressing procedure .....	24
3.4. Summary and discussion .....	24
4. Crustal state of stress in California and the role of the San Andreas Fault.....	27
4.1. Scope .....	27
4.2. Introduction .....	27
4.3. Californian stress field.....	28
4.4. Model.....	28
4.5. Loading procedure.....	29
4.6. Results .....	31
4.6.1. Application of 'gravity only' to the model (Figure 4.3a,b).....	31
4.6.2. Pacific Plate motion analysis.....	31
4.7. GPE – tectonic loading interaction.....	35
4.8. Model without topography .....	35
4.9. Discussion.....	37

---

---

4.10. Conclusions .....	39
5. The coefficient of friction on the SAF and its impact on stress orientations .....	41
5.1. Introduction .....	41
5.2. Other modeling studies.....	42
5.3. Model .....	43
5.3.1. Model limitations .....	43
5.4. Impact of $\mu$ on $S_H$ orientations .....	43
5.5. Shear stress on the SAF .....	45
5.6. Discussion and conclusions.....	46
6. State of stress in the Eastern California Shear Zone (ECSZ).....	47
6.1. Submodeling study at the ECSZ scale .....	47
6.2. Introduction .....	47
6.2.1. Tectonic setting of the Owens Valley Fault .....	48
6.3. ECSZ model setup.....	49
6.3. Sheorey calibration.....	51
6.4. Loading procedure.....	52
6.4.1. Tectonic stressing .....	52
6.4.2. “Displacement” analysis .....	54
6.4.3. GPS based tectonic loading.....	57
6.5. Fracture Potential .....	59
6.6. State of stress in the ECSZ .....	59
6.6.1. State of stress of the Owens Valley Fault and the Coso Range .....	60
6.7. Discussion .....	61
6.8. Conclusions .....	63
7. State of stress in the Coso Range .....	65
7.1. Introduction .....	65
7.1.1. Structure and faulting .....	65
7.1.2. Seismicity .....	66
7.2. Model construction.....	68
7.3. Loading procedure.....	70
7.3.1. Sheorey calibration.....	70
7.3.2. Tectonic loading submodel analysis - Model calibration.....	71
7.3.3. State of stress in the Coso Range after displacement loading submodel analysis .....	73
7.4. State of stress for the Coso Geothermal Field.....	75
7.5. Conclusions .....	78
8. Fracture networks and fluid flow pathways for the Coso Geothermal Field .....	79
8.1. Introduction .....	79
8.2. Fracture networks .....	79
8.3. Fracture Potential (FP) in the Coso Range .....	80
8.4. Second order structures .....	84
8.5. Discussion of fracture analysis.....	89
8.6. Mean stress derived fluid flow networks for the Coso Geothermal Field .....	89
8.7. 2 <sup>nd</sup> order fractures and fluid flow .....	94
8.8. Discussion and conclusions.....	95
9. Synthesis and discussion of the thesis.....	97
9.1. Goal of the thesis.....	97
9.2. Numerical methodology .....	97
9.3. Model calibration .....	98
9.4. Modeling results .....	99

---

---

9.4.1. SAF scale.....	99
9.4.2. ECSZ scale .....	99
9.4.3. Coso Range scale.....	100
9.5. Discussion.....	101
9.5.1. SAF and ECSZ scale .....	101
9.5.2. Coso Range scale.....	104
9.6. Main conclusions.....	106
9.7. Drawbacks and improvements.....	106
9.8. Summary and concluding remarks .....	107
10. References .....	109

### I. Terminology

Here, a short summary of the most frequently used abbreviations in the text is given.

#### I.i. Technical abbreviations

$\Delta GPE$	gravitational potential energy differences
GPE	gravitational potential energy
FP	Fracture Potential (chapter 2.6)
sFP	shear Fracture Potential (chapter 2.6)
tFP	tensile Fracture Potential (chapter 2.6)
R	stress ratio (chapter 2.7)
RSR	Regime-Stress-Ratio (chapter 2.7)
$S_H$	maximum horizontal stress component
$S_h$	minimum horizontal stress component
$S_V$	vertical stress component
$\sigma_d$	differential stress
$\sigma_m$	mean stress

#### I.ii. Regional abbreviations

ALFZ	Airport Lake Fault Zone
BB	Big Bend
B&R	Basin and Range
CGF	Coso Geothermal Field
CR	Coso Range
CWF	Coso Wash Fault
DVF	Death Valley Fault
ECSZ	Eastern California Shear Zone
GF	Garlock Fault
GV	Great Valley
HMF	Hunter Mountain Fault
IVW	Indian Wells Valley
MB	Mojave Block
NA	North America
OVF	Owens Valley fault
PP	Pacific Plate
PVF	Panamint Valley Fault
SAF	San Andreas Fault
SN	Sierra Nevada
WHMF	Wild Horse Mesa Fault
WUS	Western United States

## **II. Acknowledgements**

Bei Prof. Dr. F. Wenzel möchte ich mich für die Betreuung der Arbeit, sowie für seine Unterstützung und sein Vertrauen bedanken.

Prof. Dr. K. Fuchs möchte ich für die Übernahme des Korreferates und einen kritischen Blick über die Arbeit danken.

Especially, I would like to thank Peter Connolly for all his support, enthusiasm and interest for my work and for all the inspiring discussions about Coso and many more things.

Furthermore, I want to thank the US Navy and the Geothermal Program Office for funding this project and especially F.C. Monastero for all the interesting discussions and information on the ECSZ and Coso.

Des weiteren möchte ich allen Mitgliedern der Spannungsgruppe für eine angenehme Arbeitsatmosphäre und ihre Unterstützung danken. Darüber hinaus danke ich Andreas Barth, Oliver Heidbach, Gwendolyn Peters und Jose Dirkzwager für viele interessante Diskussionen. Tobias Hergert möchte ich für seine Unterstützung und Bereitstellung der Spannungsdaten für chapter 3 danken.

Besonderer Dank gilt Thies Buchmann für all die interessanten und erhellenden Diskussionen, sowie für seine Hilfe bei zahlreichen „modellier“-technischen Problemen.

Zum Schluss gilt mein ganz besonderer Dank meiner Familie und meinen Freunden, die mir vor allem durch ihre moralische Unterstützung während der gesamten Promotionszeit sehr geholfen haben.



### III. Abstract

The three dimensional (3D) Western US crustal state of stress and in particular the Pacific - North American plate boundary represent an interesting example for studying the interaction of tectonic loading and internal gravitational stresses. In this thesis linear elastic 3D Finite Element models are used to conduct a multi-scale analysis of the crustal state of stress. The multi-scale modeling approach enables the integration of large scale tectonic processes of the San Andreas Fault system to local, small scale processes of the Eastern California Shear Zone (ECSZ) and the Coso Geothermal Field (CGF) in the Coso Range. This is accomplished by using the Abaqus submodeling procedure, in which results from large scale models are used as boundary conditions for local, small scale models.

An important process in numerically modeling the 3D state of stress is the implementation of an initial gravitationally equilibrated state of stress, in which realistic horizontal stress magnitudes are obtained. The modeling approach presented in this thesis calibrates this initial state of stress to a model, in which horizontal stresses near surface become larger than the vertical stress. After this calibration the state of stress is subjected to tectonically derived loads to generate a close approximation of the full crustal state of stress.

On the scale of the SAF focus is placed on how (1) gravitational potential energy differences ( $\Delta GPE$ ) from topography, (2) plate boundary forces and (3) fault geometries influence the 3D crustal state of stress. Comparison to independent stress orientations, magnitudes and observed tectonic regimes shows that the modeling approach reproduces the absolute crustal state of stress. The modeling results suggest that topography induced  $\Delta GPE$  determine and define provinces of different tectonic regimes which are further developed by Pacific Plate motion. In particular, plate boundary forces transferred over the SAF have only minor influence on the near fault state of stress but have a strong impact on the regional stress field. Omitting  $\Delta GPE$  in 3D modeling studies does yield realistic stress orientations but the stress magnitudes and dependent variables such as tectonic regimes do not match independent observations. The geometrical impact of the bending segment of the SAF results in increased horizontal stresses in the Mojave Block and transfers strike-slip tectonics into the Eastern California Shear Zone to accommodate a part of the relative plate motion.

The calibrated state of stress for the SAF system is used to investigate the frictional strength of the SAF, which is the object of a controversy debate. The impact of the coefficient of friction,  $\mu$ , on the resulting stress orientations is analyzed by a sensitivity analysis with  $\mu$  ranging from 0.1 to 1.0. The modeling results indicate that  $\mu$  has only a minor impact on  $S_H$  orientations. The difference between a weak fault scenario and a strong fault scenario is less than  $5^\circ$  in the far-field, i.e. for distances greater than 10 km from the fault, and in the range of  $0^\circ$ - $10^\circ$  on the fault surface. This may indicate that using  $S_H$  orientation data is not an adequate approach to infer the strength of the San Andreas Fault.

The state of stress in the ECSZ is characterized by a transition of strike-slip and extensional tectonics. The modeling results obtain a state of stress in the ECSZ

characterized by transtensional tectonic regimes with the major active faults being situated in corridors of strike-slip tectonics. The influence of the SAF geometry by using the ABAQUS submodeling technique is necessary to generate the observed state of stress since boundary conditions derived from contemporary GPS displacements do not generate sufficient horizontal stress magnitudes to result in bulk transtension in the ECSZ.

The efficiency of geothermal energy production at the Coso Geothermal Field in eastern California is reliant on the knowledge of fluid flow directions associated with fracture networks. The mean and differential stress distributions are used to infer fluid flow vectors and second order fracture likelihood and orientation. The results show that the Coso Range and adjacent areas are regions of increased likelihood of second order fracture generation associated to tectonic boundary forces. The mean stress distribution indicates that the geothermal field occurs in a favorable location for fluid through-flow locally derived from the north and west, but more regionally from the Sierra Nevada, and that fluid storage may occur at the southern end of the Coso Wash Fault. Predicted second order structures either support or constrain fluid flow. This indicates the importance of fracture networks for fluid migration in tectonically active regions such as the Coso Range.

## IV. Deutsche Zusammenfassung

### Einleitung

Die plattentektonischen Prozesse im Westen der USA, und speziell das System der San Andreas Störung (SAF) und ihre Interaktion mit der Eastern California Shear Zone (ECSZ), repräsentieren ein exzellentes Beispiel um die Beiträge verschiedener Prozesse zum dreidimensionalen (3D) Spannungszustand zu untersuchen. Der 3D Spannungszustand in der Erdkruste liefert zum einen wichtige Hinweise bezüglich großräumiger, geodynamischer Prozesse, als auch zur Optimierung von Explorationsprozessen in Erdöl- und geothermischen Lagerstätten. Das Coso Geothermal Field (CGF) in der Coso Range befindet sich entlang einer der aktivsten Störungen innerhalb der ECSZ und Deformationsprozesse innerhalb der Coso Range werden mit tektonischen Randbedingungen assoziiert. Numerische Methoden, wie z.B. die Finite Elemente (FE) Methode, bieten die Möglichkeit, den Spannungszustand sowohl großräumiger tektonischer Prozesse, als auch den einer Lagerstätte innerhalb eines aktiven tektonischen Systems zu modellieren. Vorteil der FE Methode ist es, komplexe Geometrien von Störungen und lithologische Stratigraphien mit beliebigem Materialverhalten und komplexen Randbedingungen zu verknüpfen.

Ziel dieser Arbeit ist zum einen die Erstellung einer Serie von linear elatischen FE Modellen, von der Skala der SAF bis hin zur Skala des CGF, um den kompletten Spannungstensor in der Kruste zu simulieren. Dies wird mit Hilfe der Abaqus Submodeling Technik (siehe Abschnitt 1.3.1.) durchgeführt, die großräumige tektonische Randbedingungen (Plattenrandkräfte) mit lokalen Randbedingungen, wie z.B. Differenzen des Gravitationspotentials, und Abhängigkeiten von der lokalen Geometrie (Störungen, Schichten), verknüpft. Insgesamt werden mit der Submodeling Technik Modelle der SAF, der ECSZ und der Coso Range erstellt und analysiert.

Eine weitere Aufgabe dieser Arbeit ist die Bestimmung der Bruchflächendichte und der Bruchflächenorientierung auf der Skala des CGF, um Abhängigkeiten der Wasserwegsamkeiten von der Spannungsverteilung ableiten zu können. Da Bohrlochstabilität, Orientierungen natürlicher und induzierter Störungen und Klüfte, sowie Wasserwegsamkeiten direkt von der Spannungsverteilung abhängig sind, ist die Kenntnis des Spannungszustandes einer Lagerstätte wichtig, um Bohr- und Förderungsprozesse optimieren zu können.

### Konzept zum Aufbringen verschiedener Randbedingungen

Um den 3D Spannungstensor zu modellieren, müssen die verschiedenen Komponenten, die den kompletten Spannungszustand generieren, in Betracht gezogen werden. Dies sind Differenzen des Gravitationspotentials auf Grund von krustalen Mächtigkeitsänderungen oder lateralen Dichtekontrasten, Plattenrandkräfte und basale Scherkräfte (werden in dieser Arbeit vernachlässigt; Zoback, 1992). Ein weiteres Phänomen des Spannungszustandes in der Erdkruste ist, dass die horizontalen Spannungen nahe der Erdoberfläche größer als die vertikalen Spannungen werden (Figure 3.1).

Um diesem Phänomen Rechnung zu tragen wurde eine Prozedur entwickelt, bei der ein initialer Spannungszustand resultiert, der sich in einem gravitativen Gleichgewichtszustand befindet und eine Zunahme der horizontalen Spannungen nahe der Oberfläche erzeugt (Kapitel 3). Hierbei wird der Spannungszustand gegen ein analytisches Modell kalibriert (Sheorey, 1994; Figure 3.2). Der kalibrierte, initiale Spannungszustand kann nun verwendet werden, um die von der Tektonik abgeleiteten Randbedingungen aufzubringen. Die durch die Tektonik resultierenden Spannungen werden im weiteren mit unabhängigen Daten (Spannungsmagnituden und Spannungsorientierungen) kalibriert. Auf diese Weise wird sichergestellt, dass ein möglichst realistischer Spannungszustand generiert wird. Diese Vorgehensweise wird für alle Modelle befolgt und stellt einen wichtigen Teil der Arbeit dar (Kapitel 3).

### **Spannungszustand im Westen der USA und der San Andreas Störung**

Am Beispiel der Pazifisch – Nordamerikanischen Plattengrenze und der SAF werden die Interaktion der verschiedenen Komponenten des Spannungszustandes in der Erdkruste untersucht (Kapitel 4). Im speziellen wird analysiert, wie Variationen des Gravitationspotentials, Plattenrandkräfte und Störungsgeometrien die Spannungen in der Kruste beeinflussen. In Kapitel 4 wird gezeigt, dass die kalibrierten Modellergebnisse eine gute Übereinstimmung mit unabhängigen Spannungsdaten zeigen. Topographisch induzierte Änderungen des Gravitationspotentials des initialen Spannungszustandes resultieren zunächst in einem dominanten extensiven Spannungsregime, in dem Orientierungen von  $S_H$  variabel sind. Nach Aufbringen der tektonischen Randbedingungen werden folgende Regime erzeugt:

- Nahe der SAF (0-200km) in Zentralkalifornien dominieren *strike-slip* und Transpression.
- Am Big Bend Segment der Störung erfolgt ein Übergang von Transpression hin zu *strike-slip*. Im Mojave Block im südlichen Teil der ECSZ dominiert Transtension.
- Die ECSZ zeigt einen Übergang von *strike-slip* zu Transtension.
- Extension in der Basin and Range

Die Plattenrandkräfte resultieren in ausgeprägten, konsistenten Spannungsorientierungen und übertragen kompressive Spannungen in das Fernfeld. Der gekrümmte Verlauf der SAF ist die Hauptursache, dass diese erhöhten Horizontalspannungen erzeugt und bis in die ECSZ übertragen werden (Figure 4.6).

### **Stärke der San Andreas Störung**

Die Stärke der SAF in Abhängigkeit des Reibungskoeffizienten,  $\mu$ , und die damit verbundenen Scherspannungen auf der Störung sind Gegenstand kontroverser Diskussionen. Im Allgemeinen werden zwei unterschiedliche Szenarien angenommen. Das eine Szenario geht von einer relativ starken Störung ( $\mu=1.0$ ; z.B. Scholz, 2000) aus, das andere Szenario von einer relativ schwachen Störung ( $\mu<0.1$ ; z.B. Zoback et al., 1987). Eine Vorgehensweise, um die Stärke der SAF zu bestimmen, ist die Analyse des Winkels  $\beta$  von  $S_H$  zum Verlauf der Störung. Hierbei treten bei einer starken Störung kleine Winkel ( $\beta \sim 30^\circ$ ), und bei schwacher Störung große Winkel ( $\beta > 70^\circ$ ) auf.

Anhand des modellierten Spannungszustandes für das System der SAF wurde, unter der Annahme einer infinitesimal dünnen Störung, eine Sensitivitätsanalyse des Reibungskoeffizienten bezüglich den resultierenden Orientierungen von  $S_H$  zur Störung durchgeführt (Kapitel 5). Die Ergebnisse zeigen, dass die Orientierungen von  $S_H$  im Fernfeld nur in geringem Maße von  $\mu$  abhängen, denn im Fernfeld der Störung variieren die Orientierungen zwischen den beiden Extremfällen ( $\mu=0.1$  und  $\mu=1.0$ ) nur zwischen  $0^\circ$ - $5^\circ$ . Direkt auf der Störung sind die Differenzen etwas größer, bewegen sich aber immer noch im Rahmen von  $0^\circ$ - $10^\circ$ , und nicht wie in der Theorie vorausgesagt zwischen  $30^\circ$ - $50^\circ$ . Diese geringe Abhängigkeit, in Zusammenhang mit den unterschiedlichen Interpretationen, der Spannungsorientierungen könnte daraufhin deuten, dass die Analyse von Spannungsorientierungen zur Abschätzung der Stärke der SAF eine zweifelhafte Methode ist, und dass die Spannungsorientierungen eher Aufschluss über den Ladungszustand der Störung geben.

### **Spannungszustand in der ECSZ**

25% der relativen Plattenbewegung zwischen der pazifischen Platte und dem amerikanischen Kontinent wird von den aktiven Störungen der ECSZ übertragen. Der Spannungszustand repräsentiert dementsprechend einen Übergangsbereich zwischen dem extensiven Regime der Basin and Range Region und dem durch die dextralen Scherkräfte hervorgerufenen strike-slip Regime nahe der Plattengrenze. Das Spannungsfeld ist gekennzeichnet durch NNE gerichtete Kompression und WNW gerichtete Extension. Daten zu absoluten Spannungsmagnituden und die damit verbundene Ableitung der tektonischen Regime für die ECSZ sind kaum vorhanden. Zur Kalibrierung der Modellergebnisse wurden Daten des CGF und der World-Stress-Map (WSM) verwendet. Die Ergebnisse der FE Modelle zeigen eine gute Übereinstimmung mit diesen Daten (Kapitel 6). Die FE Ergebnisse liefern einen Spannungszustand, in dem die aktiven Störungen sich in einem strike-slip Regime bewegen und der Rest der ECSZ transtensiv ist. Mit der Simulation konnte gezeigt werden, dass der gekrümmte Verlauf der SAF die Ursache für erhöhte Horizontalspannungen in der ECSZ darstellt. Dieses Ergebnis stimmt mit weiteren Studien bezüglich der Ursache der ECSZ überein. Bei der Simulation mit GPS abgeleiteten Randbedingungen werden diese erhöhten Horizontalspannungen nicht erzeugt und repräsentieren somit für die ECSZ keinen adäquaten Ansatz zur Bestimmung von tektonischen Randbedingungen.

### **Spannungszustand in der Coso Range und des Coso Geothermal Field**

Der Spannungszustand in der Coso Range ist in zahlreichen Arbeiten bestimmt und dokumentiert worden. Diese Studien beobachten ein Übergangsregime von *strike-slip* zu Transtension.  $S_H$  weist eine konstante Orientierung von ~NNE auf. Die Modellergebnisse stimmen gut mit den  $S_H$  Orientierungen und Spannungsmagnituden für das CGF überein (Kapitel 7). Für die Coso Range wird ein Spannungsregime erhalten, das durch *strike-slip* Deformation nahe der Oberfläche und Transtension mit zunehmender Tiefe gekennzeichnet ist. Ein Vergleich mit von Spannungsverhältnissen (R) abgeleiteten tektonischen Regimen aus seismischen Daten zeigt eine gute Übereinkunft.

## Bruchnetzwerke und Wasserwegsamkeiten für das Coso Geothermal Field

Anhand des kalibrierten Spannungszustandes für das Coso Geothermal Field (CGF) wird mit Hilfe der Fracture Potential (FP) Methode (Connolly und Cosgrove, 1999) das Auftreten neuer Störungen oder die Reaktivierung bereits existierender Störungen simuliert und mit kartierten Störungen sowie der Verteilung der Seismizität verglichen (Kapitel 8). Die Übereinstimmung von FP Maxima mit seismischen Clustern zeigt (Figure 8.4), dass die Coso Range – Indian Wells Valley Region ein Gebiet ist, das von tektonischen Randkräften beeinflusst wird. Die schlechte Übereinstimmung der Modellergebnisse von FP und beobachteter Seismizität im Gebiet des CGF lässt sich dadurch erklären, dass Wasserzirkulationsprozesse durch die Exploration maßgeblich zur Verteilung der Seismizität beitragen. Um dies zu simulieren, reicht ein elastischer Modellansatz, wie hier verwendet, nicht aus. Stattdessen müsste man effektive Spannungen mittels poro-elastoplastischem Materialverhalten simulieren.

Potentielle, optimal orientierte, virtuelle Scherbrüche (synthetisch und antithetisch), die mit den FP Ergebnissen vorhergesagt werden, stimmen im Allgemeinen gut mit dem kartierten Verlauf des Störungsnetzwerkes in der Coso Range überein. Die meisten virtuellen Scherbrüche weichen maximal bis zu  $20^\circ$  von den Orientierungen kartierter Störungen ab. Dies ist ein Indikator dafür, dass das Auftreten von Bruchprozessen in der Coso Range wahrscheinlich Reaktivierungsprozesse entlang existierender Störungen darstellt.

Mit Hilfe von mean stress abgeleiteten Druckänderungen werden mögliche Wasserwege für das CGF analysiert. Hierbei fließt das Wasser von einer Region hohen mean stresses im Norden der Coso Range südwärts auf ein Gebiet erniedrigten mean stresses im Indian Wells Valley zu. Ein lokal erniedrigter mean stress am südlichen Ende der Coso Wash Störung (CWF) sorgt dafür, dass sich die Flussvektoren innerhalb des CGF von Nord-Süd auf Nordwest-Südost drehen und auf die CWF zufließen. Von besonderer Bedeutung ist nun das Zusammenspiel von vorhergesagten Scherbrüchen, kartierten Störungen und den Flussvektoren, um ein Gesamtbild der Wasserwegsamkeiten entlang von Störungen und Klüften zu erhalten. Das Modell zeigt, dass nördlich des CGF NNE orientierte Scherbrüche den Nord-Süd Fluss unterstützen könnten und die NW-SE orientierten Scherbrüche innerhalb des CGF das Wasser in Richtung CWF leiten. Andererseits könnten NNE orientierte Scherbrüche innerhalb des CGF den Fluss Richtung CWF verhindern oder umleiten. Zusammenfassend lässt sich schlussfolgern, dass das CGF ein Durchflussgebiet ist, in dem erniedrigte mean stresses an der CWF auf eine potentielle Fluidakkumulation schließen lassen. Dieses Gebiet stimmt zudem mit der kürzlichen East Flank Erweiterung des CGF überein.

## Zusammenfassung/Schlussfolgerungen

In dieser Arbeit wird der 3D Spannungszustand der Erdkruste mit Hilfe der FE Methode simuliert. Der modellierte Spannungszustand basiert auf einer sich im Gleichgewicht befindenden Kruste in der Spannungen durch Differenzen des Gravitationspotentials und durch Randbedingungen, die tektonische Plattenrandkräfte

simulieren, erzeugt werden. Der resultierende Spannungszustand und davon abgeleitete Parameter sind direkt vom Verhältnis horizontaler zu vertikalen Spannungen abhängig. Dies zeigt die Notwendigkeit einen initialen Spannungszustand zu simulieren, der sich in einem gravitativen Gleichgewichtszustand befindet und gegenüber analytischen Modellen wie dem von Sheorey kalibriert ist. Numerische Modelle, die dies nicht berücksichtigen und die nicht gegenüber unabhängigen Daten kalibriert sind, müssen vorsichtig verwendet werden, wenn spannungsabhängige Parameter analysiert werden. Mit Hilfe der Submodeling Technik wird eine Verbindung großräumiger tektonischer Randkräfte mit lokalen spannungsabhängigen Prozessen ermöglicht. Der Modellierungsansatz dieser Arbeit liefert realistische 3D in-situ Spannungen für alle betrachteten Modellgrößen. Damit liefert der Ansatz eine geeignete Basis um tektonische Regime, relevante Störungsparameter und, speziell für die Coso Range und das CGF, neue Bruchflächen, Bruchflächenorientierung und Wasserwegsamkeiten direkt von der Spannungsverteilung ableiten zu können.

Ein großer Vorteil des gewählten Modellansatzes ist, dass die Modelle nicht nur ausschließlich einem einzigen Zweck dienen. Die FE Modelle können für verschiedene Analysen des Spannungszustandes, wie z.B. Fracture Potential, Slip Tendency, Scher- und Normalspannungsverteilungen auf speziellen Störungen, oder Coulomb Failure Stress, verwendet werden. Weiterhin besteht bei allen Modellen die Möglichkeit Verbesserungen zu integrieren und weitere, tiefergehende Analysemethoden durchzuführen. Zukünftige Arbeiten sollten, speziell für das CGF, die Implementierung poro-elasto-plastischen Materialverhaltens berücksichtigen, um effektive Spannungen, und somit eine realistischere Kopplung zwischen Fracture Potential und Seismizität zu erreichen. Weiterhin könnten transiente oder statische Flussrandbedingungen zusätzliche Auskunft über die Wasserwegsamkeiten im CGF liefern.

Zusammenfassend lässt sich sagen, dass mit Hilfe linear elastischer FE Modelle ein realistischer 3D Spannungszustand der Erdkruste für verschiedene Modellgrößen simuliert wurde und somit die nachfolgenden Analyse spannungsabhängiger Parameter ermöglicht wurde. In Verbindung mit anderen Untersuchungsmethoden (Seismik, Geomagnetik, Geodäsie, etc.) ist nun ein besseres Verständnis von regionaler und lokaler Tektonik und damit verbundener Prozesse möglich.



## 1. Introduction

### 1.1. Purpose of the work

In earth sciences the knowledge of the three dimensional (3D) state of stress is essential both for understanding geodynamic processes as well as for optimizing reservoir processes in geothermal and hydrocarbon systems. For both large and small scale tectonic processes, the 3D state of stress defines tectonic regimes, determines the seismically most active and hazardous regions and gives indications on crucial fault parameters. In a reservoir information on the 3D state of stress is essential to optimize drilling, production and well bore stability. Crucial parameters such as the likelihood of fracture generation, fracture orientation, fluid pathways, optimal drilling direction and reservoir pressure are directly dependent on the 3D state of stress. In both research areas geomechanical models to simulate the 3D state of stress often contain complex three-dimensional geological structures. Therefore, numerical methods such as the finite element (FE) method provide a useful tool to simulate and analyze geodynamic processes and study their impacts on the resulting state of stress.

The tectonics of the Western United States (WUS) and especially the San Andreas Fault (SAF) system and its interaction with the Eastern California Shear Zone (ECSZ) represent one of the most interesting examples for studying the interaction of the different contributions to the 3D crustal state of stress. Productivity of the Coso Geothermal Field located in the ECSZ is directly related to tectonic deformation processes and thus knowledge of the in-situ state of stress becomes of interest. The purpose of this thesis is twofold:

- Develop a series of multi-scale FE models to simulate the full crustal stress tensor in the WUS. The models are applied to scales of the SAF, the ECSZ and the Coso Range.
- Use results of the modeled 3D state of stress on the scale of the Coso Geothermal Field to analyze second order fracture networks and associated fluid flow pathways from tectonically induced mean and differential stress variations.

### 1.2. Questions to be addressed

Within this framework the following set of relevant questions will be addressed:

1. What are the different contributions to the 3D crustal state of stress in the WUS?
2. What is its influence of the SAF on ECSZ tectonics? Is it a strong or a weak fault?
3. What are the causes for the transtensional state of stress in the ECSZ/Coso Range?
4. Coso Geothermal Field (CGF): how do tectonically induced stresses affect the likelihood of 2<sup>nd</sup> order fracture generation and associated fluid flow pathways?

### 1.3. Approach used

#### 1.3.1. Multi-scale modeling – Submodeling approach

Since the scope of this study is focused on different aspects and scales of the WUS state of stress, several models have to be generated. In this process it is important to

emphasize that the application of boundary conditions simulating tectonic loads can be most realistically determined at the scale of the SAF. Plate boundaries can be defined as model boundaries and their displacements or acting forces can be determined most accurately and realistically. In general, these boundaries influence large regions (i.e. tectonic plates) and therefore sufficient resolution on a local scale (10's km) can not be obtained due to computational limitations. For the area of interest a higher resolution, i.e. finer discretization of the FE mesh, is necessary to resolve stress perturbations due to local inhomogeneities such as fault distribution or lithology changes. In order to yield higher resolution data in the ECSZ and Coso Range region, the technique of submodeling is used (ABAQUS/Standard User's Manual, §7.3.1). The purpose of submodeling in an FE analysis is to obtain an accurate, detailed solution in a local region of a larger and coarser model. Boundary conditions applied to the local part of the model (with finer mesh) use values interpolated from the solution of the initial, coarser "global model". When using the submodeling procedure, an initial coarse global model, with all corresponding boundary conditions is run. Since the submodel is a separate analysis, submodeling can be used to any number of levels, i.e. a submodel can be used as a global model for a subsequent submodel. The results from the global model are interpolated on the appropriate parts of the boundary of the submodel. Thus the response at the boundary of the local region is defined by the solution for the global model. The driven nodes and any loads applied to the local region determine the solution in the submodel. It is important to emphasize that the solution for the state of stress of the global model in this analysis is fully calibrated against stress magnitudes, orientations and derived tectonic regimes. Once the displacements of the global model analysis are generating a "realistic" state of stress in the global model they are transferred to the submodel scale. In this study the submodeling technique is applied twice. The initial global model is at the SAF scale. These results are transferred to a model of the ECSZ. Then these results are applied to a model of the Coso Range.

An alternative to the submodeling technique would require the determination of the relevant boundary conditions at each scale, separately. Since it is most convenient to apply displacement loads as boundary conditions in geomechanical modeling (tectonic boundary forces applied to the model boundaries are difficult to determine and lateral and vertical inhomogeneities of these forces are mostly unknown), the GPS derived surface displacements and tectonic block motions (e.g. NUVEL plate motion models, DeMets et al., 1990) are commonly used to drive the model. However, GPS data are constrained to specific regions or campaign profiles and do not evenly cover large regions. Hence, these data need to be interpolated. Continuous spatial grids of GPS velocities have to be computed using constraints of bigger scale processes. Using such an approach would be very similar to the submodeling approach which is already implemented in the ABAQUS software routines. Furthermore, as demonstrated for the scale of the ECSZ, interpolation of the ECSZ GPS displacements to the model boundaries does not yield the observed tectonic regimes since the compression imposed by the SAF is not reflected by the GPS displacements (see chapter 6).

### 1.3.2. Loading procedure and model calibration

Modeling the 3D crustal state of stress is a task that requires care. The different contributions generating the complete state of stress have to be accounted for. These are gravitational potential energy differences due to crustal thickness variations and density variations, plate boundary forces and basal tractions. Zoback (1992) showed that there is little evidence for strong basal tractions affecting the stress field in the lithosphere. Liu et al. (2007) conclude that basal shear tractions for the WUS lithosphere are <2MPa. Since only the 3D crustal state of stress is analyzed in this study and basal traction boundary conditions are difficult to determine and moreover difficult to apply in 3D, basal tractions are neglected in this study. Furthermore, the horizontal stress paradox, i.e. horizontal stresses near surface become larger than the vertical ones, requires an initial state of stress that produces realistic horizontal stresses. This state of stress is generated by calibrating the modeling results to the analytical model of Sheorey (see chapter 3). Once this is achieved additional tectonic loads are applied to the model.

The resulting state of stress needs to be calibrated against independent data. Since only linear elastic rheologies are used, the magnitudes of the displacement boundary conditions mimicking the tectonic loading are constrained by the state of stress predicted. The model results are compared to stress dependent tectonic regimes and stress measurements at certain locations. Furthermore, resulting orientations for the maximum horizontal stress component are compared to orientations of the World-Stress-Map. Difference grids give information on the quality of the results. Once the models are calibrated the resulting state of stress is used to analyze subsequent parameters.

### 1.3.3. Fault modeling

Faults play a major role in this study and hence the way in which they are incorporated into the FE models must be described. Generally, there are two ways of modeling faults in ABAQUS. Either as a rheology contrast, in which the fault is included as a region with weaker material. This can be accomplished by modeling the fault as a narrow zone of elements which obey plastic rheological laws accounting for deformation. Once a certain failure criterion is reached within the fault elements, this can be Mohr-Coulomb failure or a variety of Drucker-Prager failure criterions (Davis and Selvadurai, 2002), the element fails and plastic strain energy is released. The other possibility is the usage of contact surfaces (CS) which is followed in this study. A contact surface is the numerical description of a surface based frictional sliding between two bodies. The CS is a pre-existing discontinuity surface in the FE mesh. The main role of a contact surface between 2 bodies is the ability to carry displacements or slips once a certain failure criteria has been reached. In this study the contact surfaces obey Coulomb friction ( $\tau = \mu * \sigma_n$ ) defined by the coefficient of friction,  $\mu$ , on the fault surface.

Within the FE model it is necessary to predefine the contact surfaces. The first step of which is to duplicate the nodes on the two surfaces of the fault. These duplicate nodes are linked to their corresponding contact elements and are assigned to each side of the fault as either a master or a slave surface (Figure 1.1). These two surfaces are then made to interact via the ABAQUS \*CONTACT PAIR card. Hereby, in-plane displacements are

allowed on the fault surface. The contact nodes are not allowed to separate normal to the fault plane.

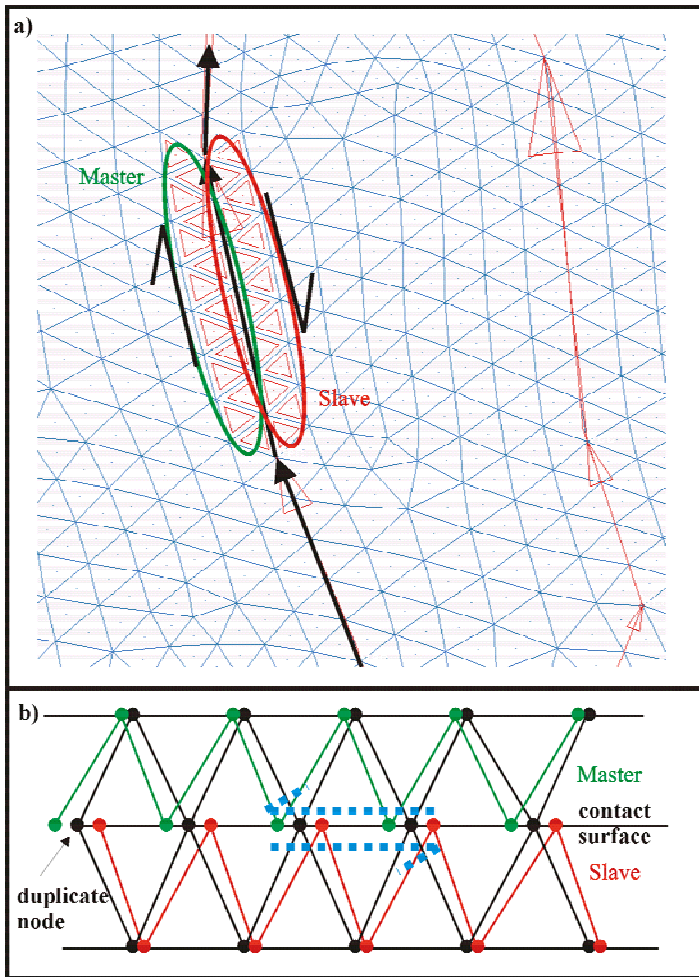


**Figure 1.1:** a) Fault slips at fault segments along vectors with corresponding contact elements of master and slave surfaces (2D). b) deformed mesh after slip occurs, showing the principle of duplicate nodes.

### 1.3.4. Modeling processes - Software used

The numerical models presented in this study are solved using the standard routine of the commercial finite element software package ABAQUS<sup>TM</sup>, version 6.6-1 (<http://www.simulia.com>). The model geometry is initially composed by using GoCAD (<http://www.earthdecision.com>). Discretization of the model volume is undertaken with the commercial software package HyperWorks, version 7 (<http://www.altair.com>). The FE results were analyzed and visualized with the post-processing tool GeoMoVie by Peter Connolly. For visualization and mapping of the FE results the commercial software Surfer, version 8 (<http://www.goldensoftware.com>) was used.

### 1.3.5. Computation

The overall effort to establish a FE model beginning with the data compilation of the geometry, the geometry composition (GoCAD), the model discretization

(HyperWorks), Sheorey calibration, and tectonic loading analysis/calibration comprises a time span of approximately 3 months. Individual efforts are listed in Table 1.1.

The FE models are solved on a SGI Altix 350 solver using 12 1.5GHz Itanium processors. Computation times for the various models are listed in Table 1.2.

<b>Work processes</b>	<b>Time period</b>
Geometrical data compilation	1 week
Model composition in GoCAD	~2 weeks
Model discretization	~6 weeks
Sheorey calibration	1 week
Tectonic loading analysis/calibration	~3 weeks
<b><i>Overall time to establish model</i></b>	<b><i>~12 weeks</i></b>

**Table 1.1:** Time estimates for the various work processes in order to establish a fully calibrated geomechanical FE model.

<b>Model</b>	<b>Solving time</b>
SAF Sheorey calibration	~1.5 hours
SAF tectonic loading	~ 2 hours
ECSZ Sheorey calibration	~2 hours
ECSZ tectonic loading	~2.5 hours
Coso Sheorey calibration	~3 hours
Coso tectonic loading	~4.5 hours

**Table 1.2:** Solving times for the individual modeling steps.



## 2. Theory

In the following chapter a brief summary of stress theory and related physical properties is given. The short compilation of stress theory represents a summary from corresponding text books by Ramsay (1967), Timoshenko and Goodier (1970), Ranalli (1995), Davis and Selvadurai (1995), Eisbacher (1996), Ramsay and Lisle (2000), Turcotte & Schubert (2002), Jaeger and Cook (2007).

### 2.1. The stress tensor

Deformation in a continuous medium occurs due to the acting of two kinds of forces, body forces and surface forces. Body forces act throughout the volume of the body and thus their magnitude is directly proportional to the volume or mass involved. The body force per unit mass in geophysics is the acceleration of gravity. Surface forces act on arbitrary surface elements bounding a body. The resistance against surface forces is defined as stress and is expressed by the traction vector  $\vec{T}$ , which is defined by the limit

$$\vec{T} = \lim_{\Delta A \rightarrow 0} \frac{\Delta \vec{F}}{\Delta A}. \quad (2-1)$$

The traction vector can vary by the size of the force, as well as the size of the area and the orientation of the surface. In general, the traction vector can comprise any angle with the surface and thus can be divided into two vector components: one component acts normal to the surface (normal stress) and the other parallel (shear stress). Cauchy showed that the traction vector on any arbitrary surface can be determined by

$$\vec{T} = \sigma_{ij} \hat{n}_j. \quad (2-2)$$

$\hat{n}_j$  represents the unit normal vector of any arbitrary surface and  $\sigma_{ij}$  describes the three-dimensional stress tensor at any point:

$$\sigma_{ij} = \begin{pmatrix} \sigma_{xx} & \sigma_{xy} & \sigma_{xz} \\ \sigma_{yx} & \sigma_{yy} & \sigma_{yz} \\ \sigma_{zx} & \sigma_{zy} & \sigma_{zz} \end{pmatrix}. \quad (2-3)$$

Cauchy also showed that  $\sigma_{ij}$  is symmetric, which follows from the conservation of the angular momentum. Thus only six independent stress components are necessary to completely define the state of stress at any point. In geosciences it is often convenient to consider the components of the traction vector that act normal and parallel to the surface, e.g. a fault surface of interest. The component acting perpendicular to the surface is defined by the scalar product  $(\vec{T} \cdot \hat{n})\hat{n}$  and the component acting parallel is given by the triple vector product  $\hat{n} \times (\vec{T} \times \hat{n})$ . The magnitude of the normal component is called the normal stress acting on the surface and the magnitude of the tangential component is called the shear stress on the surface. It should be noted that both normal and shear stress are

scalars and are meaningless unless the surface they act upon is completely specified.  $\sigma_n$  and  $\tau$  can be expressed as

$$\begin{aligned}\sigma_n &= \vec{T} \cdot \hat{n} \text{ and} \\ \tau &= \sqrt{\vec{T} \cdot \vec{T} - \sigma_n^2}.\end{aligned}\quad (2-4)$$

## 2.2. Principal stresses

By applying a principal axes transformation of the stress tensor a coordinate system can be found, where any shear stresses vanish and only the normal stresses  $\sigma_1$ ,  $\sigma_2$  and  $\sigma_3$  occur, which are referred to as the principal stresses.

$$\sigma^P = \begin{pmatrix} \sigma_1 & 0 & 0 \\ 0 & \sigma_2 & 0 \\ 0 & 0 & \sigma_3 \end{pmatrix} \quad (2-5)$$

The three principal stresses are identified as maximum principal stress  $\sigma_1$ , intermediate principal stress  $\sigma_2$  and minimum principal stress  $\sigma_3$ .

## 2.3. Mean stress

The mean stress is defined as the arithmetic mean of the three principal stresses:

$$\sigma_m = P = \frac{\sigma_1 + \sigma_2 + \sigma_3}{3} = \frac{1}{3} \text{trace}(\sigma_{ij}) = \frac{1}{3} \sigma_{kk} \delta_{ij}. \quad (2-6)$$

The mean stress is also termed as pressure  $P$ , but only corresponds to the hydrostatic pressure under the condition  $\sigma_1 = \sigma_2 = \sigma_3$ . The mean stress causes volume changes in rocks. It should be noted that these conditions only apply for linear theory.

## 2.4. Differential stress

The differential stress is the difference between the maximum principal stress and the minimum principal stress:

$$\sigma_d = \sigma_1 - \sigma_3. \quad (2-7)$$

The differential stress is the main responsible factor in producing shear stresses, which cause fracturing in materials.

## 2.5. Mohr circle of stress

The resolution of stress into shear and normal components is used to analyze many problems of geodynamic significance, e.g. fracture processes and faulting. Since shear stress is related to fracture processes it is important to determine the planes on which the shear stress is maximum. If the principal stresses are known it is possible to derive normal and shear stresses acting on any plane with given orientation. This state of stress can be represented with the so called Mohr circle in a new coordinate system with axes  $\sigma_n$  and  $\tau$  (Fig. 2.1). The Mohr circle also demonstrates that the planes of maximum shear stress are

equally oriented  $\beta = \pm 45^\circ$  to the principal stress axis. Note that the maximum shear stress is not related to the maximum values of the principal stresses but to the differential stress:

$$\tau_{\max} = \frac{\sigma_1 - \sigma_3}{2} \quad (2-8)$$

If the applied stresses cannot be accommodated by elastic deformation, permanent deformation will occur; termed brittle failure. Generally, there are two types of brittle failure: tensile fractures and shear fractures. The conditions for each failure mode are extensively described in standard text books (e.g. Jaeger and Cook, 2007).

Tensile fractures occur in the plane normal to the minimum principal stress. If a certain value of  $\sigma_3$  (the tensile strength T) in a cross section of the rock is exceeded, the rock fails in tension.

Coulomb postulated that shear failure on a surface will occur if the shear stress acting on that plane exceeds the cohesive strength of the rock plus the frictional resistance to movement, resulting in the Coulomb failure criterion:

$$\tau = c_0 + \mu_i \sigma_n \quad (2-9)$$

Where  $\tau$  is the shear stress acting along the surface,  $c_0$  is the cohesive strength,  $\mu_i$  represents the coefficient of internal friction and  $\sigma_n$  is the normal stress (Fig. 2.1).

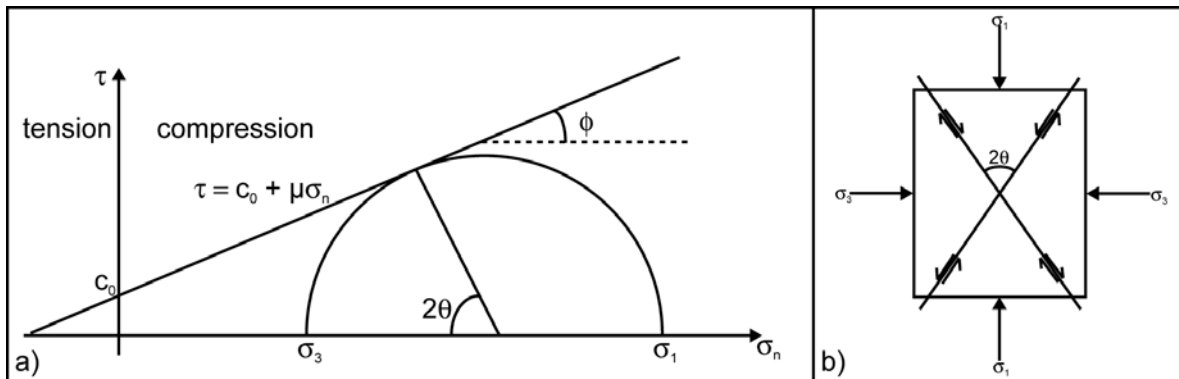


**Figure 2.1: a)** Coulomb failure criterion displayed using a Mohr circle construction. If the Mohr circle touches the failure envelope, failure will occur. **b)** shear failure of a rock sample is possible on two conjugate planes forming an angle of  $\pm\theta=45^\circ-\phi/2$ .

By analogy to sliding friction,

$$\mu_i = \tan \phi_i, \quad (2-10)$$

where  $\phi_i$  is the angle of internal friction. Considering the geometry of Figure 2.1a, it is clear that the relation between the angle of friction and the failure angle is given by

$$\theta = 45 - \frac{\phi_i}{2}. \quad (2-11)$$

The shear stress is not dependent on the sign of the fracture angle  $\theta$ , and thus two conjugate failure planes are possible at angles of  $\pm\theta$  to  $\sigma_1$  (Fig. 2.1b) resulting in so called synthetic and antithetic shear fractures.

Using the combined “Griffith-Coulomb” failure criterion enables distinction between tensile and shear fractures. As shown by Griffith (see Jaeger and Cook, pp.314, Connolly and Cosgrove, 1999) the most important factor for separating shear and tensile failure is differential stress (Fig. 2.2). If  $\sigma_d > 4T$  the Mohr circle (see red and blue Mohr circles in Figure 2.2) cannot touch the tensile part of the failure envelope, and thus can only fail by reaching the envelope in the shear regime. If  $\sigma_d < 4T$  failure is only possible if  $\sigma_3 = -T$  and thus the distance between  $\sigma_3$  and  $-T$  becomes important. This is analogous to the relationship of Price (1966):

$$c_0 = 2T . \quad (2-12)$$

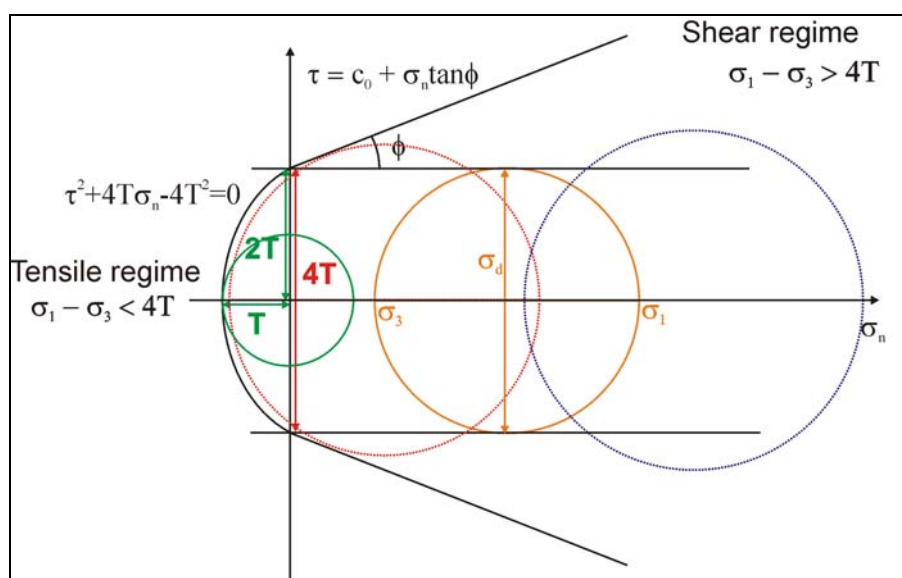


**Figure 2.2: Combined Griffith -Coulomb failure criterion. Shear failure is possible if  $\sigma_d > 4T$  (red and blue circle), tensile failure is possible if  $\sigma_d < 4T$  (green circle).**

## 2.6. Fracture Potential (FP)

Second order fracture type and likelihood are key factors in this study and it is desirable to use a tool that enables prediction of expected fracture type due to prevailing stress states. Since only linear elastic rheologies are used in the FE modeling study which do not include plastic failure of rock, a method has to be used which enables to study the occurrence of brittle failure in the present state of stress. To this end, the fracture potential method (FP) is used herein (Connolly and Cosgrove, 1999, Eckert and Connolly, 2004). The advantage of FP over other concepts such as Coulomb-Failure-Stress (CFS) and slip tendency is that it is reliant on knowing only four scalar parameters: differential stress, the mean stress, the cohesion and the coefficient of friction. The FP predicts regions where fracturing is likely and the type of fracture that will develop. Concepts such as the CFS require a specific knowledge of the actual stress state and the orientation of the faults and are not directly applicable to intact failure.

### 2.6.1. Fracture potential in the shear regime (sFP)

The definition of the fracture potential in the shear regime (sFP) is based on the relationship between the critical differential stress at failure and the actual differential stress (Figure 2.3) as shown on a 2D Mohr circle construction.

$$FP = \frac{\sigma_d/2}{\sigma_{d,crit}/2} \quad (2-13)$$

If this ratio reaches a value of 1, the Mohr circle of the actual stress state reaches the failure envelope and failure occurs.

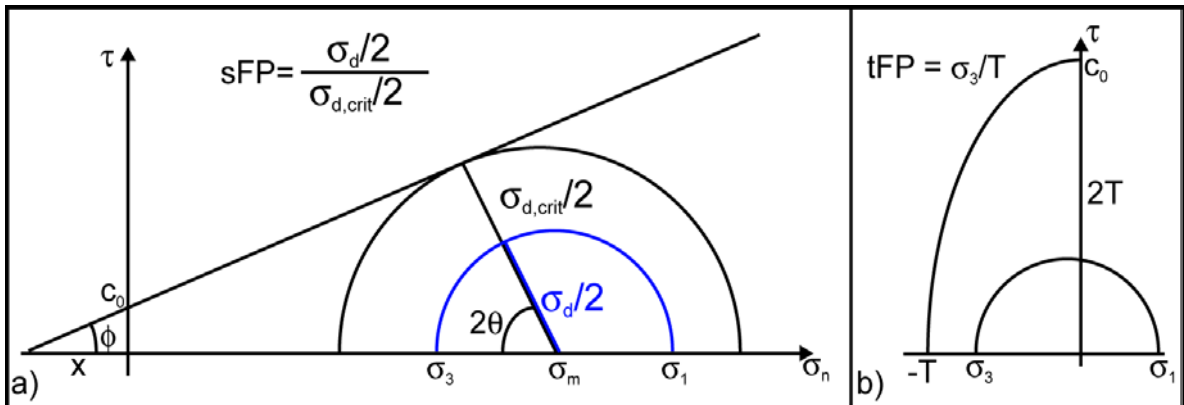


**Fig. 2.3:a)** Derivation of the sFP in the shear regime. Failure occurs if the Mohr circle reaches the envelope and thus a critical differential stress  $\sigma_{d,crit}$  is exceeded. Giving actual stress states a likeliness of fracturing the differential stress is set in relation to  $\sigma_{d,crit}$ . **b)** The fracture potential in the tensile regime is defined as the ratio of  $\sigma_3$  to T. Due to the shape of the Griffith parabola failure can take place if  $\sigma_3$  overcomes the tensile strength.

The derivation of the critical differential stress utilizes  $\sin \phi = \frac{\sigma_{d,crit}/2}{x + \sigma_m}$  and  $x = \frac{c_0}{\tan \phi}$ .

Therefore:

$$\frac{\sigma_{d,crit}}{2} = \left( \frac{c_0}{\tan \phi} + \sigma_m \right) \sin \phi = c_0 \cos \phi + \sigma_m \sin \phi. \quad (2-14)$$

Giving the shear fracture potential as:

$$SFP = \frac{\sigma_d/2}{\sigma_{d,crit}/2} = \frac{\sigma_d}{2(c_0 \cos \phi + \sigma_m \sin \phi)}. \quad (2-15)$$

sFP is only determined when shear failure is possible ( $\sigma_d > 4T$ ). At low differential stress only tensile failure is possible and sFP is undetermined. Thus, if  $\sigma_d < 4T$  the sFP is 0, since shear failure cannot occur.

### 2.6.2. Fracture potential in the tensile regime (tFP)

In the tensile regime, the fracture potential is the ratio of  $\sigma_3$  to the tensile strength of the material. Since the material can only fail if  $\sigma_3$  is larger than the tensile strength, the tFP is defined as (Figure 2.3):

$$tFP = \frac{\sigma_3}{T} \quad (2-16)$$

It should be noted that the overall criteria for failure in tension is  $\sigma_d < 4T$ . If  $\sigma_3$  is positive, a compressional state of stress must exist and therefore the fracture potential in tension is set to 0.

In summary, FP lies between -1 (tensile failure) and +1 (shear failure), with the closer to each extreme, the more likely the respective mode of fracturing. A FP value of 0 indicates a stress state which brittle failure theory indicates will not fail by fracturing.

### 2.7. Regime-Stress-Ratio (RSR)

Anderson (1905) defined three basic types of faulting (extensional, strike-slip and compressional) based on the relative magnitudes of the principal stress components  $\sigma_1$ ,  $\sigma_2$  and  $\sigma_3$ , one of which he assumed to be normal to the Earth's surface. Thus, depending on which principal stress is vertical, new faults will be either extensional, strike-slip or compressional. Unfortunately, this classification does not distinguish between cases away from end-member faulting regimes, e.g. a mixture of extensional and strike slip faulting (transtension).

Bott (1959) showed that the slip direction is not only dependent on the orientation of the maximum principal stress but also on the stress ratio R.

$$R = \frac{\sigma_2 - \sigma_3}{\sigma_1 - \sigma_3} \quad (2-17)$$

where  $\sigma_1 > \sigma_2 > \sigma_3$ . R conveys information about the relative magnitudes of the three principal stresses but not their orientation. If the geometric information (implicit in Anderson's work) is included a new parameter RSR ( $A_\Phi$ , Simpson, 1997) can be derived by combining regime and R. Assigning the Andersonian regimes of extensional, strike-slip and compressional faulting values of 0, 1 & 2 respectively, RSR is defined by:

$$RSR = (n + 0.5) + (-1)^n (R - 0.5) \quad (2-18)$$

RSR is thus a continuous function between 0 - 3 that covers all faulting regimes from radial extension (0), extension (0.5), transtension (1), strike-slip (1.5), transpression (2), compression (2.5) to constriction (3). Using RSR enables easy identification of the particular type of faulting if the tensor is available. This is particularly important in regions where transpression and transtension occur.

## 2.8. Finite Element modeling

### 2.8.1. Equations of equilibrium

In general, problems in continuum mechanics require the solution of a linear, non-linear or  $x^{\text{th}}$  order partial differential equation (PDE) with appropriate boundary conditions. The equations of motion for small movements following the conservation of momentum is:

$$\frac{\partial \sigma_{ij}}{\partial x_j} + \rho B_i = \rho a_i \quad (2-19)$$

Where  $a$ =accelerations and  $\rho$ =density of the material.  $\rho$  represents an average, homogeneous, consistent density and thus the conservation of mass is followed.

In tectonic problems accelerations are normally assumed to be negligible since the instantaneous displacements are low. Hence the body is in a state of equilibrium and the equations of static elasticity are applicable (Ranalli, 1995). For a continuous body to be in equilibrium, the resultant of all body and surface forces has to vanish as well as the resultant moment about any axis. The equations of the equilibrium of forces acting in  $x$ -direction are

$$\begin{aligned} & \left( \sigma_{xx} + \frac{\partial \sigma_{xx}}{\partial x} dx \right) dy dz - \sigma_{xx} dy dz + \left( \sigma_{yx} + \frac{\partial \sigma_{yx}}{\partial y} dy \right) dx dz - \sigma_{yx} dx dz \\ & + \left( \sigma_{zx} + \frac{\partial \sigma_{zx}}{\partial z} dz \right) dx dy - \sigma_{zx} dx dy + \rho B_x dx dy dz = 0 \end{aligned} \quad (2-20)$$

The partial derivatives represent the rate of change of the stress components in the relevant coordinate direction.  $B_x$  denotes the component of body force per unit mass with density  $\rho$ . Transforming equation (3-11) it follows that

$$\frac{\partial \sigma_{xx}}{\partial x} + \frac{\partial \sigma_{yx}}{\partial y} + \frac{\partial \sigma_{zx}}{\partial z} + \rho B_x = 0. \quad (2-21)$$

Using the similarity for  $y$ - and  $z$ -directions equation (3-12) can be written in index notation

$$\frac{\partial \sigma_{ji}}{\partial x_j} + \rho B_i = 0. \quad (2-22)$$

Perfect linear elasticity can be expressed as

$$\sigma_{ij} = C_{ijkl} \varepsilon_{kl}, \quad (2-23)$$

and is called Hooke's law.  $\varepsilon_{ij} = \frac{1}{2} \left( \frac{\partial u_i}{\partial x_j} + \frac{\partial u_j}{\partial x_i} \right)$  is the infinitesimal strain tensor with displacement components  $u$  (e.g. Ranalli, 1995, pp.38-39).  $C_{ijkl}$  represents a set of 81

elastic parameters, which reduces to 36 since both the stress tensor and the strain tensor are symmetric. Substituting (2-23) into (2-22) we get:

$$\frac{\partial}{\partial x_j} [C_{ijkl} \cdot \varepsilon_{ij}] + \rho B_i = \frac{\partial}{\partial x_j} \left[ C_{ijkl} \frac{1}{2} \left( \frac{\partial u_i}{\partial x_j} + \frac{\partial u_j}{\partial x_i} \right) \right] + \rho B_i = 0 \quad (2-24)$$

A unique solution of Equation (2-24) requires so called boundary or initial conditions.

If a PDE cannot be solved analytically, numerical solutions such as the finite element method may be applicable. The transition from an analytical to a numerical solution represents transition from a continuous to a discrete description of the problem. In this process, the continuum is divided into a number of simply shaped sub-regions, the so-called finite elements, of which each demands internal continuity. The elements are interconnected at a discrete number of points, termed nodes, which are located on the element's boundaries. The displacements of these nodes are the unknown parameters in the problem.

Once the model region has been discretized, a set of linear equations of the unknown field variable, in this case the displacements  $[u(x)]$ , is approximated for each element. Using a linear approximation requires a dense discretization in regions where the gradient of  $u(x)$  is high. The finer the discretization, the better the fit of the linear approximation functions to the trend of  $u(x)$  (Figure 2.4). Thus, in regions of high displacement gradients a fine discretization is needed in order to minimize the numerical error. With this inherent need of fine discretization, the submodeling approach (see chapter 1.3.1) is used to achieve high resolution on the study region. After each element has been approximated into a set of linear equations, these approximation functions are assembled into a global equation, which enables solution of the numerical problem. Which is now:

$$\vec{F} = \bar{K} \cdot \vec{u} \quad (2-25)$$

Where:  $\bar{K}$  :global stiffness matrix representing the material properties and geometry of the elements,  $\vec{u}$  : field variable, in this case displacements, and  $\vec{F}$  : load vector. Hence an equation is found that relates the displacements to the forces acting in the model. Once this equation is solved the stresses and strains can be derived from it.

The major advantage of the finite element method over other numerical procedures such as the finite difference or the boundary element methods is that the FE approximation functions do not have to be differentiable. This implies that every element can be assigned different material properties and the model can handle more complex geometries. Since the shape and size of the finite elements can be chosen arbitrarily, complex model boundaries can be described easily. The complete mathematical description of the finite element method is complex and is beyond the scope of this study. Only the fundamental concept has been outlined. Further details are given in Zienkiewicz & Taylor (1994, Vol. 1 &2), which is considered as the standard textbook dealing with FE.

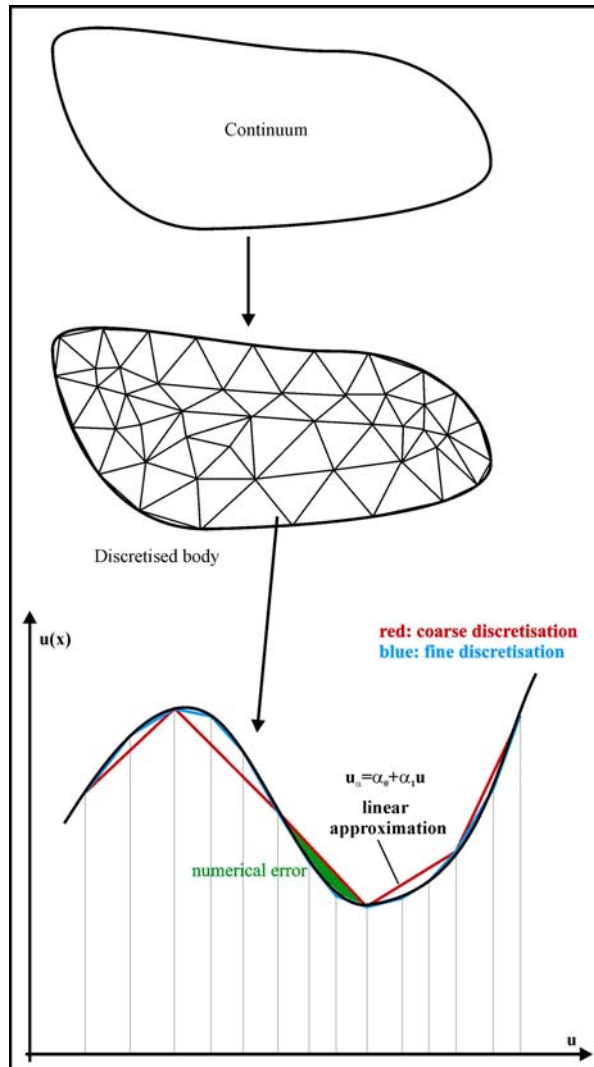


**Figure 2.4:** Sketch demonstrating the FE method. The observed field variable  $u(x)$  in a continuum is described by a PDE which cannot be solved analytically. Therefore, the continuum is discretized into finite elements, in which the behavior of  $u(x)$  is described by a set of linear equations  $u_\alpha = \alpha_0 + \alpha_1 u$ , in which  $\alpha$  indicate the approximation coefficients. In regions where the gradient of the field variable is steep, a fine discretization is needed to minimize the numerical error.



### 3. Finite Element modeling of tectonic stresses

The content of this chapter represents the results of work efforts undertaken in the Tectonic Stress Group of the Geophysical Institute of the University of Karlsruhe. Involved co-workers were Tobias Hergert, Thies Buchmann, Peter Connolly, Gwendolyn Peters, Oliver Heidbach and Birgit Müller.

#### 3.1. Introduction

The knowledge of the 3D state of stress is essential both for understanding geodynamic processes and for optimizing reservoir processes in geothermal and hydrocarbon systems. For both large and small scale tectonic processes, the 3D state of stress defines tectonic regimes, determines the seismically most active and hazardous regions and gives indications on crucial fault parameters such as shear stress and slip tendency. In a reservoir, both hydrocarbon and geothermal, information on the 3D state of stress is essential to optimize drilling, production and well stability. Crucial parameters such as the likelihood of fracture generation, fracture orientation, fluid pathways, optimal drilling direction and reservoir pressure are directly dependent on the 3D state of stress.

In both research areas geomechanical models simulating the 3D state of stress often contain complex three-dimensional geological structures. Therefore, numerical methods such as the finite element (FE) method provide a useful tool to simulate and analyze geodynamic processes and study their impacts on the resulting state of stress. The FE method enables the accurate calculation of stresses for heterogeneous structures with complex geometries (faults, stratigraphic layers) and non-linear material behavior. The FE method has become a common tool and is utilized in a variety of studies (e.g. Chery et al., 2004, Eckert and Connolly, 2004, Parsons et al., 2006, Buchmann and Connolly, 2007).

A large number of numerical experiments focus on the change of in-situ stress due to injection or extraction of fluids on a reservoir scale (e.g. Rutqvist et al., 2006) or due to earthquake related co-seismic slip, e.g. Coulomb failure stress analysis (e.g. Stein, 1999, Parsons et al., 1999). These kinds of analysis only account for the relative change in stress in respect to an arbitrarily chosen initial state of stress. Numerical experiments which focus on processes such as faulting regimes, fracture likelihood or critical shear stress on a fault it is crucial to simulate the absolute 3D state of stress. Therefore, these models have to specify an initial stress state that both equilibrates gravitationally induced stresses and reproduces reasonable ratios of horizontal to vertical stresses with depth.

#### 3.2. Analysis and prediction of the horizontal state of crustal stress

The state of stress in the Earth's crust and its estimation and implementation in numerical modeling studies is an integral part in understanding many geotechnical problems. Of particular interest are the horizontal stresses arising because of the upper free-surface boundary condition imposed by the Earth's surface. Variations in the magnitude of the two ~horizontal (or in-plane) principal stresses are a dominant factor in anisotropic deformation in the majority of tectonic regions. The most common approach used to estimate the state of in-plane stress ( $S_H$ ) in the Earth's crust is to assume that all the constituent materials are isotropic and elastic and that these stresses are solely induced by

the Poisson effect of the gravitationally induced stress ( $S_V$  = density \* gravitational acceleration \* depth below surface). It can be shown via Hooke's Law that these assumptions lead to:

$$S_H = v / (1 - v) * S_V, \quad (3-1)$$

$$k = S_H / S_V, \quad (3-2)$$

where  $S_H$  is the mean horizontal stress,  $S_V$  the vertical stress, (weight of the overburden),  $v$  is the Poisson's ratio and  $k$  is the ratio of the mean horizontal to vertical stress.

Analyses based on this approach and which use a Poisson's ratio typical for crustal rocks (0.25; Turcotte and Schubert, 2002), result in a  $k$ -ratio of  $\sim 0.33$ . This  $k$ -ratio characterizes an extensional stress regime, i.e. only normal faulting earthquakes would occur under these conditions. Numerous in-situ stress measurements have demonstrated that this concept is incorrect in detail for the upper  $\sim 5$  km of the Earth's crust (e.g. Brudy et al., 1997, Hickmann and Zoback, 2004). A compilation of world-wide in-situ stress measurements is presented in Figure 3.1. It is clear that all the measured data have higher  $k$ -ratio's than the 0.33 value for  $k$  that an average crustal Poisson's ratio yields. The data clearly show that Poisson's constraint alone underestimates horizontal stress and that additional effects have to be considered.

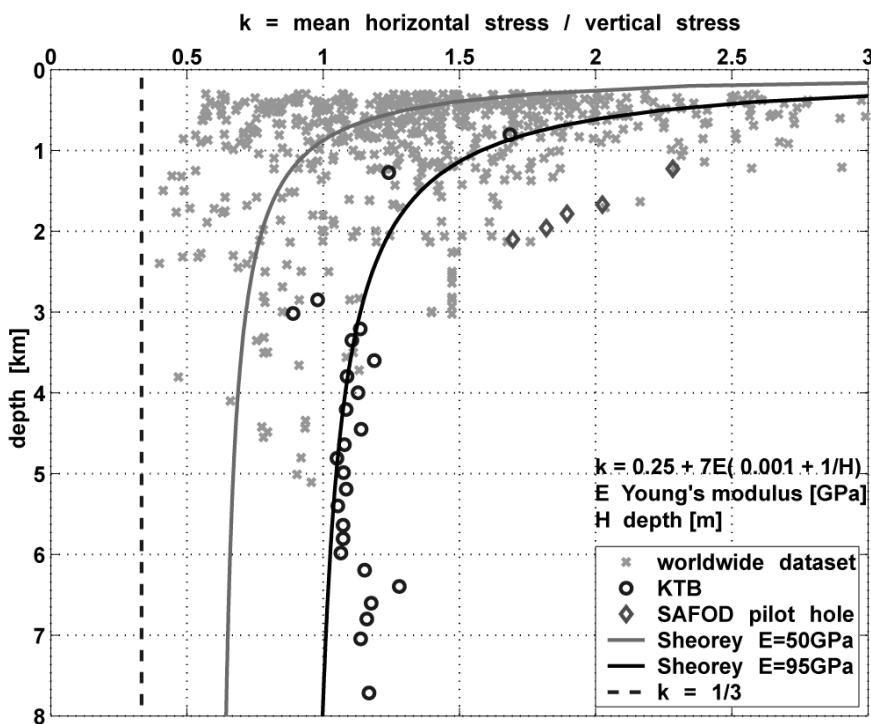


**Figure 3.1:** World-wide compilation of stress magnitude measurements (>300m depth; data compilation from Tobias Hergert) including data from the KTB site (Brudy et al., 1997) and the SAFOD pilot hole (Hickman and Zoback, 2004). Solid curves represent  $k$ -ratios ( $k = S_H / S_V$ ) after Sheorey (1994) for different Young's moduli. Dashed line is  $k$ -ratio after Poisson's constraint for  $v=0.25$ , i.e. modeling results from this study 2005. Special thanks goes to Tobias Hergert for providing the stress data.

A comprehensive approach to derive stress magnitudes that more closely match those observed in the crust was published by Sheorey (1994). Sheorey assumed a 1D layered spherical model of the Earth and considered the structure of crust and mantle in terms of elastic properties, density, temperature gradient and the temperature dependent thermal expansion coefficient. Sheorey (*op cit*) argued that stress in the upper crust, and thus the k-ratio, is a result of equilibrium between gravitational compaction and thermal expansion. This means that surficial stress depends on material properties and state variables down to the Earth's core. For the uppermost kilometers of the crust Sheorey (1994) derived the following empirical approximation for the k-ratio:

$$k = \frac{\nu}{1-\nu} + \frac{\alpha EG}{(1-\nu)\gamma} \left(1 + \frac{1000}{H}\right) \quad (3-3)$$

which can be simplified to:

$$k = 0.25 + 7E (0.001 + 1/H) \quad (3-4)$$

where E is the Young's modulus (GPa),  $\gamma$  is the unit rock pressure,  $\alpha$  is the coefficient of linear thermal expansion, G is the thermal gradient,  $\nu$  is the Poisson's ratio and H depth (m).

Figure 3.1. shows two curves based on Sheorey's formula for the k-ratio against depth. The first for E=50 GPa corresponds to the value that Sheorey (1994) assumed for the uppermost crust, which is a good average of the data cloud of worldwide stress measurements. The curve obtained for E = 95 GPa provides a very close fit to data from the KTB borehole in southeast Germany, which correlates to the elasticity reported by Brady et al. (1997). The KTB drilling site is located on the western flank of the Bohemian Massif, a tectonically quiescent region with low topographic relief. This setting corresponds well to the boundary conditions in Sheorey's (1994) theory. At the SAFOD pilot hole near the San Andreas Fault, California, the k-ratio is higher than at KTB (Figure 3.1; Hickmann and Zoback, 2004), presumably due to tectonic and/or topographic loading effects. In cases where plate tectonics and/or geological features such as faults and topography become relevant, the additional complexity is most readily addressed using a numerical modeling approach.

### 3.3. Numerical modeling of in-situ stresses

The accurate numerical simulation of the 3D in-situ stress state of a volume of rock representing a part of the Earth is a task that requires care. In nature, this volume of rock is exposed to boundary conditions such as static, dynamic and thermal loads, acting over geological time scales. In order to simulate the present-day state of stress, an initial state of stress has to be defined that represents the long-term genesis of the geological volume. Since it is currently impossible to simulate this genesis in great detail, an applicable procedure has to be developed that yields initial in-situ stress conditions that equilibrate gravitationally induced stresses and which are consistent with the observations from in-situ stress measurements and models such as Sheorey's.

### 3.3.1. Technical problems

As an initial example a simple geologic setting representing a tectonically quiet intra-plate region with a flat topography, where lateral density inhomogeneities are neglected, is assumed. A 3D rectangular box representing the model volume is the most commonly used boundary geometry in 3D numerical modeling (Figure 3.2). The boundary conditions on the sides allow in-plane displacements (rollers), i.e. vertical compaction, and the bottom boundary conditions either allow in-plane displacements or are represented by elastic springs. Typical rheological parameters for rocks within the Earth's crust are used (e.g.  $\rho=2700\text{kg/m}^3$ ,  $v=0.25$ ,  $E=50\text{GPa}$ ; Turcotte and Schubert, 2002). This model is referred to as M1 in the following sections.

The generation of an initial state of stress is critically dependent on how gravity (and/or other body forces) acts. The application of gravity to the numerical model leads to an instantaneous elastic compaction of the volume. The state of stress resulting from this deformation yields horizontal stresses which depend exclusively on the induced vertical stresses and are consistent with the Poisson's effect in a homogeneous elastic medium.

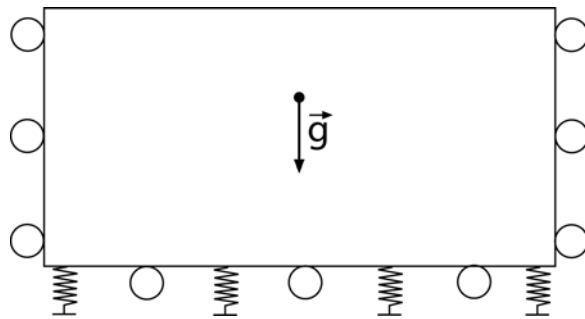


**Figure 3.2: Commonly used 3D rectangular box for simulation of a gravity dependent state of stress, referred to as M1. Boundary conditions typically used are rollers (circles) or elastic springs.**

The resulting horizontal stresses are only dependent on the Poisson's ratio assigned and thus the k-ratio is typically  $\sim 0.33$  with depth (M1 in Figure 3.3). This state of stress yields extensional stress conditions, i.e. a normal faulting regime with  $S_V \gg S_H > S_h$  throughout the crust. This is not consistent with the more compressional state of stress generally observed in the Earth's crust (e.g. Brudy et al., 1997). The k value obtained from the 3D rectangular box is 0.3-0.4 lower than the prediction of Sheorey's model (and by implication real data) for  $E=50\text{GPa}$  (Figure 3.3). Furthermore, the shape of the Sheorey curve, in which k increases significantly near surface, is not reproduced.

The results of M1 demonstrates that the standard modeling approach is inappropriate to generate a “realistic”/reasonable initial state of stress. The 3D rectangular box modeling approach clearly demonstrate that important processes generating the in-situ state of stress are not being considered. Firstly, the FE mesh compacts instantaneously under gravity and thus the compaction history of rock volumes is not considered. Secondly, the interaction of thermal expansion and gravitational compaction, as represented in Sheorey's model, is not considered. Third, the spherical shape of the Earth, an important factor in generating horizontal stress, is neglected in the 3D rectangular box

model. Furthermore, pore pressure is an important parameter in generating a more isotropic state of stress resulting in higher k-ratios.

Ideally, 3D models should include processes presented by models such as Sheorey's and additionally include pore pressure. However, this would significantly increase the dimension of the model (down to the earth's core) and would require the implementation of thermally induced stresses and of poro-elastic materials. The dimensions of 3D numerical models and the use of poro-elastic elements are still a critical issue in terms of computational time. Therefore, an applicable technical procedure has to be found that accounts for Sheorey's observations without substantial increase of the model dimension and rheological complexity.

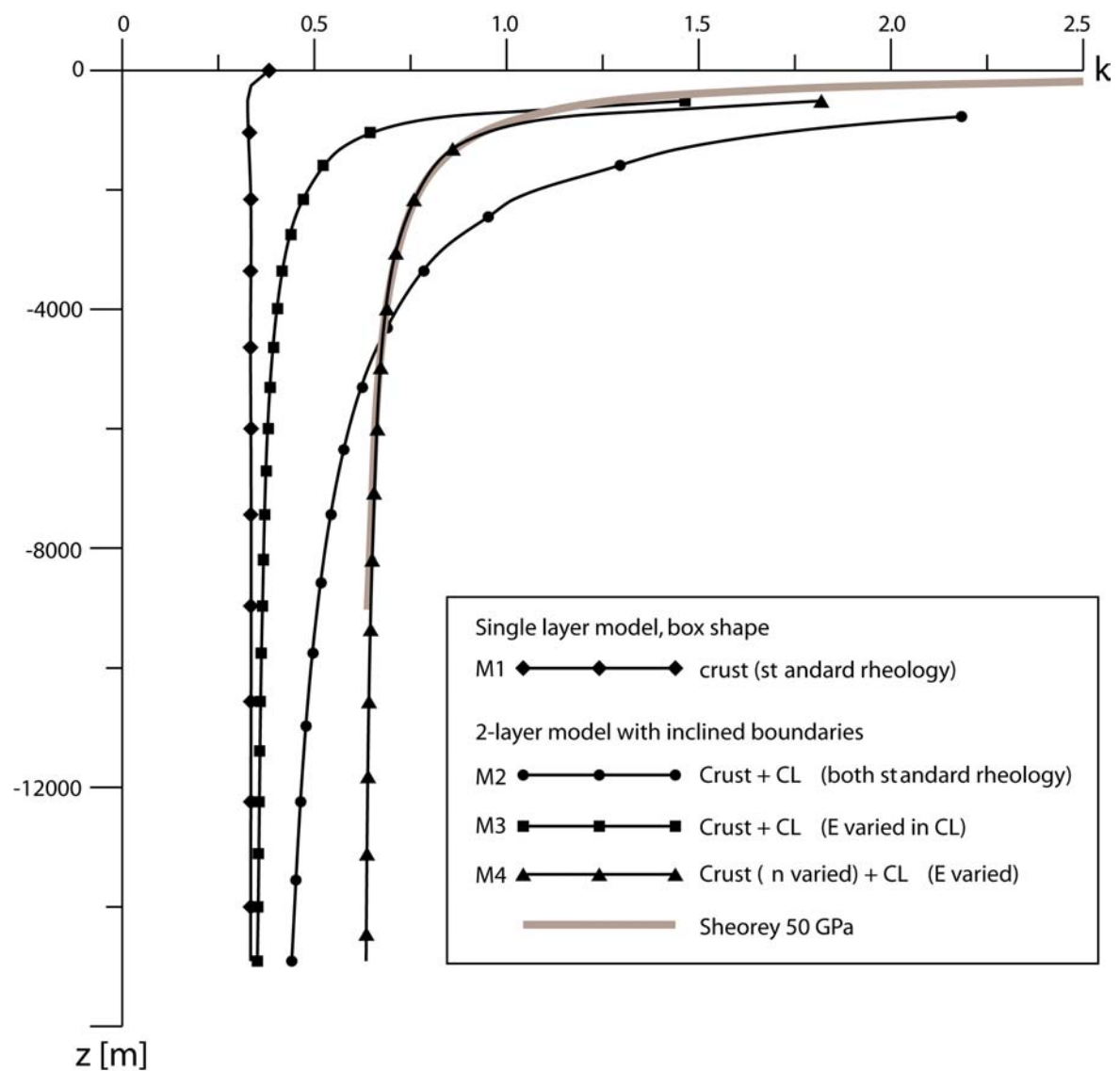


**Figure 3.3: k-ratios for the various modeling approaches. M1 shows the underestimation of horizontal stress in the most common used modeling approach. M4 yields a good fit to Sheorey's observations for the presented procedure to model an initial state of stress.**

Model	Model components	Thickness [km]	E [GPa]	$\nu$	$\rho$ [kg/m <sup>3</sup> ]
Model 1	Crust	50	50	0.25	2700
Model 2	Crust + load frame	50	50	0.25	2700
	Compaction layer	100	50	0.25	2700
Model 3	Crust + load frame	50	50	0.25	2700
	Compaction layer	100	750	0.25	2700
Model 4	Crust + load frame	50	50	0.382	2700
	Compaction layer	100	750	0.25	2700

Table 3.1: Rheologies used for the various modeling steps. Description of the various models and the “term” load frame follows in the text.

### 3.3.2. Solution proposed for the limitations of a 3D rectangular box model

In this section an approach is introduced that enables simulation of an initial 3D state of stress similar to the majority of in-situ data, Sheorey’s observations and thus yields more realistic horizontal stress magnitudes than a classical 3D rectangular box approach. In order to simplify the interaction of gravitational compaction and thermal expansion the technical procedure presented mimics the compaction processes using a 2-layer model geometry (Figure 3.4).

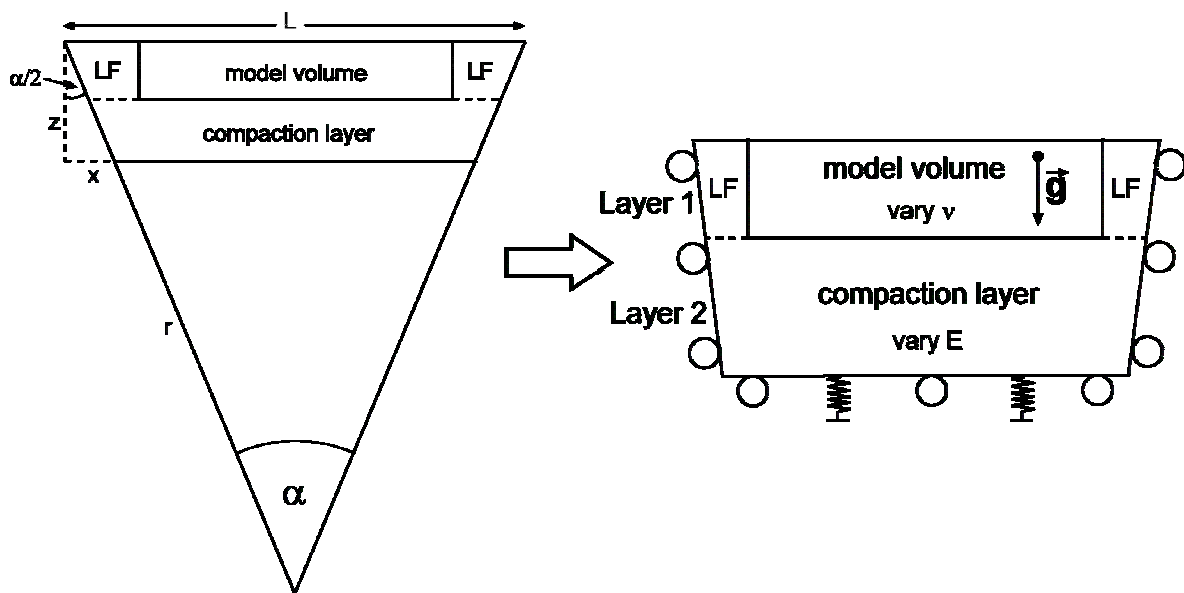


Figure 3.4: Two layer model geometry with inclined boundaries proposed. The model volume is implemented in a load frame (LF) and underlain by a compaction layer. The corner coordinates of the compaction layer (CL) are calculated as follows (here exemplified for the x-coordinate in a N-S oriented model). After the law of cosines, the angle  $\alpha$  is given by:  $\cos \alpha = 1 - L^2 / 2r^2$ , with  $L$  = model length and  $r$  = radius of the earth. The distance  $x$ , to calculate the bottom coordinates, follows:  $x = z \tan(\alpha/2)$ .

For the new model geometry the model volume (MV, M1) is implemented in a larger model volume, the so-called load frame. The model now features 2 layers (Figure

3.4). The first layer includes the MV and the load frame. The second layer represents an “artificial” compaction layer that allows the model to compact sufficiently so that the lateral compression yields a realistic k-ratio. Both layers have inclined model boundaries accounting for the spherical shape of the Earth. The model has dimensions of 200km by 200km laterally and a depth of 50km. The compaction layer is 100km thick. In total, 234,665 tetrahedral elements are used.

For the initial model (M2) a homogeneous rheology for both layers (Table 3.1) is assumed. This model generates k-ratios generally consistent with Sheorey’s model, i.e. increasing horizontal stresses near surface (M2 in Figure 3.3). The inclined model boundaries lead to higher k-values due to a non-linear increase of horizontal compaction. However, neither the shape of the Sheorey curve nor the curves’ position is matched. This indicates the importance of the total amount of elastic compaction, which is critical when attempting to replicate the shape of the k-curve.

The next model (M3) used different material properties for the two layers. The material properties of layer 1 match those of in-situ observations, i.e.  $\rho=2700\text{kg/m}^3$ ,  $v=0.25$ ,  $E=50\text{GPa}$  (Table 3.1). The compaction layer has the same density and Poisson’s ratio but the Young’s modulus in the compaction layer is varied until the shape of the Sheorey curve of  $E=50\text{GPa}$  (M3 in Figure 3.3) is resembled. It should be noted that the sensitivity of the k-ratio to the amount of compaction and model size (depth) precludes a simple derivation of a “rule of thumb” for the thickness of the compaction layer.

Iteration of the best fit value to use for Young’s modulus of the compaction layer enables a close match to the shape of the k-curve but not the magnitudes, which remain too low. Due to the missing pore pressure in the model the state of stress is to anisotropic. As mentioned in section x.x the implementation of poro-elastic elements is not applicable and thus, in order to fit the Sheorey curve the Poisson’s ratio in layer 1 needs to be increased (Table 3.1, M4 in Figure 3.3). This does not change the shape of the k-curve but shifts it towards higher values, since greater horizontal strain, and hence stress, are now induced for a given vertical strain (due to gravity loading).

The resulting state of stress can now be exported for the area of the initial model volume (MV in Figure 3.4) and then be imported as an initial state of stress for an undeformed stress-free model (M5) which features the actual, “realistic” elastic parameters for the Young’s modulus and the Poisson’s ratio. Since the forces calculated in M4 are in equilibrium, negligible displacements and thus no significant change in the initial stress state will occur when gravity is applied to M5. Hence, the procedure presented equilibrates the gravitational stresses and yields horizontal stresses in a zero topography situation consistent to Sheorey’s analytical model. This so-called “gravitationally pre-stressed” model can now be subjected to boundary conditions such as those mimicking tectonic loads and the change of absolute in situ stress due to these processes can be investigated.

The variation of the Poisson’s ratio in the first modeling phase, which obtains the initial stress conditions, and which seems to be arbitrary, accounts for the compaction history of rock volumes and the fluid content of the rock volume. During formation most rocks exhibit a higher fluid content than subsequently. In metamorphic and igneous rocks (re-)crystallization is typically a series of dehydration reactions whilst in sediments water

is lost during compaction. Thus, early in their history, a rock volume has a relatively high effective Poisson's ratio ( $\nu$ ) since part of it is filled by pore fluid. During the dehydration/compaction process  $\nu$  reduces to commonly observed values of 0.25 - 0.3. In summary, the high value of ~0.4 for the Poisson's ratio in the procedure of simulating the initial state of stress aims to mimic the entire compaction history within a single modeling step and further accounts for the existence of pore pressure in an effective state of stress.

### 3.3.3. Summary of the pre-stressing procedure

The practical implementation of the methodology discussed above is summarized so as to establish numerical models that are capable of reproducing a realistic, 3D state of stress. In total the pre-stressing procedure involves 5 steps (Figure 3.5):

1. Add load frame and compaction layer with inclined model boundaries to the model volume.
2. Vary Young's modulus of compaction layer and Poisson's ratio of the upper layer. This represents an iterative procedure until the k-value of the Sheorey curve is fitted sufficiently.
3. Export the stresses in the area of the model volume of interest (MV).
4. Import these stresses as an initial state of stress for a new undeformed, stress-free model volume with the actual elastic properties.
5. Apply boundary conditions mimicking e.g. tectonic loads

### 3.4. Summary and discussion

The remarkable fit of Sheorey's analytical model to k-values from global stress magnitude measurements emphasizes the importance of the ratio between modeled horizontal and vertical stresses. The correct implementation of an initial stress field in numerical models is essential to simulate stress conditions that are capable of reproducing the absolute state of stress and thus generate compressional stress regimes near surface as observed by Brady et al. (1997). The pre-stressing procedure presented describes a simple technical procedure which yields stress states that fit Sheorey's observations for k. It should be noted that the approach presented is generally valid for homogeneous models with a flat topography. For models incorporating significant geometrical and rheological heterogeneity it may prove impossible to precisely reproduce k-curves that resemble Sheorey's observations. In this case, one or more best -fit(s) initial stress states must be determined and the most appropriate one must be calibrated after application of the contemporary tectonic processes. However, in most cases the pre-stressing procedure is applicable even when topography and lateral inhomogeneities are present. In these cases the fit has to be carried out in a region of the model where topography is flat and where lateral density variations are small.

It is important to note that the presented approach does not represent an alternative to Sheorey's model but rather acts as a technical makeshift to accomplish an initial state of stress at low computational and time costs. A point of criticism may be the arbitrary increase in Poisson's ratio for layer 1 in Step 2. However it should be emphasized that this

is only conducted in Step 2 to achieve the initial state of stress, but not for the final model run (Step 5) which accounts for the actual elastic properties.

Thus, in comparison to the standard rectangular box modeling procedure, the pre-stressing procedure represents a significant improvement in numerical modeling especially when parameters depending on the absolute state of stress are investigated.

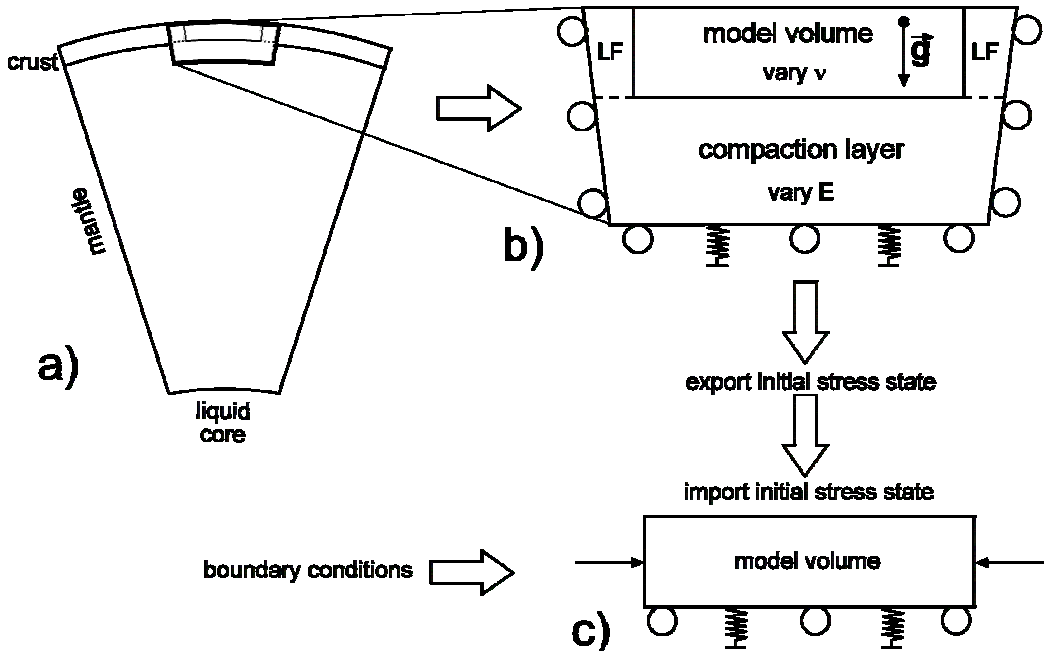


Figure 3.5: Modeling procedure proposed in this study. a) The model volume of interest represents only the uppermost part of the layered, spherical Earth model of Sheorey. b) In order to approximate the interaction of compaction and thermal expansion processes in Sheorey's model, the model geometry is simplified with a 2-layered model including the compaction layer. During this step,  $E$  in the compaction layer and  $v$  in the model volume and load frame are varied. This procedure allows matching  $k$ -ratios consistent with Sheorey's model and an initial state of stress is obtained. c) For application of additional boundary conditions in subsequent steps, only the model volume is used and assigned with standard values for  $v$ .



## 4. Crustal state of stress in California and the role of the San Andreas Fault

### 4.1. Scope

The Pacific-North American plate boundary, including the San Andreas Fault (SAF), represents one of the most interesting examples for studying the interaction of the different contributions to the 3D crustal state of stress. Using 3D finite element analysis the scope of this chapter is to investigate on how (1) gravitational potential energy differences ( $\Delta GPE$ ) from topography, (2) plate boundary forces and (3) fault geometries influence the 3D crustal state of stress. Comparison to independent stress orientations, magnitudes and observed tectonic regimes shows that the modeling approach reproduces the absolute crustal state of stress. Once the numerical models are calibrated the role of the coefficient of friction,  $\mu$ , on the SAF is studied. Of particular interest is the influence of  $\mu$  on the orientation of the maximum horizontal stress component,  $S_H$ .

### 4.2. Introduction

Deformation in the western United States (WUS) and especially close to the Pacific-North American plate boundary is spatially complex. While extensional deformation dominates in the continental interior, i.e. in the Basin and Range province, dextral shear is accommodated and partitioned between the San Andreas Fault (SAF) system and the Eastern California Shear Zone (ECSZ, e.g. McClusky et al., 2001, Miller et al., 2001). Many recent studies have focused on the interaction of extension in the Western United States continent and plate boundary tectonics along the SAF (e.g. Bohannon and Parsons, 1995, Atwater and Stock, 1998; Sonder and Jones, 1999; Flesch et al., 2000; Jones et al., 2004).

To understand the different deformation styles observed, the sources that contribute to the crustal state of stress and how they interact become of particular interest. The state of stress in the lithosphere is the result of plate boundary forces, gravitational potential energy differences ( $\Delta GPE$ ) and basal shear tractions (e.g. Fleitout et al., 1991; Richardson and Reding, 1991; Sonder and Jones, 1999). Jones et al. (1996) suggested that buoyancy forces arising from GPE variations are sufficient to explain a variety of different deformation styles in the WUS Cordillera. However, this does not seem to apply for the state of stress for the Pacific Plate – North American plate boundary along the SAF. Flesch et al. (2000) showed that approximately equal interaction of  $\Delta GPE$  and plate boundary forces reproduce the observed deformation and stress field. In a more recent study, Flesch et al. (2007) conclude that the deviatoric stress field can be explained by equal interaction of  $\Delta GPE$  and a combination of plate boundary forces and basal tractions. Humphreys and Coblenz (2007) model the contributions to the state of stress in America by applying a large variety of forces on the margins (boundary loads), base (basal tractions) and interior ( $\Delta GPE$ ) of the plate. For the WUS they conclude that extension is driven by high GPE, root drag and an outward pull at southern Cascadia. Li and Liu (2006) associate stress and strain changes in southern California to the complexity of the geometry of the SAF, especially in the Big Bend region. Thus active faults and seismicity in the ECSZ might be directly related to the geometry of the SAF, as observed by Du and Aydin (1996).

The quantitative modeling studies presented above are either based on 2D assumptions and thus a vertically averaged state of stress or neglect GPE. The study presented in this chapter uses 3D finite element analysis (FEA) to investigate the interaction of  $\Delta$ GPE due to surface topography, plate boundary forces and the geometry of the San Andreas Fault on the crustal state of stress. Basal tractions are neglected for simplicity and are furthermore considered to be relatively small (e.g. Zoback, 1992; Liu et al., 2007). The focus of this study is on the upper, brittle 15km of the crust and crustal thickness variations with depth are neglected. An implicit assumption is that the models are in isostatic equilibrium and that  $\Delta$ GPE result from surface topography changes. The modeling approach tries to simulate the absolute 3 dimensional stress tensor, such that modeled stress orientations, magnitudes and deformation styles are calibrated against independent stress orientations and magnitudes.

### 4.3. Californian stress field

The central and southern California stress field has been the focus of many studies (e.g. Zoback et al., 1987; Scholz, 2000; Hardebeck and Hauksson, 2001; Hardebeck and Michael, 2004; Townend and Zoback, 2004). In general, three major stress provinces can be distinguished: (1) Western California in the vicinity of the SAF exhibits strike-slip and compressional deformation and shows  $\sim$ N45°E orientations of the maximum horizontal stress component  $S_H$  (Mount and Suppe, 1987; Townend and Zoback, 2004; Provost and Houston, 2003). (2) Southern California, which exhibits a more complex state of stress: Hardebeck and Hauksson (2001) inferred an average  $S_H$  orientation of  $\sim$ N7°E, but also observe variations of N30°-45°E. Townend and Zoback (2004) observe a relatively uniform  $S_H$  orientation of  $\sim$ N22°E throughout southern California. (3) The Eastern California Shear Zone (ECSZ) north of the Garlock Fault (GF) is situated in a transition zone between E-W extension in the Basin and Range (B&R) province and dextral strike-slip tectonics from the plate boundary and has  $S_H$  generally oriented N22°E (e.g. Zoback, 1989; Unruh et al., 2002; Hardebeck and Hauksson, 2001). In the ECSZ, south of the Garlock Fault, Hardebeck and Hauksson (2001) observe a distinct stress state with  $S_H$  oriented N20°-45°E.

### 4.4. Model

**Geometry and rheology:** Linear elastic material properties are applied to model the upper 15km of the lithosphere. The 3D geometry comprises the topographic and bathymetric surfaces of California and the Pacific Plate (Figure 4.1). The WUS continent, intersected by the major active faults of the ECSZ (the Owens Valley Fault, Panamint Valley-Hunter Mountain Fault, Death Valley Fault, Garlock Fault; after Jennings, 1994), the Pacific Plate (PP) and the Sierra Nevada – Great Valley (SN-GV) microplate are represented as rheological contrasts (Table 4.1). The SAF separates the PP from the continent. The average mesh dimension is 5km and a total of  $\sim$ 385500 hexagonal elements have been used.

**Loading conditions (Figure 4.1):** The model is loaded by gravity and the PP plate motion is simulated by treating the part of the PP, which is bound by the Patton Escarpment, as a

rigid body with a constant velocity of 47mm/yr oriented N37°W. The southeastern model boundary also has PP motion applied to it. At the eastern model boundary, north of the SAF, Basin and Range (B&R) tectonics are mimicked by 3mm/yr east-west displacement. The boundary conditions for the southeastern model boundary are a linear interpolation between PP motion and B&R tectonics. The northern and basal model boundaries are constrained so that only in-plane motion is allowed. All faults are vertical and are included as frictional contact surfaces (coefficient of friction  $\mu=0.6$ , after Byerlee 1978) separated by split nodes, which allow in-plane fault motion but no separation.

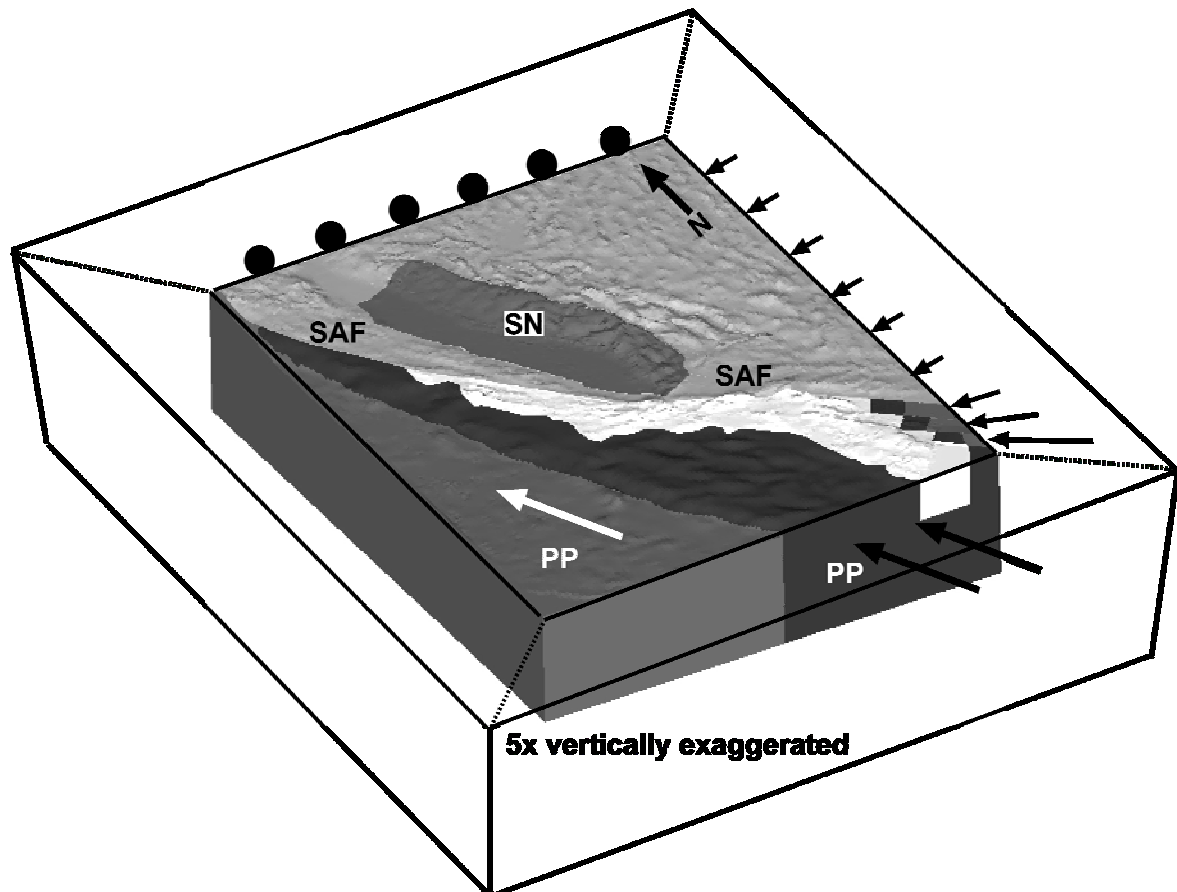


**Figure 4.1: 3D model sketch:** The model comprises the WUS continent, intersected by the major active faults of the ECSZ (after Jennings, 1994), and the PP. The two blocks are separated by the SAF. The arrow indicates PP motion. The circles indicate “roller” boundary conditions, i.e. in plane motion is allowed. The loading frame was used only for the “gravity only” model.

#### 4.5. Loading procedure

(1) **Gravitational pre-stressing:** The procedure described in chapter 3 is applied to receive an initial stress state. In order to receive “realistic” horizontal stress magnitudes, k values obtained in the gravitational loading step are calibrated to Sheorey’s model (Figure 4.2). The loading frame with inclined model boundaries has a base of compaction at 300km depth. The Poisson’s ratio ( $\nu$ ) and the Youngs modulus of the loading frame are varied until “realistic” k values are generated (Table 4.1). Once the modeled k is calibrated against a typical k path (Sheorey; 70 GPa, Figure 4.2) the stresses obtained are used as the

initial stress state to which tectonic loads are applied. A better fit to the Sheorey path (as described and shown in chapter 3) is prevented by the coarse model resolution of  $\sim 5\text{km}$  as an average element size.

(2) **Tectonic loading:** In this study the magnitude of tectonic loading is constrained by the state of stress predicted. The model results are compared to stress dependent tectonic regimes and focal mechanisms at certain depths. For example, strike slip focal mechanisms in the ECSZ generally occur at depths of  $\sim 5\text{km}$ . A good calibration in this region occurs if the model predicts strike-slip or transtensional deformation at  $z=-3000\text{m}$ . Furthermore, predicted stress magnitudes are compared to stress measurements at three different locations: at the Cajon Pass, at the SAFOD pilot hole and at the Coso Geothermal Field.

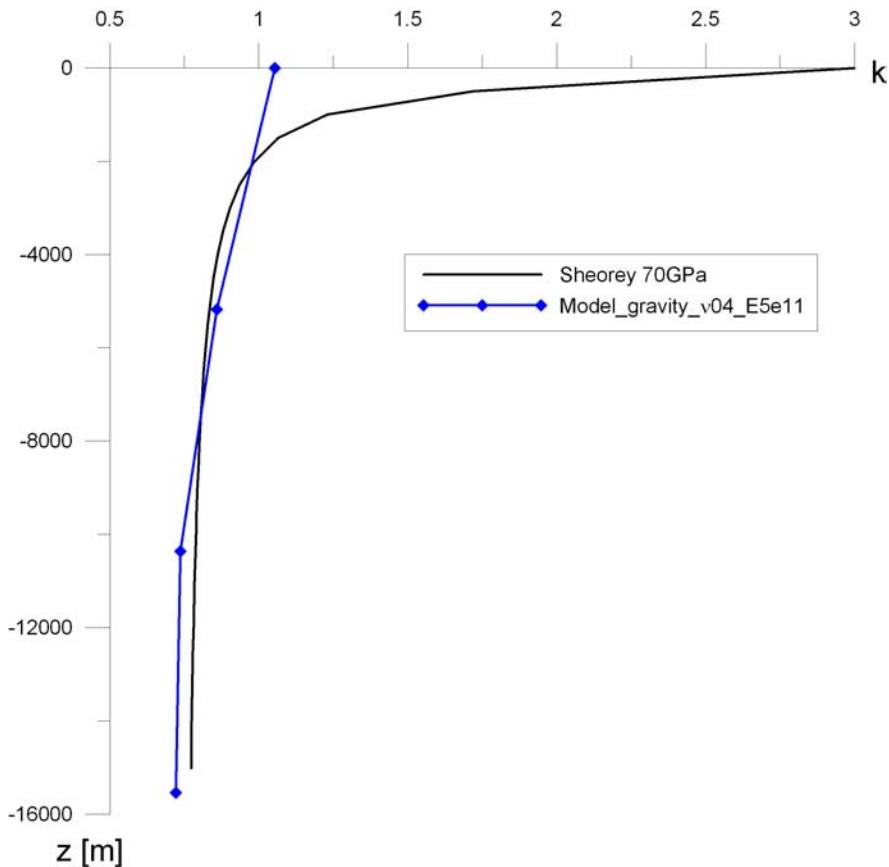


**Figure 4.2:** The resulting horizontal stress magnitudes after the gravitational pre-stressing are calibrated against the Sheorey graph of 70 GPa. A better fit especially close to surface is prevented by the coarse mesh resolution.

	Gravitational Loading			Tectonic Loading		
	$\rho [\text{kg}/\text{m}^3]$	$v$	$E [\text{Pa}]$	$\rho [\text{kg}/\text{m}^3]$	$v$	$E [\text{Pa}]$
Frame	2750	0.4	5.0 E11			
WUS	2700	0.4	5.0 E10	2700	0.25	5.0 E10
PP	3200	0.4	10.0 E10	3200	0.275	10.0 E10
SN	2700	0.4	7.5 E10	2700	0.275	7.5 E10

**Table 4.1:** Rheologies used for the loading steps described in chapter 3.

## 4.6. Results

To investigate the effects of the interaction between gravitational potential energy (GPE) and Pacific Plate (PP) motion on the Californian stress field gravity driven models are compared to models, in which the gravitational stress state has PP motion applied to it in steps equivalent to 10000yrs to 30000yrs of loading. The results presented in the following paragraphs are plotted on horizontal planes at  $z=-3000\text{m}$  as a representative of the seismogenic zone where most earthquakes occur.

### 4.6.1. Application of ‘gravity only’ to the model (Figure 4.3a,b)

**Tectonic regimes:** The Regime-Stress-Ratio (RSR; see chapter 2.7) in the “gravity only” model run distinguishes two areas. The majority of the model is dominated by extension, whilst a corridor adjacent to the SAF (0-150km) exposes increased horizontal stresses and thus has a transpressional to compressional state of stress.

**$S_H$  orientation:** Gravitational loading results in an irregular  $S_H$  orientation. The Basin and Range and the ECSZ exhibit no preferred orientation of  $S_H$ . In a 100km-150km from the SAF north of the Big Bend  $S_H$  is oriented N40°E-N55°E, approximately perpendicular to the SAF. The Sierra Nevada-Great Valley exhibits its own stress field (N20°W-N30°W).

The variability in  $S_H$  shows that the topography has a strong effect on the resulting stress orientations. Furthermore, the Sierra Nevada (SN) together with the high GPE in the eastern model area cause significant SAF normal compression.

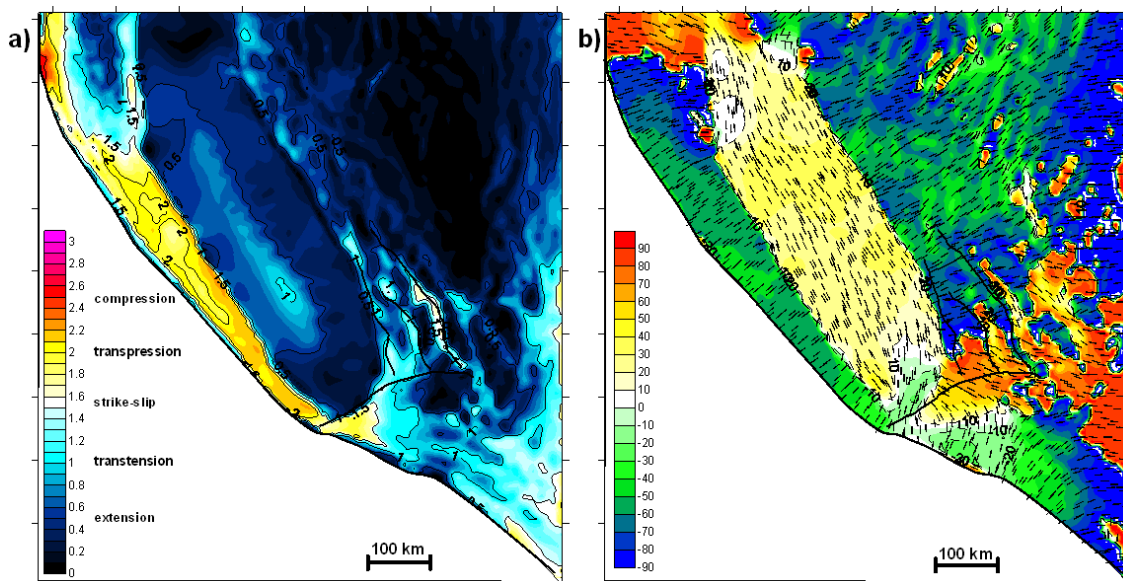


**Figure 4.3:** a) RSR contours for “gravity only” yield extensional tectonics for the majority of the model. North of the Big Bend segment the SAF is situated in a more compressional tectonic regime. b)  $S_H$  orientations are irregular and do not show preferred orientations.

### 4.6.2. Pacific Plate motion analysis

**Tectonic regimes:** To obtain the best-fit PP loading magnitude, PP motions equivalent to between 10ka and 30ka were studied. Applying loads equivalent to ~10ka of deformation yields results in which most of the model, similarly to the gravity case, is dominated by

extension. Loading magnitudes equivalent to greater than 20ka of deformation result in greater compression than seen in nature and is clearly overloading the model. The best-fit results are obtained for loading equivalent to ~20ka of PP motion. This model yields stress regimes most consistent with Californian geology, focal mechanisms and stress inversion data (Hardebeck and Hauksson, 2001). In particular, gravitational pre-stressing and tectonic loading of 20ka establishes several Regime-Stress-Ratio (RSR) provinces (Figure 4.4a):

- (1) Strike-slip to transpression in central California adjacent to the SAF (0-200km).
- (2) A transition of transpression in the BB area to strike-slip and transtensional regimes in the MB.
- (3) The ECSZ is transition zone of extension in the B&R and strike-slip in the MB.
- (4) Extensional deformation in the B&R

The Sierra Nevada and the Basin and Range in the east are the regions with the highest GPE and thus most likely to be dominated by extensional tectonics. The coastal areas with lower GPE are dominated by transpression and strike-slip regimes. The interaction between  $\Delta$ GPE and the plate boundary forces becomes most evident in the ECSZ. The ECSZ is interpreted to be a transition zone between extension in the Basin and Range and strike slip deformation from the NA-PP interaction (e.g. Hearn and Humphreys, 1998; Bennett et al., 2003). Calculating the Regime-Stress-Ratio using the modeled stress field produces values consistent with these independent observations such as a transtensional regime in the ECSZ in the upper ~5km of the crust.

The compression imposed by the bending geometry of the SAF is the main factor for transferring strike-slip deformation into the ECSZ. This can be seen east of the Sierra Nevada, where a corridor of transtension extends from the ECSZ south and north of the Garlock Fault along the Walker Lane Belt to the northern model boundary.

**$S_H$  Orientation:** After adding the equivalent of 20ka PP motion to the gravitational stress state,  $S_H$  is oriented N10°E-N25°E in the B&R, in the ECSZ north of the Garlock Fault and in the Sierra Nevada (Figure 4.4b). In the Mojave Block  $S_H$  orientations are ~N15°E. Close to the SAF, near the Big Bend, orientations vary between N10°E and N20°E but are generally close to the regional trend. North of the Big Bend, along the SAF,  $S_H$  is N15°E-N25°E. In the area of the Salton Trough the model predicts  $S_H$  at ~N25°E. Compared to the  $S_H$  orientations predicted by the 'gravity only' model the stress field further than ~150km from the fault is significantly changed by the plate motion. Especially in the ECSZ, Basin and Range and in the Sierra Nevada a distinct stress field is observed after PP motion is applied.

Finally, the model results are compared to  $S_H$  orientations from the World-Stress-Map (WSM, Heidbach et al., 2007). An algorithm by Müller et al. (2003) is used to generate an interpolated grid of the WSM orientations and then the model results are subtracted to obtain a misfit (Figure 4.4c). The predicted  $S_H$  have a good fit to the WSM data, especially north of the Big Bend, in the Mojave Block and in the ECSZ where the misfit is less than 10°. In general, the predicted  $S_H$  orientations do not vary more than 20° from the WSM ones indicated by the green and yellow contours. The root-mean-square (RMS) of  $S_H$  orientation difference is 14.2°. This is within the error range (10-25°) of  $S_H$ .

orientation for the WSM ‘A-C’ quality data used. The largest discrepancies (-25° to -40°) occur in the northwest model corner in the vicinity of the Mendocino triple junction, which is not included in the model, but which might significantly influence the stress field.

**Stress magnitudes:** The resulting stress magnitudes for the maximum and minimum horizontal stress component,  $S_H$  and  $S_h$ , as well as the vertical stress component,  $S_V$ , are compared to measured and estimated magnitudes at the SAFOD pilot hole (Hickman and Zoback, 2004), at the Coso Geothermal Field (Sheridan and Hickman, 2004) and at the Cajon Pass (Zoback and Healy, 1992). In Figure 4.5 the lines represent the modeled magnitudes and the diamond glyphs the measured data. As indicated by the RSR results, the tectonic regimes, i.e. the relative positions of  $S_H$ ,  $S_h$ , and  $S_V$  are matched for all three sites.  $S_h$  is matched very well for all locations. The modeled stress path passes through the data points.  $S_V$  is slightly overestimated for all locations since the density does not vary with depth.  $S_H$  yields a good fit for SAFOD, is slightly overestimated for Coso and large discrepancies occur for Cajon Pass. The high  $S_H$  magnitudes at the Cajon Pass might result from the bending geometry of the SAF in the model, representing a more convergent boundary than north of the BB and thus resulting in high horizontal stresses. In nature the strain in this region is partitioned between the SAF, the San Jacinto Fault and the El Sinore Fault and thus lower  $S_H$  magnitudes are observed at Cajon Pass.

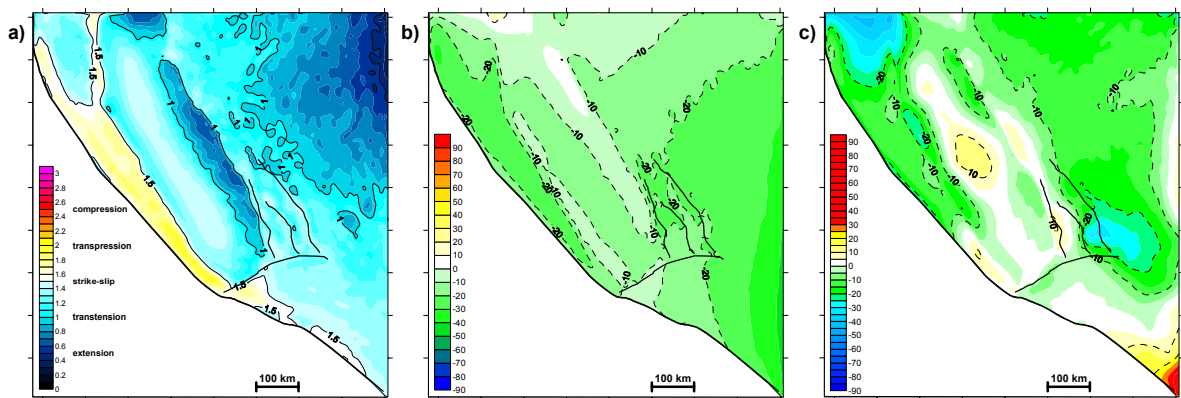


**Figure 4.4:** a) Regime-Stress-Ratio (RSR; chapter 2.7) for gravity plus tectonic loading yields transtension in the ECSZ, extension in the B&R and the SN, and strike-slip to transpressional tectonics along the SAF. b)  $S_H$  orientation for gravity plus tectonic loading shows distinct stress orientations of N10°E-N25°E. c) Difference of  $S_H$  orientation compared to WSM orientations. Predicted  $S_H$  orientations do not vary more than 20° from the WSM ones indicated by the green and yellow contours.

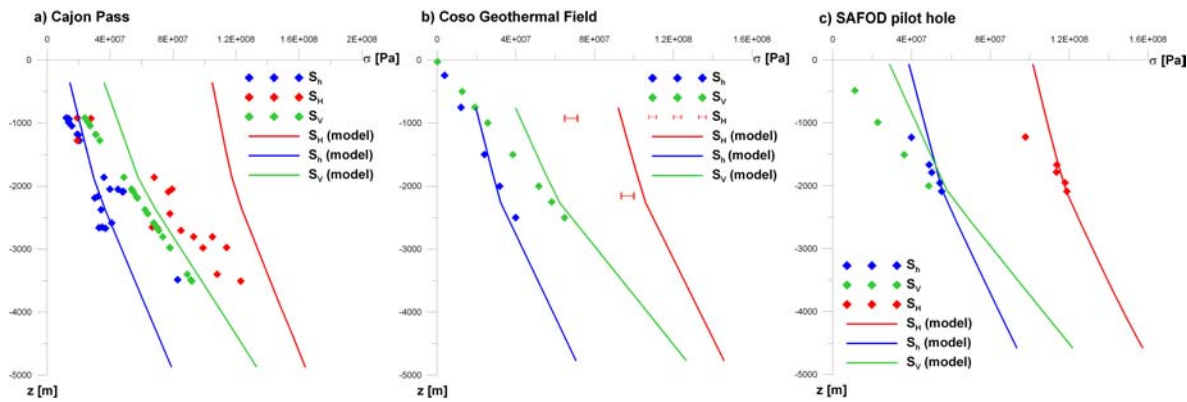


Figure 4.5: Stress magnitudes for a) Cajon Pass, b) Coso Geothermal Field, c) SAFOD pilot hole.  $S_h$  is matched very well for all locations.  $S_H$  yields a good fit for SAFOD, is slightly overestimated for Coso and large discrepancies occur for Cajon Pass.

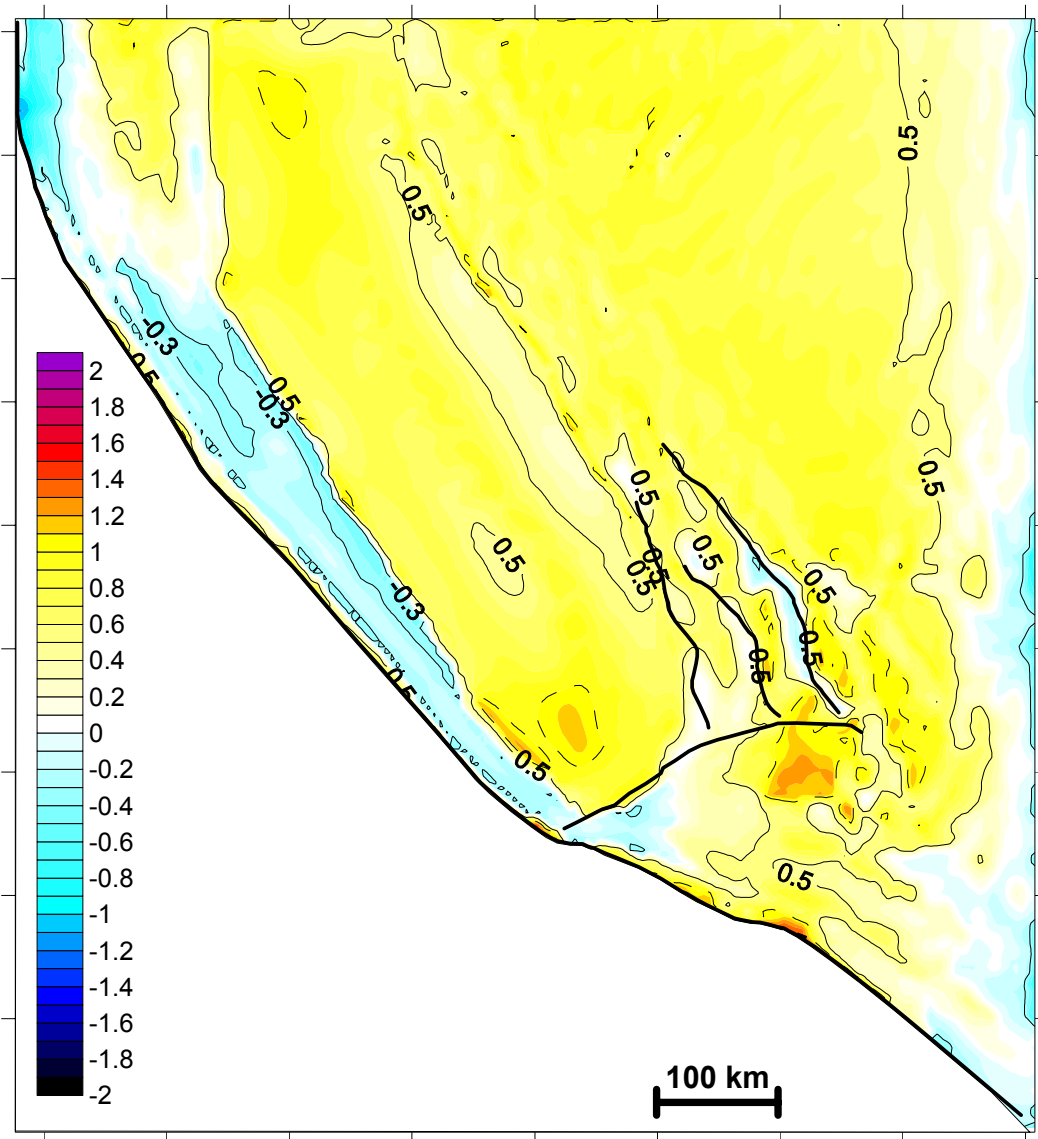


Figure 4.6: Regime-Stress-Ratio (RSR) difference between the tectonic loading model and the gravity only model shows the influence of the bending geometry of the SAF. Compression is transferred into the ECSZ.

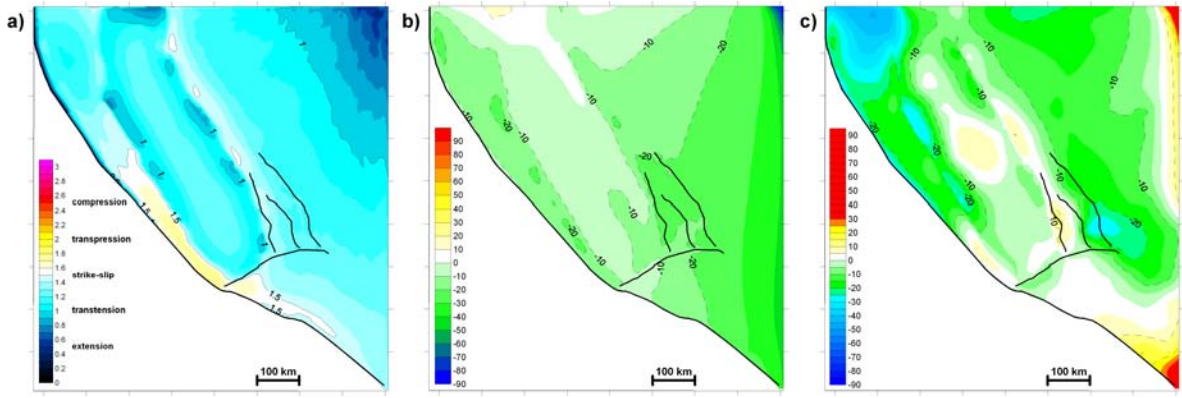
#### 4.7. GPE – tectonic loading interaction

Figure 4.6 shows the difference in Regime-Stress-Ratio (RSR) between the tectonic loading model and the gravity loading only model. The tectonic loading results in fault slip along the SAF north of the Big Bend and thus reduces the fault normal compression ( $<0$ , blue contours) imposed by the high GPE area of the Sierra Nevada and the Basin and Range in the gravitational loading only model. For all other regions the tectonic loading imposes more compression ( $>0$ , yellow contours). The region of highest compression imposed is in the Mojave Block (0.5 - 1). This shows the influence of the bending geometry of the SAF transferring compression into the ECSZ. It should be noted that the stress release along the fault results in less RSR difference (0 to -0.3) than the compression imposed in the far-field ( $>0.5$ ).

#### 4.8. Model without topography

In order to demonstrate the importance of topography induced  $\Delta$ GPE results of an equivalent model are presented in which topographic effects are neglected (Figure 4.7 a, b, c). The observed  $S_H$  orientations resemble those obtained in the gravity and tectonic loading results. The misfit to the WSM orientations is similar and does not show significant differences. However, the tectonic regimes predicted show variations. The Basin and Range (B&R) and the Sierra Nevada (SN) exhibit more transtension, the extensional influence of the topography is minimized. The transpressional corridor along the SAF is much smaller in extent. Figure 4.8 illustrates the difference in RSR of the model with topography and the one without. It can be seen that regions with high GPE (SN, B&R) show less extension ( $<0$ , blue contours) and regions of low GPE (Great Valley) show less compression ( $>0$ , red contours). The reduced compression can not only be seen in the Great Valley but also along the SAF north of the Big Bend. This indicates the strong influence of the high GPE regions of the Sierra Nevada and the Basin and Range on the stress field of the SAF.

The influence of the topography can best be observed in the stress magnitudes at the calibration sites (Figure 4.9 a, b, c). The stress magnitudes predicted for the SAFOOD site are similar to the ones obtained from the model with topography, with only a slight increase of ~5MPa for the horizontal stress components. The magnitudes at the Cajon Pass in the San Gabriel Mountains and for Coso in the Coso Range show much more topographical influence. The high GPE of mountain ranges resulting in extension is removed and both horizontal stress components are significantly increased (10MPa-20MPa).



**Figure 4.7:** a) RSR for gravity plus tectonic loading without topography. Sierra Nevada and Basin and Range exhibit more transtension and the transpressional corridor along the SAF is much smaller in extent. b)  $S_H$  orientation for gravity plus tectonic loading without topography does not show significant changes. c) Difference of  $S_H$  orientation compared to WSM orientations.

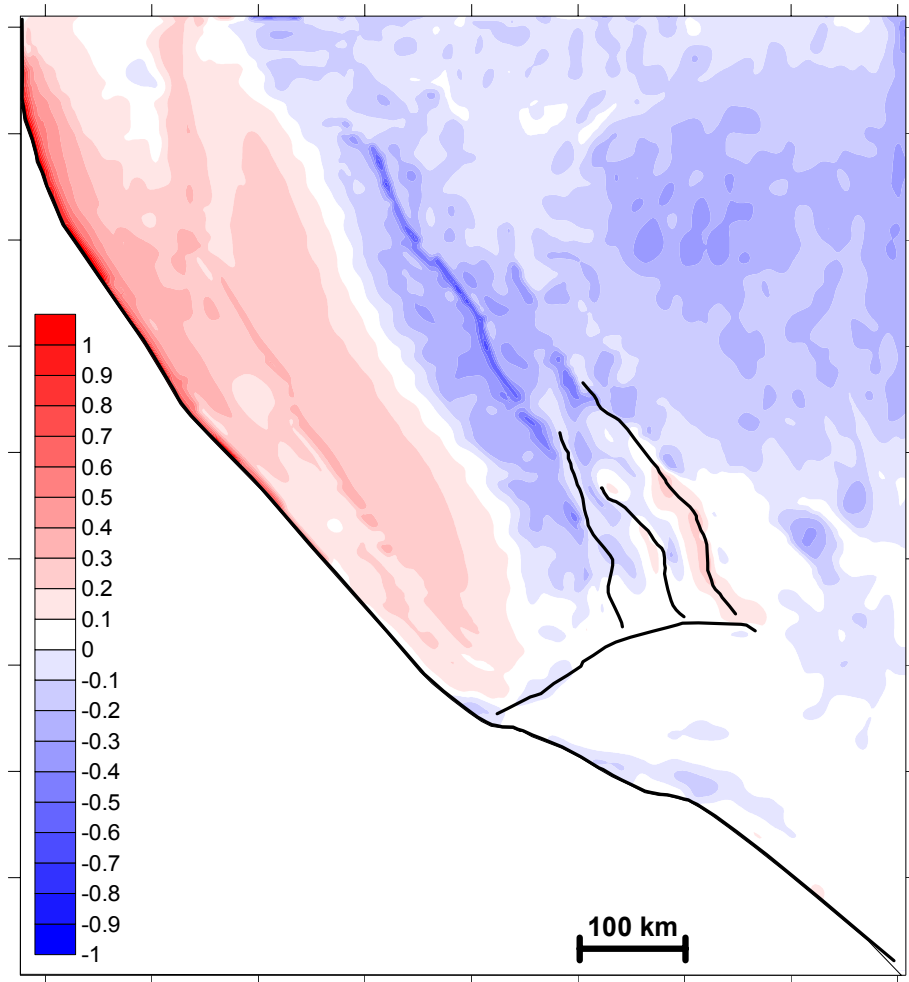


**Figure 4.8:** Difference in RSR between model with topography and without topography. Regions with high GPE (SN, B&R) show less extension (<0, blue contours) and regions of low GPE (Great Valley) show less compression (>0, red contours).

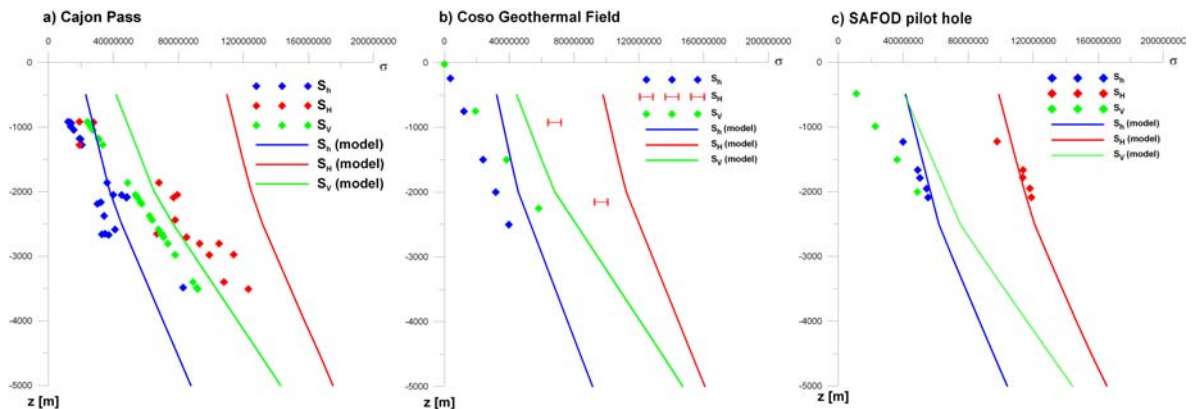


**Figure 4.9:** Stress magnitudes predicted for the SAFOD site seem to be very similar to the ones from the model with topography, with only a slight increase of ~5MPa for the horizontal stress components. The magnitudes at the Cajon Pass in the San Gabriel Mountains and for Coso in the Coso Range show much more topographical influence and both horizontal stress components are significantly increased (10MPa-20MPa).

#### 4.9. Discussion

The lithospheric state of stress is an assembly of many different and complex processes. In the presented approach it is assumed that the crust is in isostatic equilibrium and that gravitational potential energy differences ( $\Delta GPE$ ) imposed by surface topography, plate boundary forces and the first order geometry of the SAF contribute to the 3D crustal state of stress. Neglecting the total crustal thickness is a significant drawback since including Moho surface data would, to some extent, account for buoyancy forces arising from crustal thickness variations with depth. Unfortunately, Moho geometry data for California is constrained to specific areas (e.g. Richards-Dinger, 1997; Zhu and Kanamori, 2000; Fliedner et al., 2000) and different datasets show discrepancies in the order of kilometers. Furthermore, Moho map compilations for California have a very coarse resolution (e.g. 2x2 degree for crust2.0, Bassin et al., 2000). Thus, Moho depth is based on interpolation and is not consistent with the high resolution of the topography dataset used for the FE model. Furthermore, crustal strength profiles (Kohlstedt, et al., 1995) suggest that an upper elastic crust and a lower viscoelastic crust maybe a better approach to model the 3D state of stress. A Moho surface and a viscoelastic lower crust were not implemented since such a model requires a set of basal boundary conditions that can maintain the dominant topography, in particular the Sierra Nevada mountain range which is lacking a thick crustal root (e.g. Jones et al., 2004), in equilibrium. Iteration of this set of boundary conditions has proven to be a very time consuming task that has not been successfully achieved to date. In order to avoid possible errors that result from these uncertainties, the study focuses on the state of stress in the upper crust (0-15km) in California and assumes that  $\Delta GPE$  are solely the effect of surface topography. It is worth emphasizing how well, even with this clearly limiting assumption, the modeling results calibrate to the independent stress orientations and magnitudes.

The dominance of extension and the variability for the orientation of  $S_H$  in the “gravity only” step shows the strong influence of contemporary topography on the in-situ state of stress. The high GPE regions in the north-eastern part of the model cause

significant SAF normal compression. After applying Pacific Plate (PP) motion large parts of the Basin and Range remain extensional, the ECSZ exhibits transtensional tectonics and the compressional corridor along the SAF is reduced to a transpressional tectonic regime. In this process the far-field state of stress in the Sierra Nevada, in the Eastern California Shear Zone (ECSZ) and in the Basin and Range is significantly influenced by PP motion. The plate boundary forces result in distinct  $S_H$  orientations and transfer compressional stresses into the far-field. Figure 4.6 illustrates that stress release along the SAF results in less Regime-Stress-Ratio difference (0 to -0.3) than the compression imposed in the far-field (>0.5). This observation indicates that the tectonic loading of the PP motion has a stronger influence on the far-field state of stress of the SAF. It is suggested that  $\Delta GPE$  related to topography determine the distribution of the tectonic provinces and the PP motion leads to development of the observed tectonic regimes. The results presented are consistent with studies by Flesch et al. (2000, 2007) who conclude that the deviatoric stress field can be explained by equal interaction of  $\Delta GPE$  and boundary forces. Humphreys and Coblenz (2007) also conclude that the tensional nature of WUS stress is a result of high GPE and that orientations of  $S_h$  are associated to plate boundary forces.

An important factor controlling the stress state in California, and especially in the ECSZ, is the geometry of the SAF itself. Du and Aydin, (1996) presented the concept that the Big Bend perturbs and amplifies the surrounding state of stress and induces a zone of shearing northwest of the southern end of the bend. This phenomenon was also found by Li and Liu (2006) who obtained a zone of increased plastic strain energy coinciding with the ECSZ also using 3D FEA. The results presented are consistent with these observations and modeling results. The geometry of the SAF causes a relative increase in  $S_H$  magnitudes along the BB segment and is the main factor for transferring compression and hence strike-slip tectonics through the Mojave Block into the ECSZ.

A model in which topographic influences on  $\Delta GPE$  are omitted yields realistic stress orientations consistent with models including topography. However, stress magnitudes and dependent variables such as tectonic regimes do not match independent observations. In particular, less extensional deformation in regions of high altitude and less compressional deformation in regions of low altitude is generated. Reduced compression along the SAF north of the Big Bend demonstrates the strong influence of the high GPE regions of the Sierra Nevada and the Basin and Range on the stress field of the SAF. The importance of  $\Delta GPE$  becomes most evident when the resulting absolute stress magnitudes are considered. Differences of 5MPa at SAFOD might not seem very much, but it should be noted that an average stress drop of an earthquake is in the range of 1-10MPa (Stein and Wysession, 2003). In this context, differences of 10-20MPa for the Cajon Pass and Coso are significant and might represent a different state of stress.

A comparison to a similar 3D FE modeling approach used by Parsons (2006) points out the importance of how to apply plate boundary forces in 3 dimensions. Parsons investigated the tectonic differential stressing in California and exposed his model to  $\Delta GPE$  and loading conditions simulating the observed surface displacement field. The highest differential stressing rates coincide with regions of greatest seismic energy release in a 200km wide corridor along the plate boundary.  $S_H$  orientation is mostly perpendicular

to the strike of the SAF, but significant misfits to independent data occur in the far field of the SAF. Parsons results indicate that GPS derived surface loads yield appropriate results for short term processes in correlation to recent seismicity, but do not seem to reproduce the 3D state of stress, which has evolved over geologic time scales, correctly.

#### 4.10. Conclusions

Using 3D FEA, the impact of different contributions to the 3D crustal state of stress is investigated. The crustal state of stress is the result of  $\Delta GPE$  due to surface topography, plate boundary forces and the geometry of the San Andreas Fault (SAF). The good match of resulting stress orientations and magnitudes to independent data shows that the absolute state of stress in the upper brittle crust can be reproduced under the present assumptions and loading conditions applied.

Contemporary topography in California is remarkable and resulting  $\Delta GPE$  define regions of different tectonic regimes. These regions are caused by Pacific Plate motion, which is the main driving force for a distinct regional stress field. In particular, plate boundary forces transferred over the SAF have a stronger impact on the regional stress field than near the SAF. Neglecting topography induced  $\Delta GPE$  yields realistic stress orientations but the stress magnitudes and dependent tectonic regimes do not match independent observations. The geometrical impact of the bending segment of the SAF results in increased horizontal stresses in the Mojave Block and transfers compression and hence strike-slip tectonics into the Eastern California Shear Zone to accommodate a part of the relative plate motion.

It should be noted that the results of this study are only valid for the upper brittle crust since buoyancy forces arising from crustal density variations with depth have been neglected. Including a Moho surface is necessary to draw conclusions on the complete lithospheric state of stress. This would account for complete crustal thickness variations and thus might enhance the influence of  $\Delta GPE$  on the complete state of stress.



## 5. The coefficient of friction on the SAF and its impact on stress orientations

### 5.1. Introduction

The San Andreas Fault (SAF) system in California is a prime example of a strike-slip plate boundary bearing the capability to produce strong earthquakes. Hence knowledge of its frictional strength and the accumulation of shear stress on the fault becomes an integral part in estimating the likelihood of earthquake occurrence, triggering and intensity. The frictional strength of the San Andreas Fault is the topic of many studies and the object of a highly controversial debate in recent years. While heat flow measurements (Lachenbruch and Sass, 1992) indicate that the San Andreas is relatively weak, interpretations of stress orientations result in different interpretations and conclusions on the coefficient of friction,  $\mu$ , on the fault.

The SAF has long been inferred as being a weak fault due to a missing heat flow anomaly adjacent to the fault (Brune et al., 1969; Lachenbruch and Sass, 1992). This observation constrains the coefficient of friction,  $\mu$ , to be  $\sim 0.1$ - $0.2$  and the shear stress not to exceed 20-25 MPa. However, shear stress magnitudes of  $\sim 100$  MPa inferred from measurements in deep boreholes (e.g. Brudy et al., 1997; Townend and Zoback, 2000) have shown that faulting in the earth's crust occurs on faults with a high  $\mu$  (0.6-0.85), consistent with laboratory experiments on a variety of rock types (Byerlee, 1978). The discrepancy of the observations of the frictional strength of the SAF and the associated shear stress on the fault is a topic of strong debate. In general, two end-member scenarios have been proposed. (1) The strong fault scenario proposes  $\mu=0.6$ - $0.85$ , consistent with the laboratory experiments, and corresponding shear stress magnitudes larger than 100 MPa (Scholz, 2000). The missing heat flow anomaly is explained by heat loss through water convection in a highly permeable fault zone (Scholz, 2000) or due to dynamical weakening by acoustic fluidization (Melosh, 1996). (2) The weak fault scenario (e.g. Zoback et al., 1987) proposes a coefficient of friction of  $\mu < 0.1$  and shear stresses between 10-20 MPa on the SAF, while all other faults are strong. The low strength of the SAF is explained by high fluid pressure (Rice, 1992).

In order to argue in favor of one of the two scenarios, measurements of the direction of the maximum horizontal stress component,  $S_H$ , at seismogenic depths along the SAF have been used to infer the strength of the SAF. The concept of the two scenarios should predict different orientations of  $S_H$  (Figure 5.1). If the SAF is strong, the fault should be optimally oriented and the angle  $\beta$  between  $S_H$  and the strike of the fault should be low ( $\sim 30^\circ$ ). A weak SAF with low shear stress requires relatively high angles ( $\sim 80^\circ$ ) of  $S_H$ . A large number of stress measurements, mostly derived from earthquake focal mechanisms, have been made along the SAF and have been used to infer the strength of the SAF (e.g., Hardebeck and Hauksson, 1999; Provost and Houston, 2003; Townend and Zoback, 2004). In this process some studies observe high angles, others observe low angles. Hardebeck and Michael (2004) reviewed and reanalyzed the stress orientations from different studies and concluded that the disagreement resulted from different interpretation. They found that  $S_H$  orientations generally have an intermediate angle ( $40^\circ$ - $60^\circ$ ) and propose that the strength of the SAF is similar to the strength of other faults in all

the scenarios considered. Thus, the SAF maybe a strong fault which is not optimally oriented, or in a low-stress model the stress orientations indicate the loading state and earthquake history of the fault and not its strength.

Of particular interest becomes if the observed stress orientations are a result of the coefficient of friction on the SAF and thus if the resulting stress orientations can be used to infer the strength of the SAF. Therefore, a sensitivity analysis on the coefficient of friction is conducted mimicking the end-member scenarios of a strong and weak fault to study the impact of  $\mu$  on the orientation of  $S_H$ .

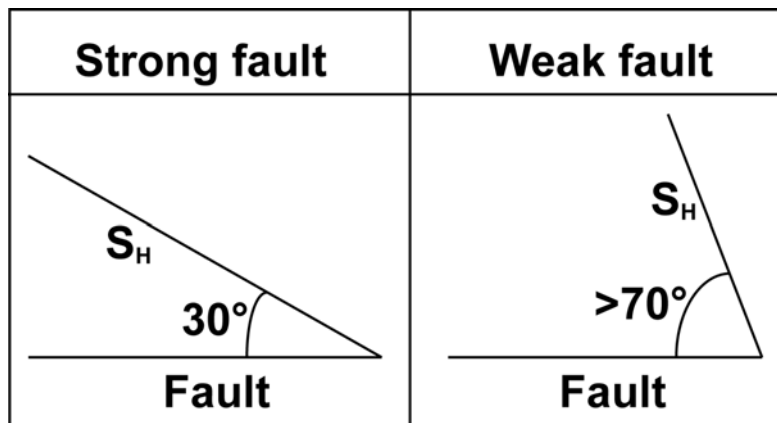


**Figure 5.1: Context of friction angle to the orientation of  $S_H$ . A strong fault requires low angles and a weak fault high angles.**

## 5.2. Other modeling studies

The strength of the SAF has been the focus of several numerical modeling studies. Chery et al. (2001, 2004) modeled the SAF as a weak zone ( $\mu=0.1$ ) in a strong crust ( $\mu=0.6-0.8$ ). They used a variety of rheologies (based on an initial temperature field) for the crust, mantle and the fault zone to study the stress orientations both near the fault zone and in the far field. Their results showed that both a strong fault ( $\mu=0.6$ ) and a weak fault ( $\mu=0.1$ ) reproduced high angles of  $S_H$  of  $\sim 80^\circ$  to the fault in the far-field. However, only a weak fault rheology generated  $S_H$  reorientations to  $63^\circ$  near the fault zone, as observed in the SAFOD pilot hole (Hickman and Zoback, 2004). The results of this study are generally appropriate for the near fault field of the creeping section of the SAF, but not for other segments of the fault as mentioned by Chery et al. (2001). Furthermore, the model setup and the loading conditions do not represent the complex interaction of plate boundary forces and gravitational potential energy differences ( $\Delta GPE$ ) due to crustal thickness variations and the geometrical heterogeneity of the fault.

Fitzens and Miller (2004) modeled the SAF in the Big Bend region as a frictional surface ( $\mu=0.6$ ) in an elastic half-space. The modeled fault contains high pressure fluid cells to simulate interseismic and coseismic fluid pressure changes and thus variable fault strength with time. They obtained stress magnitudes consistent with a strong crust and intermediate angles of  $S_H$  ( $\sim 45^\circ$  at the northern segment and  $\sim 55^\circ$  at the southern segment) within 20km of the fault. They also obtained local stress rotations of  $\pm 10^\circ$  due to differences in cumulative slip on the fault. This may be an indication for the heterogeneity

of  $S_H$  orientations along the SAF. However, due to the discrepancy of stress magnitudes and orientations Fitzens and Miller do not draw a conclusion on the strength of the fault.

### 5.3. Model

The modeling study and the sensitivity analysis on the coefficient of friction presented in this chapter is based on the geometry, the boundary conditions and the model calibration presented in chapter 4.

#### 5.3.1. Model limitations

**Rheology:** As described in chapter 4 it is assumed that the stress state is dependent on ΔGPE and tectonic boundary forces with both basal shear and buoyancy forces neglected. Therefore, only linear elastic material properties are used, although heat flow measurements in the WUS and crustal strength profiles (e.g. Kohlstedt et al., 1995) suggest that an approach with an upper elastic crust and a lower visco-elastic crust maybe more realistic. However, since  $S_H$  orientations from focal mechanisms occurring in seismogenic depths of 0-10km are used to infer the strength of the SAF, the linear elastic approach is considered useful.

**Fault modeling:** The SAF is included as a contact surface separated by split nodes, which allow in-plane fault motion but no separation. The fault has zero width and obeys Coulomb friction, with varying  $\mu$ . It is important to note that the assumption of an infinitesimally thin fault neglects the actual rheology of the SAF as a fault zone, containing a plastic fault core. This fault core could be exposed to high fluid pressures weakening the fault and result in rotations of  $S_H$  to smaller angles in the fault zone (Rice, 1992). However, the cataclasite fault core of the SAF is observed to be 10-100m (Chester et al., 1993). Since the modeling approach is based on a regional tectonic scale, a plastic fault core is much smaller than the average element size in the FE model and thus effects on that scale are not considered.

### 5.4. Impact of $\mu$ on $S_H$ orientations

The results presented in chapter 4 showed that a good match to observed tectonic regimes, stress magnitudes and  $S_H$  orientations could be achieved with the current modeling assumptions. After calibrating the resulting state of stress, the influence of the coefficient of friction on the  $S_H$  orientations is investigated by conducting a sensitivity analysis ( $\mu=0.1, 0.2, 0.4, 0.6, 0.8, 1.0$ ) mimicking different scenarios for the strength of the SAF. The effect of  $\mu$  both for the far-field of the SAF and for orientations on the fault surface is investigated.

**Far-field:** Figure 5.2 illustrates the difference in  $S_H$  orientation of the two end-member scenarios, i.e. the  $S_H$  orientation results for  $\mu=0.1$  have been subtracted from the  $\mu=1.0$  results. It is obvious that  $S_H$  does not change more than  $\pm 1^\circ$  farther away than ~75km from the SAF. Closer to the fault (10-50km) the influence of  $\mu$  slightly increases and the difference between the weak and the strong fault scenario is  $-1^\circ$  to  $-3^\circ$ , indicated by the green contours in Figure 5.2. Interestingly, a higher  $\mu$  generates higher angles to the fault.

However, this influence is very small and other effects than  $\mu$  may be the cause. For example, this effect mostly occurs in regions where the rheological contrast between the Sierra Nevada micro-plate and the coastal areas is present. Closer than 10km to the fault a change in sign occurs and the difference between the weak and the strong fault scenario is  $0^\circ$ - $5^\circ$ , such that a lower  $\mu$  now results in higher angles to the fault. This effect seems to be very localized near the fault and thus the  $S_H$  results directly on the fault need to be considered.

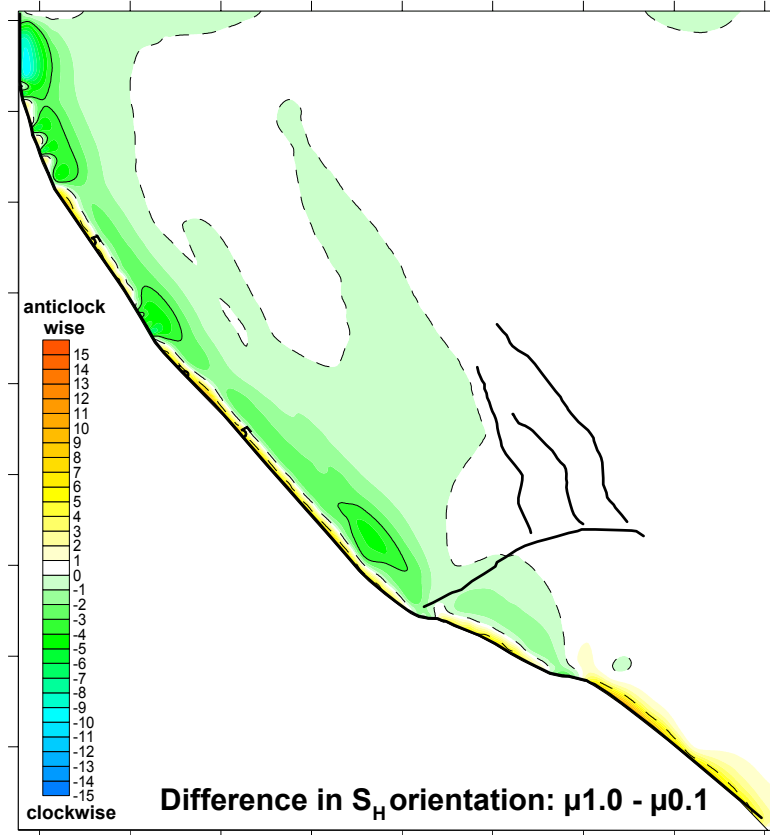


**Figure 5.2:**  $S_H$  orientation difference from the two end-member scenarios shows no significant influence of  $\mu$  in the far-field ( $<5^\circ$ ). Absolute orientations of  $S_H$  are given in Figure 4.4b.

**Near-field:** Figure 5.3 shows the angle  $\beta$  of  $S_H$  to the strike of the fault. The contours are plotted on the fault surface going from the northwest (left) to the southeast (right). In general, the SAF can be divided into two parts. North of the Big Bend  $S_H$  is at lower angles than south of the Big Bend. This trend can be observed for all  $\mu$  tested.

For the weak fault scenario ( $\mu=0.1$ )  $\beta$  is  $50^\circ$ - $65^\circ$  north of the Big Bend, and south of the Big Bend higher angles ( $70^\circ$ - $85^\circ$ ) occur. In the case of a strong fault ( $\mu=1.0$ )  $\beta$  is  $55^\circ$ - $60^\circ$  north of the Big Bend, and south of it  $\beta$  is also higher ( $70^\circ$ - $85^\circ$ ). The data also shows that local variations north of the Big Bend of angles up to  $74^\circ$  (for  $\mu=0.1$ ) and down to  $35^\circ$  (for all  $\mu$ ) can be observed. The most striking feature of Figure 5.3 is that when  $\mu$  is increased,  $\beta$  does not change significantly. Slightly higher  $\beta$  for lower  $\mu$  can be observed near the surface. To clarify the impact of  $\mu$  the difference of the two end-member scenarios has been calculated (bottom map of Figure 5.3). As for the far-field, the difference of the angle is only minor. In depths of 0-15km variations of  $0^\circ$  to  $-10^\circ$  (Figure 5.3 bottom map, yellow and red contours) occur. Only locally does  $S_H$  differ by more than  $-5^\circ$ . The

maximum difference is  $-14^\circ$ . Also, changes of  $0^\circ$ - $3^\circ$  occur (green contours), which are associated with the bends in the SAF. The fault geometry has more impact on  $\beta$  in these locations than  $\mu$ .

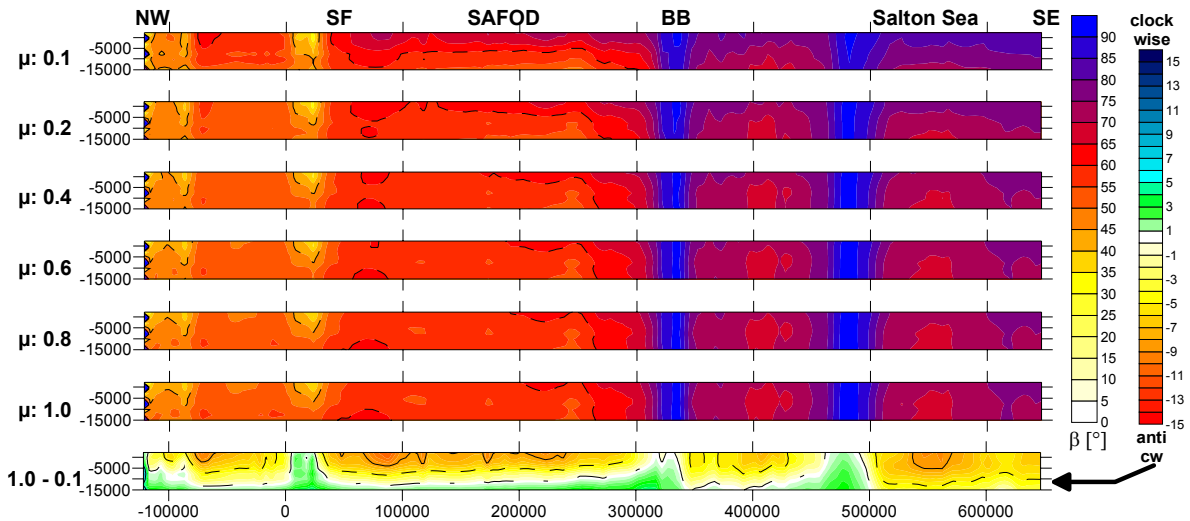


**Figure 5.3:** Angle  $\beta$  of  $S_h$  to the strike of the SAF for the various  $\mu$ . For all  $\mu$   $S_h$  is at lower angles north of the Big Bend than south of the Big Bend. When  $\mu$  is increased,  $\beta$  does not change significantly, indicating that  $S_h$  orientations do not strongly depend on the coefficient of friction and thus not on the strength of the fault.

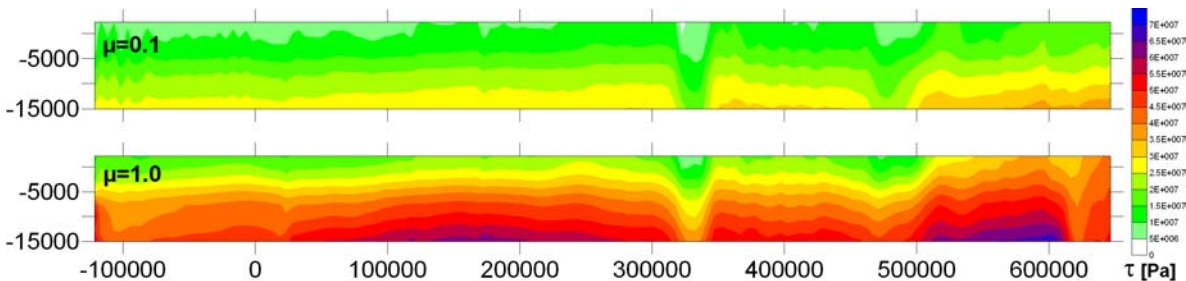


**Figure 5.4:** Shear stress magnitudes of 10-30MPa for the weak fault scenario and 25-60MPa for the strong fault scenario are predicted. The lower magnitudes at  $\sim 320,000$  and  $\sim 480,000$  are associated to geometrical effects of the bending geometry of the SAF.

## 5.5. Shear stress on the SAF

Corresponding to the coefficient of friction and thus to the strength of the fault the magnitude of shear stress on the fault surface plays an important role. The end-member scenarios generate shear stresses of 10-30MPa for  $\mu=0.1$  and 25-60MPa for  $\mu=1.0$  (Figure 5.4). For both scenarios the southern part of the SAF (south of x-coordinate 100,000, i.e. between SF and Parkfield) shear stress magnitudes are slightly higher (1-5MPa). Only at the bending sections of the Big Bend segment the shear stress is slightly ( $\sim 5$ MPa) lower than at adjacent sections.

The magnitudes for a weak SAF scenario of 10-30MPa correspond very well to previously suggested magnitudes of 10-25MPa (Brune et al., 1969, Lachenbruch and Sass, 1992) and 10-20MPa (e.g. Zoback et al., 1987). However, for the strong fault scenario the

modeled shear stress magnitudes of 25-60MPa are much lower than predicted magnitudes in the order of ~100MPa (Scholz, 2000). A possible explanation is that the modeled shear stresses represent average values. The SAF is included as a smooth vertical fault. Inhomogeneities on the fault surface would result in higher shear stresses locally.

## 5.6. Discussion and conclusions

The most important question to be addressed in this analysis is, 'does the SAF have a strong, weak or intermediate strength'? The modeled orientations for  $S_H$  show a good correlation to data from the World-Stress-Map (Figure 4.4b) and predict intermediate angles of  $\beta$  north of the Big Bend and high angles south of it. This is consistent with results from Flesch et al. (2000).  $S_H$  orientation trajectories of their results can be seen in Townend and Zoback (2004). Following the classic arguments, results for  $\beta$  north of the Big Bend are in favor of an intermediate strength and south of the Big Bend for a weak fault. However, the results show that the variations are reproduced for all tested  $\mu$ , ranging from a weak fault to a strong fault.

Increasing  $\mu$  from a weak scenario ( $\mu=0.1$ ) to a strong scenario ( $\mu=1.0$ ) results in minor changes in  $\beta$ . Differences of  $0^\circ$  to  $-10^\circ$  in a depth range of 0-15km with local variations of  $(-10^\circ$  to  $-14^\circ)$  are obtained. The observation of higher  $\beta$  for a weak fault is consistent with the predicted orientations for the fault models. However, the differences for the two end-member cases are in the order of  $10^\circ$  and not as predicted by variations between the models reported in the literature, which are in the order of  $40^\circ$ - $50^\circ$ .

An important point to emphasize is the fault modeling approach in a regional plate-scale tectonic setting. The results presented in this study are based on the assumption that the SAF is modeled as a frictional surface with zero width.  $S_H$  rotations in a plastic, weak fault core with fluid pressures present are not considered. Yet, the fault core of the SAF is inferred to be  $\sim$ 100m wide (Chester et al., 1993) and recent investigations from the SAFOD drilling site report of a fault width of approx. 20m (Hickman et al., 2005). Furthermore, stress measurements at the Cajon Pass 4km away from the fault indicate a strong crust (Zoback and Healy, 1992). These observations support the assumption that the SAF can be considered as a discrete surface in this plate scale modeling approach. Thus, the results presented here are considered reasonable approximations for determining both the far-field ( $>10$ km) and near-field ( $>1$ km) state of stress on the SAF. This set of model results suggests that  $S_H$  orientations are only marginally influenced by the faults' coefficient of friction. This leads to the assertion that  $S_H$  orientation data is not an adequate approach for inferring the strength of the SAF. It is suggested that this insensitivity to the coefficient of friction is the main reason for the different interpretations and conclusions drawn from the same dataset. It is considered more likely that the orientation of  $S_H$  indicates the loading state and earthquake history, as suggested by Hardebeck and Michael (2004). As long as direct in-situ stress measurements from the SAFOD drilling site do not yield an absolute stress tensor from which the shear stress on the fault surface can be derived and then compared to modeled magnitudes, the strength of the SAF will remain a matter of ongoing discussion.

## 6. State of stress in the Eastern California Shear Zone (ECSZ)

### 6.1. Submodeling study at the ECSZ scale

The San Andreas Fault (SAF) scale modeling study (chapter 4) yielded a state of stress that is consistent with the observed tectonic regimes in the ECSZ and the Coso Range and that provides good matches to independent data for  $S_h$  orientation and magnitudes. The resulting displacements are now used as loading conditions for a model of the ECSZ.

### 6.2. Introduction

The Eastern California Shear Zone (ECSZ) (Figure 6.1) in the south-western US has been the focus of many studies (Dokka and Travis, 1990; Savage et al., 1990; Dixon et al., 1995; Bennett et al., 1997; Gan et al., 2000; Miller et al., 2001; Bennett et al., 2003, and many others.). These studies conclude that the ECSZ accommodates up to ~25% of the relative motion between the North American plate and the Pacific plate. North of the Garlock Fault ~12mm/yr of right lateral shear is partitioned on three major right lateral fault zones: the Death Valley-Furnace Creek, the Hunter Mountain-Panamint Valley and Owens Valley structures (e.g. Bennett et al., 1997). To the west the ECSZ is bounded by the NW moving (~13mm/yr) rigid block of the Sierra Nevada (SN; Dixon et al., 2000) and the eastern margin is the Basin and Range physiographic province.

Kinematic studies of deformation within the ECSZ conclude that the observed surface displacements are partitioned between a large dextral shear component of the plate boundary deformation and a smaller extensional component of the Basin & Range tectonics (Dixon et al., 1995; Bennett et al., 2003). Consequently, transtension is widely expressed in the ECSZ (e.g. Unruh et al., 2002; Unruh et al., 2003; Wesnousky, 2005). As indicated by Du and Aydin (1996), Li and Liu (2006) and also shown in chapter 4 the geometry of the San Andreas Fault plays an important role in transferring increased horizontal stresses and thus strike-slip influence into the ECSZ.

In addition to the kinematics of the ECSZ, various authors have investigated parts of the regional stress field. Zoback (1989) reports of  $S_h$  orientations of N80°W in the Owens Valley and N60°W for the northern Basin and Range. Townend and Zoback (2004) present a consistent pattern of  $S_h$  orientation of NNE-SSW in the southern Sierra Nevada region, which is also consistent with the majority of orientations in southern California. This data set, which was mainly derived from earthquake focal mechanisms, is in good agreement with gravitational potential energy modeling results from Flesch et al. (2000). Various stress and strain measurements/investigations have been undertaken in the Coso Range north of the Garlock Fault. Roquemore (1980), Feng and Lees (1998) and Unruh et al. (2002) conclude that the Coso Range is under NNE-SSW compression and WNW-ESE extension. In summary, the stress and strain data support hypothesis of a current dextral transtensional stress regime in the ECSZ.

However, information about relative or absolute stress magnitudes is sparse, and if existing may only be valid for a local area. Furthermore, discrepancies exist as to whether the state of stress in the ECSZ represents a singular distinct regional state of stress with slip

partitioning explaining different deformation styles (Wesnousky and Jones, 1994; Le et al., 2007), or if the state of stress is spatially or temporarily varying (Zoback and Zoback, 1989; Zoback, 1989; Bellier and Zoback, 1995; Monastero et al., 2002). This chapter presents the results of a 3D finite element study of the regional state of stress in the ECSZ and especially in the Owens Valley-Airport Lake Fault Zone and suggests a consistent state of stress in the ECSZ regionally varied by topography.

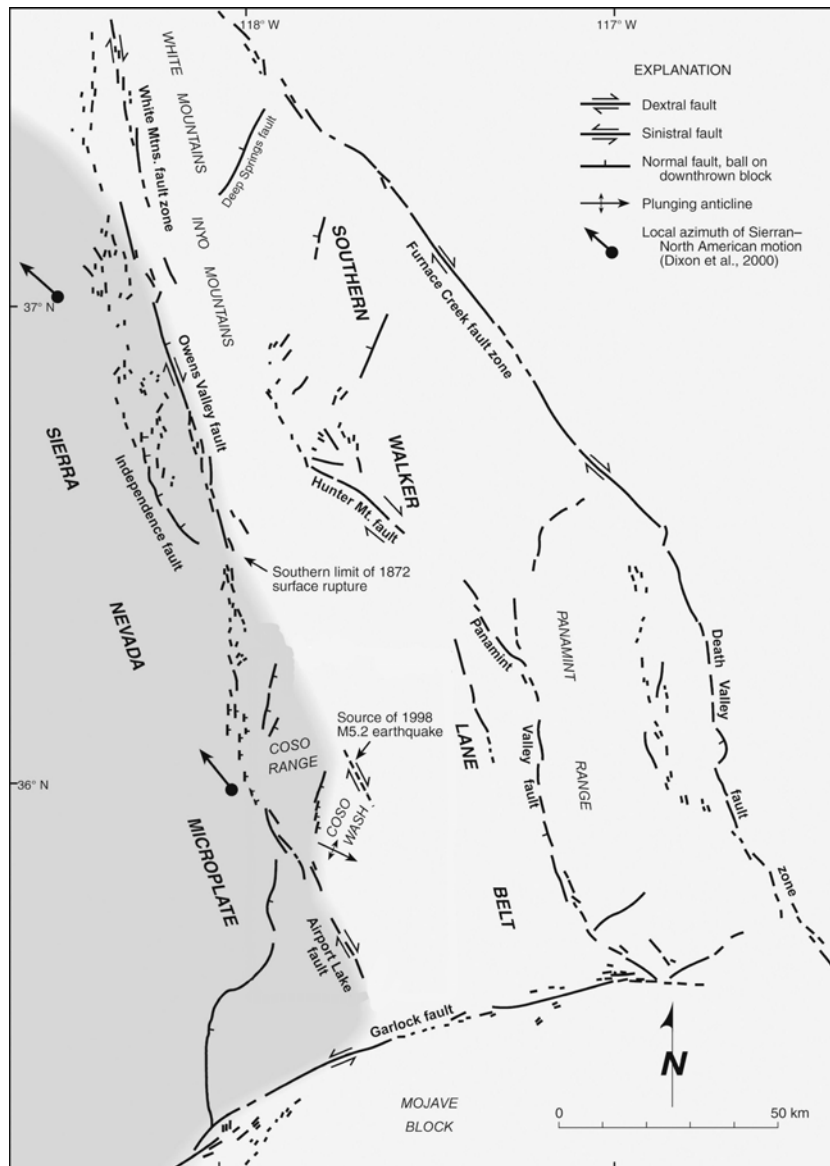


Figure 6.1: Major active faults of the Walker Lane Belt in the ECSZ (after Jennings, 1994).

### 6.2.1. Tectonic setting of the Owens Valley Fault

The Owens Valley Fault – Airport Lake Fault Zone (OVF-ALFZ) is located within the ECSZ north of the Garlock Fault and directly east of the Sierra Nevada frontal scarp. Current kinematic studies of this region suggest that the OVF-ALFZ represents a transtensional transition zone where active strike slip and normal faults accommodate north-westward translation of the rigid Sierra Nevada micro-plate (Unruh et al., 2003). At

the southern end of the Sierra Nevada the Little Lake Fault and the Airport Lake fault Zone mark the tectonic boundary between the SN and the ECSZ. Further north the Owens Valley Fault (OVF) is the most active structure bounding the SN to the east. The fault accommodates right lateral shear (locally oblique slip) and had a major rupture in 1872 with a magnitude 7.5 earthquake (Beanland and Clark, 1994).

Analysis of GPS velocity fields (McClusky et al., 2001) indicates that half of the shear in the ECSZ is accommodated on the ALFZ and the OVF. The current tectonic interpretation is that the shear on the ALFZ is transferred via a right releasing step-over northwards across the Coso Range to become the OVF. Unruh et al. (2002) conclude that shear transfer on this entire fault system forms a dilational step-over that drives crustal extension in the Coso Range. 3D analogue and preliminary 2D FE models suggested that the ALFZ and OVF structures are linked at depth to form a bend rather than a step (Dooley and McClay, 2003). Unruh et al. (2002) also suggest that the bulk transtension of the Coso Range arises because the region is attached to the NW moving Sierra Nevada and is being pulled from underneath.

### 6.3. ECSZ model setup

**Geometry:** The 3D geometry comprises the topographic surfaces of Eastern California and includes the upper 45km of the crust and the mantle intersected by the major active faults (Figure 6.2: Owens Valley Fault-Airport Lake Fault, Panamint Valley Fault, Hunter Mountain Fault, Death Valley Fault, White Mountain Fault, Blackwater Fault, Lockhart Fault, Garlock Fault; after Jennings, 1994). The Sierra Nevada is included as a separate block with different rheological parameters. The model is divided into 3 layers (upper crust, lower crust, mantle). A Moho surface separating the crust from the mantle is based on data from Zhu and Kanamori (2000) and Fliedner et al. (2000). Incorporated faults have the following dips (Table 6.1):

Fault	Dip & dip direction	Reference
Owens Valley Fault	85° NNE	Wesnousky and Jones (1994)
Airport Lake Fault Zone	80° NNE	USGS fault report
Bend across the Coso Range	80°-85°	interpretation
Death Valley Fault	90°	USGS fault report
Panamint Valley Fault	80°-90° N15°E	Jennings (1994)
Hunter Mountain Fault	80°-90°	USGS fault report
White Mountain Fault	80°	USGS fault report
Garlock Fault	90°	USGS fault report

Table 6.1: Dips for included faults

**Rheology:** As for the SAF scale only linear elastic rheologies are used (Table 6.3). The Young's modulus can be derived from seismic p- and s-wave velocities (standard textbooks, e.g. Jaeger and Cook, 2007):

$$E = \rho v_s^2 \frac{3v_p^2 - 4v_s^2}{v_p^2 - v_s^2} \quad (6-1)$$

The following datasets have been used to derive the Young's modulus for the various model units (Table 6.2).

<b>Unit</b>	<b><math>\rho</math></b>	<b>vp</b>	<b>vs</b>	<b>Reference</b>
Mojave upper crust	2700	6000		Fuis et al., 2001
Mojave lower crust	2850	6350		Fuis et al., 2001
Mojave mantle	3300	8000		Fuis et al., 2001
Southern California	2700	5900	3410	Zhu and Kanamori (2000)
Basin and Range upper crust	2700	6000		Fliedner et al., 2000
Basin and Range lower crust		6400		Fliedner et al., 2000

**Table 6.2: Seismic velocities used to derive the Young's modulus for the various model units.**

<b>Layer/Unit</b>	<b>Density [kg/m<sup>3</sup>]</b>	<b>E [GPa]</b>	<b>v</b>
Upper Crust	2700	70	0.25
Lower Crust	2850	85	0.275
Sierra Nevada	2690	75	0.275
SN_LowerCrust	2850	85	0.3
Mantle	3300	175	0.325

**Table 6.3: Rheological parameters for the various model units**

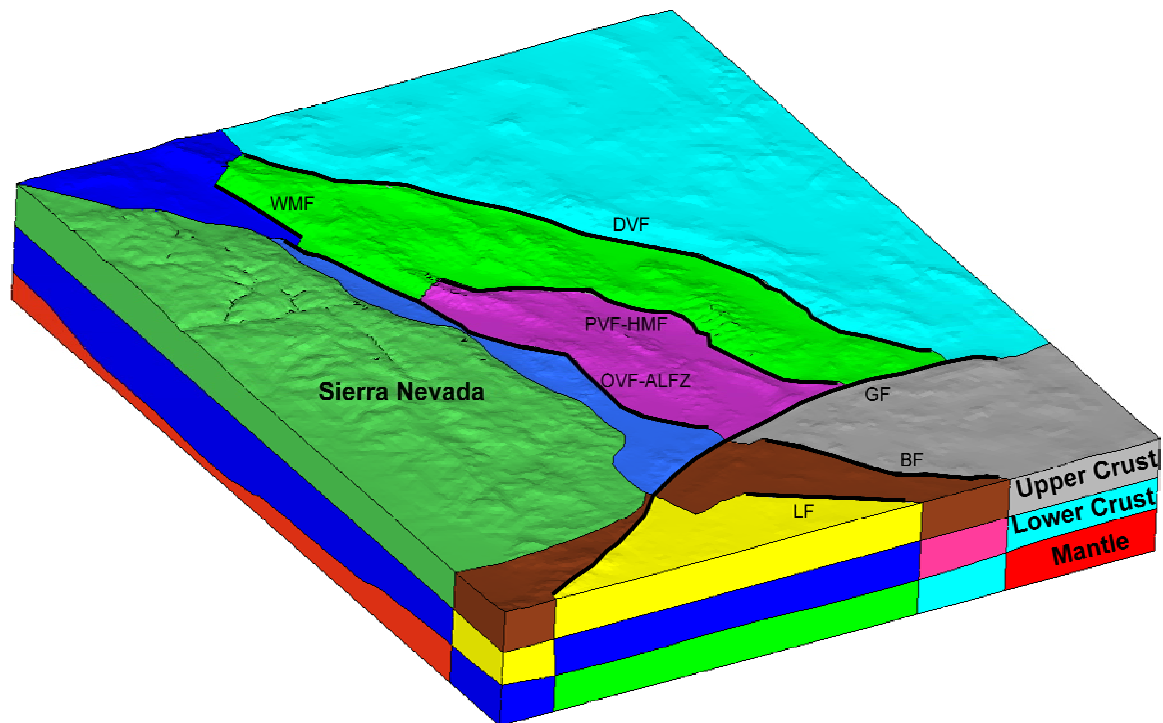


**Figure 6.2:** The ECSZ scale model comprises layers of the upper, lower crust and the mantle. The Sierra Nevada is included as a separate block. Major faults of the ECSZ after Jennings (1994). OVF-ALFZ: Owens Valley Fault-Airport Lake Fault Zone, PVF: Panamint Valley Fault, HMF: Hunter Mountain Fault, DVF: Death Valley Fault, WMF: White Mountain Fault, BF: Blackwater Fault, LF: Lockhart Fault, GF: Garlock Fault.

### 6.3. Sheorey calibration

The initial state of stress for the ECSZ is calibrated against the Sheorey curve for  $E=70\text{GPa}$  (Figure 6.3). Two different virtual wells are used to calibrate the resulting  $k$ -ratios. One site is situated in the Mojave block (blue line in Figure 6.3) and the other one in the Coso Range (red line in Figure 6.3). Both curves match the Sheorey curve below 2 km depth. The better fit of the Coso Range curve is caused by the finer discretization in this area.

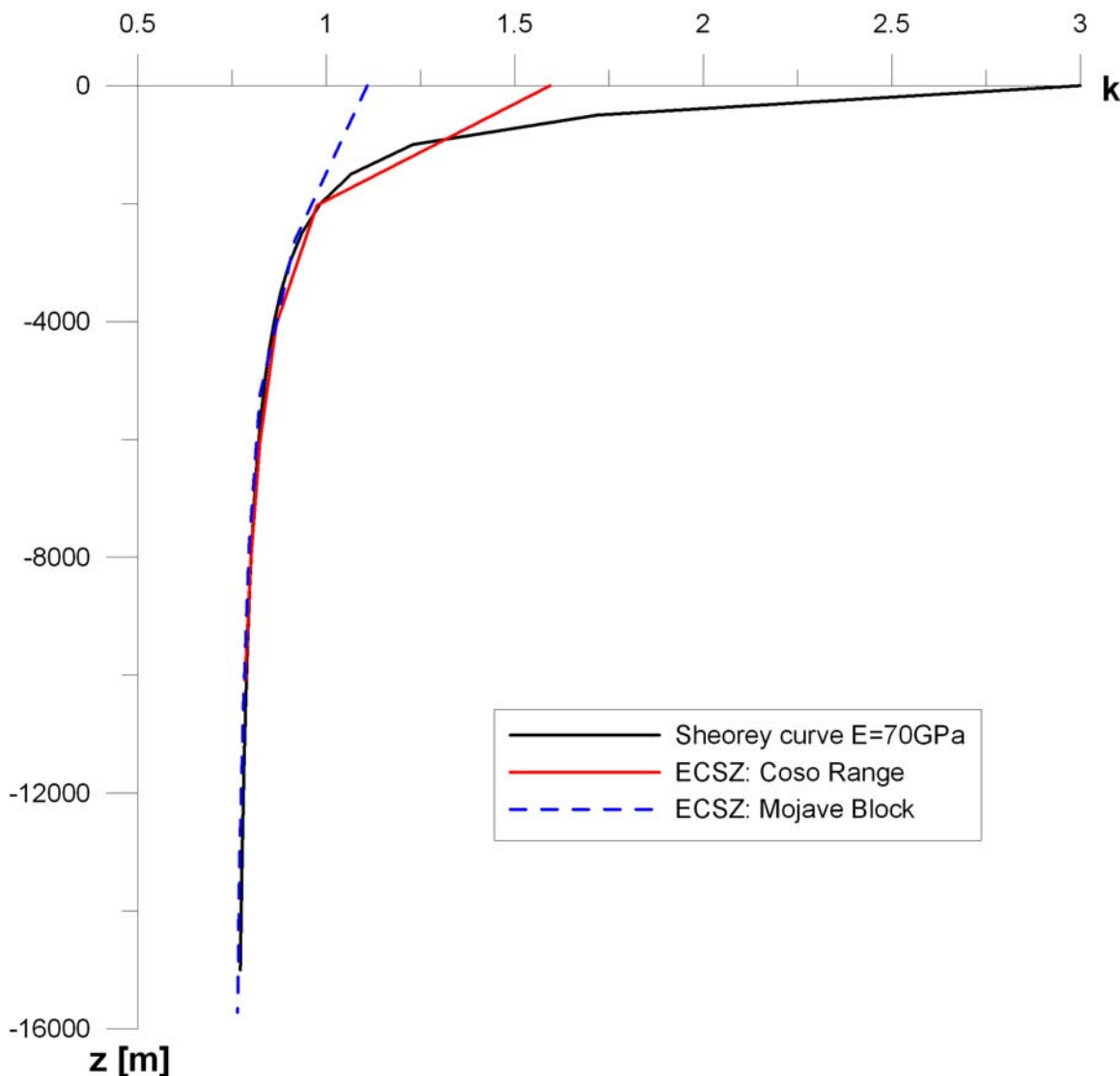


**Figure 6.3:** Sheorey calibration for the initial state of stress. 2 “wells” are used to match the Sheorey curve of  $E=70\text{GPa}$ . The Coso Range curve provides a better fit since the mesh resolution is finer than in the Mojave Block.

## 6.4. Loading procedure

It should be noted that the SAF scale analysis cannot reproduce the observed displacement field, since the rather homogeneous model does not account for the strain partitioning observed in the WUS. To alleviate this limitation, an additional step is added to the modeling procedure:

- a) initial gravitational state of stress (Sheorey based)
- b) submodel analysis from SAF scale to obtain realistic state of stress, i.e. tectonic stressing (see chapter 1.3.1.)
- c) superimpose GPS displacement boundary conditions to account for contemporary tectonics and obtain realistic displacement field

The last step is necessary since realistic displacements are necessary for the Coso Range scale submodel analysis.

### 6.4.1. Tectonic stressing

In this modeling step the model is solved as a submodel of the SAF scale model. Instead of running the model to mimic the same 20ka time period as the SAF scale model, the ECSZ scale model is only run over 10ka. This time span provides a better fit to the state of stress than a 20ka sub-model (see stress magnitudes in Figure 6.6 for both periods), presumably reflecting stress relief processes within the ECSZ that are not observable at the larger scale.

**Regime-Stress-Ratio (RSR; see chapter 2.7):** RSR is shown for depths of  $z=-1000\text{m}$ ,  $z=-3000\text{m}$  and  $z=-5000\text{m}$  (Figure 6.4). For  $z=-1000\text{m}$  the model predicts strike-slip regimes in the Mojave Block, in the Indian Wells Valley, in the Owens Valley, in the Panamint Valley and in the Death Valley. Close to the faults even slight transpressional regimes are obtained. The Coso Range exhibits transtension. For  $z=-3000\text{m}$  the strike-slip influence is reduced and most parts of the ECSZ exhibit transtensional stress regimes. However, close to the faults (OVF, PVF and DVF) the strike-slip influence is still modeled. At  $z=-5000\text{m}$  the topographic influence on the state of stress becomes more dominant, i.e. higher  $\Delta GPE$ , and extension prevails, especially in the Sierra Nevada and the Basin and Range. The fault sets of the ECSZ are still located in transtensional corridors.

**$S_H$  orientation:** The submodel analysis yields a distinct stress field for the model region.  $S_H$  is oriented  $N10^\circ E - N25^\circ W$  (Figure 6.5a). The difference plot to the WSM (Figure 6.5b) shows a good match. The majority of the model region has differences of less than  $20^\circ$ . The Coso Range in particular has a very good correlation with  $S_H$ , differing by less than  $10^\circ$  to the available data.

**Stress magnitudes (Figure 6.6):** The stress magnitudes are analyzed for different model periods. The resulting magnitudes for  $S_h$  and  $S_H$  are used to infer the most appropriate loading magnitude.  $S_H$  magnitudes for the 20ka period yield slightly overestimated magnitudes for  $S_H$  but the magnitude for  $S_h$  is too low and becomes negative above  $z=-1000\text{m}$ . For 10ka modeled  $S_H$  magnitudes fit the upper stress estimate and modeled  $S_h$  magnitudes significantly increase and fit the measurements. The vertical stress component yields a nearly perfect fit. Only close to surface the modeled magnitudes are slightly overestimated since low density sediments near surface are not included in the model.

**Displacements:** The displacement field resulting from the submodel analysis does not yield the observed surface displacements. The magnitudes are too high since the SAF scale global model does not account for the large strain partitioning observed in the Western US.

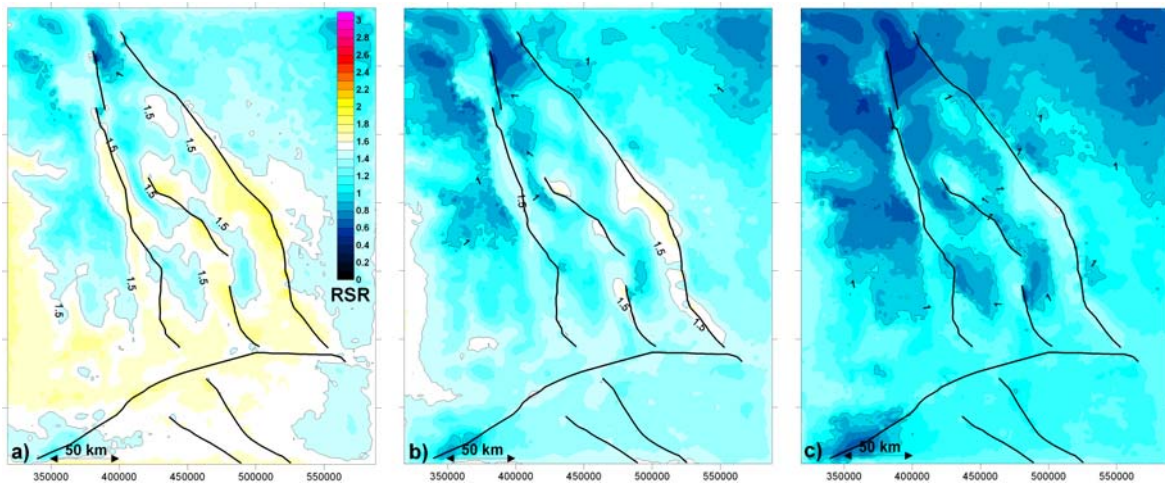


**Figure 6.4:** a) Regime-Stress-Ratio (RSR) at  $z=-1000\text{m}$ . Strike-slip and transtension in most parts of the ECSZ. The northern model part is dominated by extension due to higher  $\Delta\text{GPE}$ . b) RSR at  $z=-3000\text{m}$ . Transtension in the southern ECSZ and extension north of the Coso Range. c) RSR at  $z=-5000\text{m}$ .

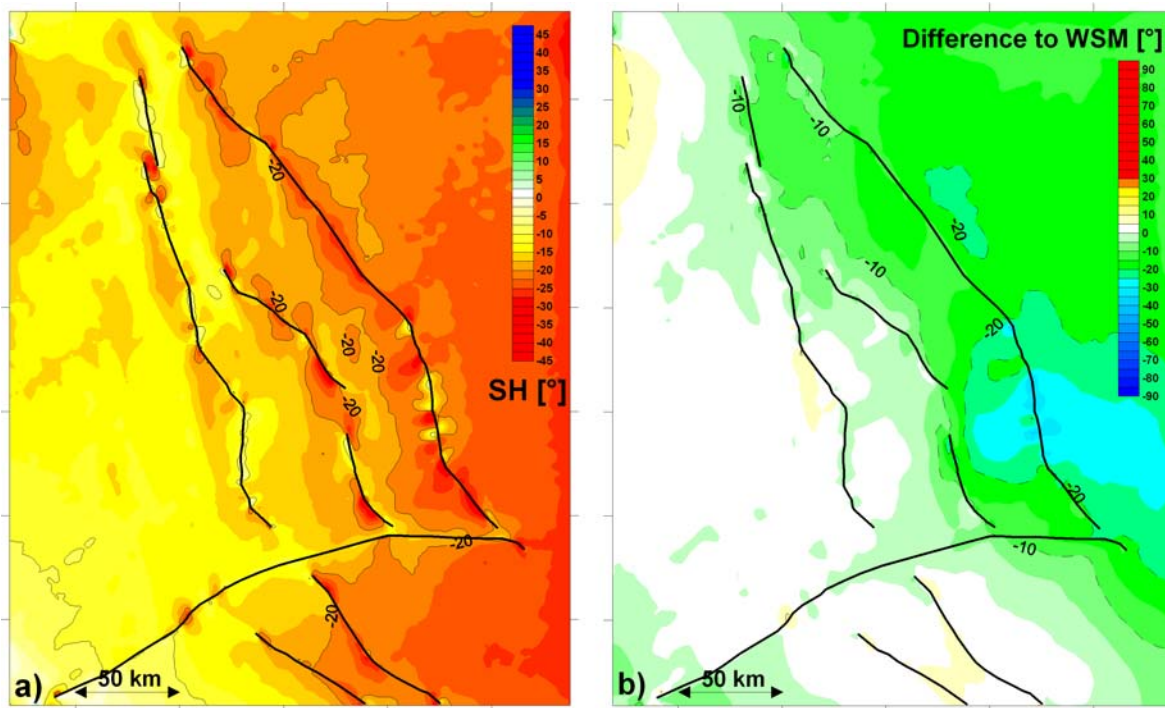


**Figure 6.5:** a)  $S_H$  orientation. A distinct stress field is observed in the ECSZ.  $S_H$  is oriented N10°E–N25°E. b) Difference to WSM data shows a good fit (i.e.  $<20^\circ$ ) for majority of the model. Especially in the Coso Range a good fit (i.e.  $<10^\circ$ ) has been achieved.

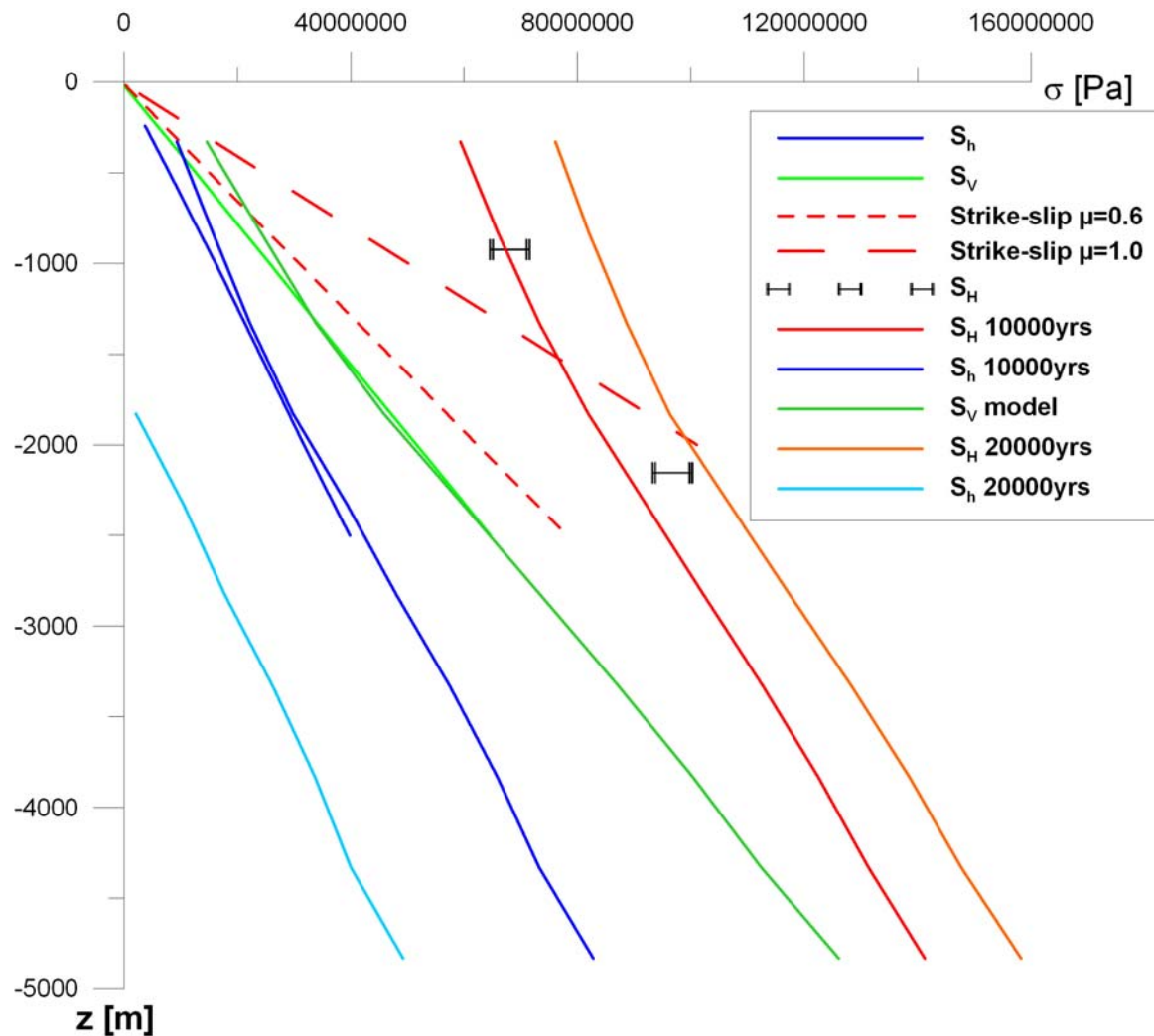


**Figure 6.6: Stress magnitudes at Coso for 10000yrs and 20000yrs of elastic displacement. Reference measurements and estimates after Sheridan and Hickman (2004).**

#### 6.4.2. “Displacement” analysis

A displacement field obtained by extrapolating 1000 years of contemporary GPS is now imposed on the resulting state of stress. The Sierra Nevada (SN) block has a constant N47°W directed velocity of 12.4 mm/yr (Bennett et al., 2003), the eastern model boundary is moved 3mm/yr E-W mimicking Basin and Range (B&R) tectonics, the northern model boundary is an interpolation between SN and B&R velocities, and on the southern model boundary velocities are increased from SN velocity in the SW to the average north velocity component of stations J700, BSY and BARS (10.11mm/yr) until the Blackwater Fault and then decreased to match B&R velocities in the SE model corner.

The aim of this procedure is to obtain a result set that is consistent both for stress and displacements. The results of this model can then be used for a submodel analysis at the Coso Range scale. The GPS displacement applied are equivalent to 1000yrs of elastic displacement. This causes only minor changes to the modeled state of stress and yields displacements that can then be used for the submodel analysis of the Coso Range scale model.

**Regime-Stress-Ratio (RSR):** The RSR distribution (Figure 6.7) after the GPS displacement application yields slightly more transtension but still represents a very similar state of stress for the ECSZ for all considered depths.

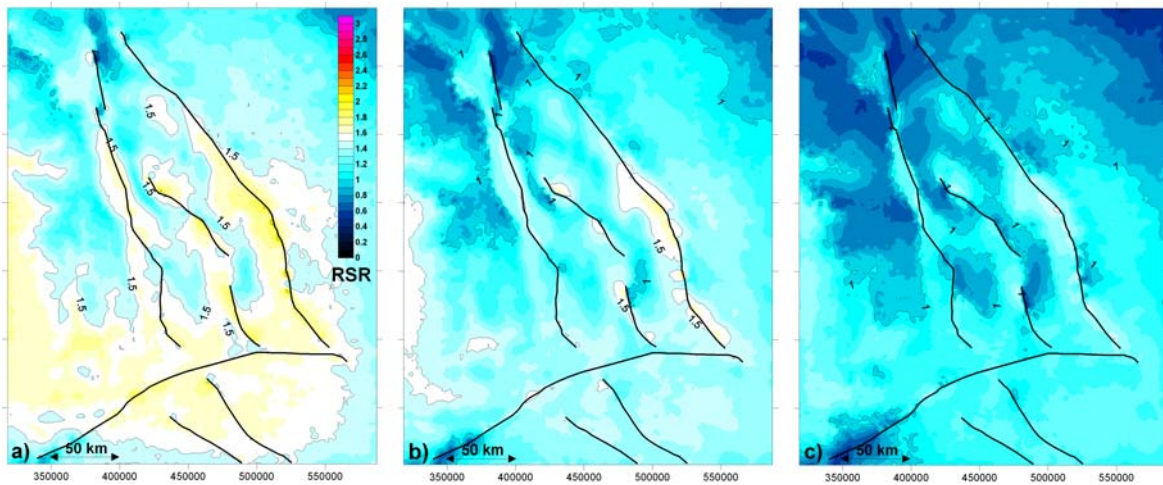


Figure 6.7: Results for the displacement analysis. Regime-Stress-Ratio (RSR) is slightly decreased since more extension is imposed to the model (a=-1000m, b=-3000m, c=-5000m).

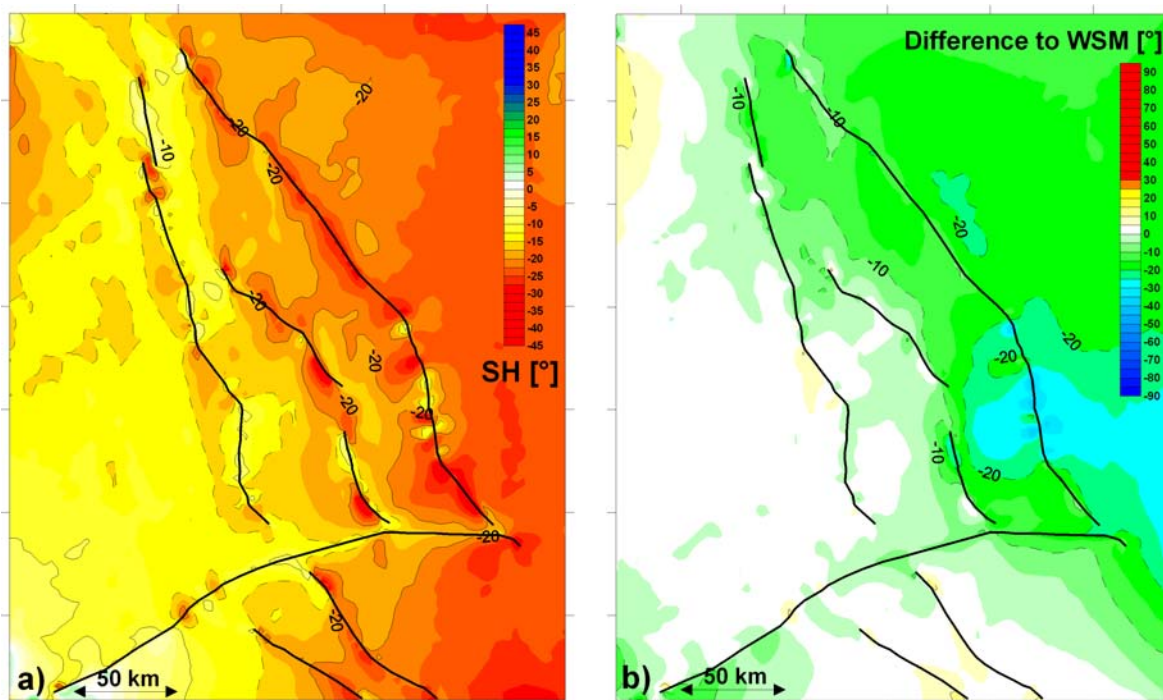
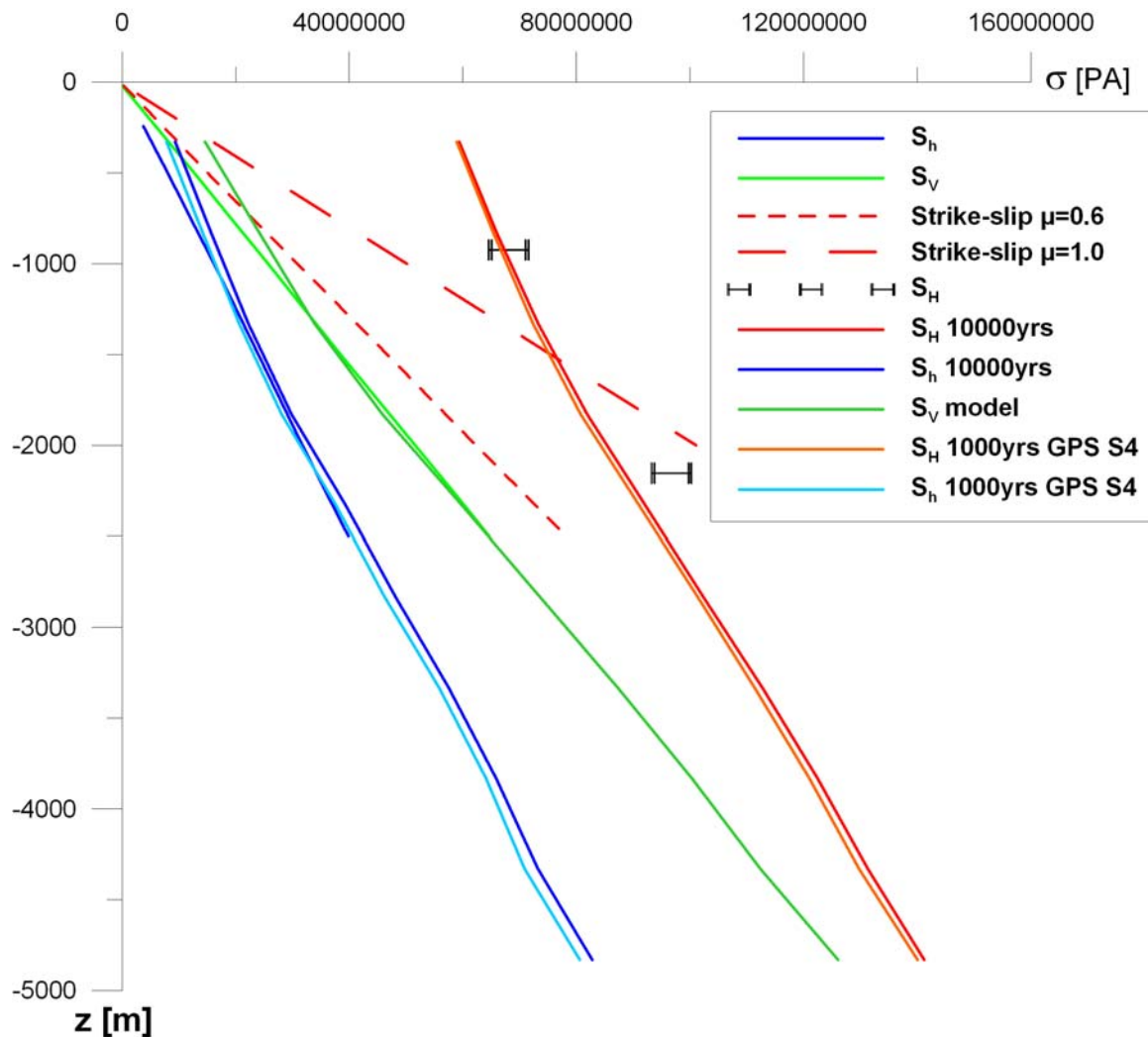


Figure 6.8: a)  $S_H$  orientation. A similar distinct stress field is observed in the ECSZ.  $S_H$  is oriented N10°E-N25°E. b) Difference to WSM data shows a good fit (i.e.  $<20^\circ$ ) for majority of the model. Especially in the Coso Range a good fit (i.e.  $<10^\circ$ ) has been achieved.



**Figure 6.9:** Stress magnitudes for the GPS displacement analysis are slightly smaller than for the tectonic stressing procedure. The stress regime is not affected.

**$S_H$  orientation:** The GPS displacements change the stress orientations only slightly (Figure 6.8c, d).

**Stress magnitudes:** The stress magnitudes derived for the displacement analysis are slightly lower, i.e. more tensile, due to the additional tensile loads (Figure 6.9), but still match the independent data.

**Displacements:** The GPS derived loads and the resulting surface displacement field are compared to current/recent GPS measurements in the ECSZ (Figure 6.10). From the USGS webpage (<http://quake.usgs.gov/research/deformation/gps/auto/>) the Yucca and Fort Irwin profiles are used. Data from Bennett et al. (2003) gives additional calibration points in the northern ECSZ and along the Yucca profile. In general, a good fit to the independent surface displacement was achieved, both for the modeled magnitudes and orientations.

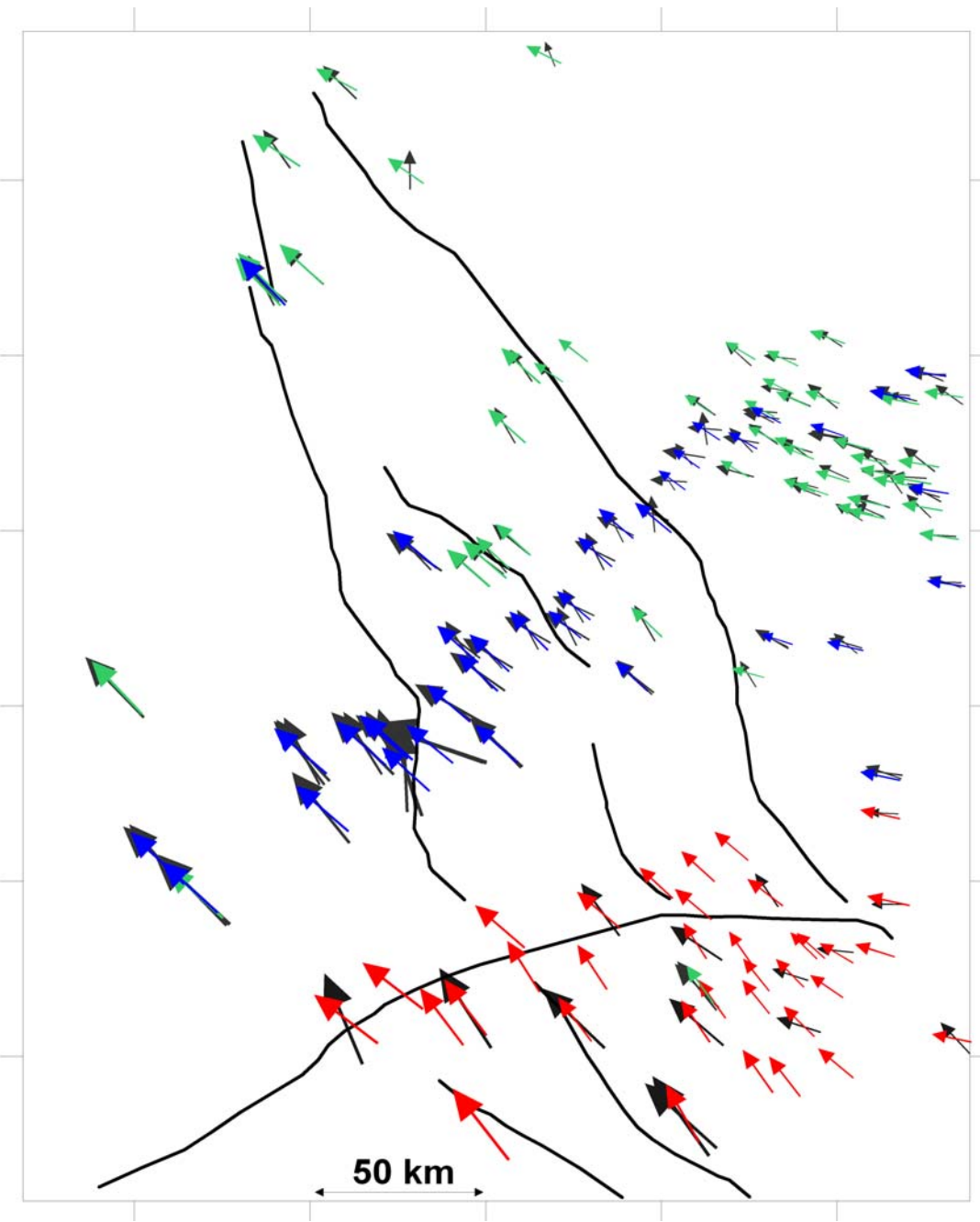


**Figure 6.10:** Modeled (red, blue and green arrows) and observed (black arrows) surface displacement field. The modeled displacement orientations and magnitudes yield a good match to independent data and thus provide a good base for the submodeling analysis of the Coso Range scale models.

#### 6.4.3. GPS based tectonic loading

One might argue that the state of stress in the ECSZ can also be modeled by applying boundary conditions only based on contemporary GPS velocities. The velocities of the 1000yrs displacement step are therefore extrapolated to 10000yrs and 20000yrs to mimic a tectonic loading only based on the interpolated GPS displacement field. The results for the Regime-Stress-Ratio at  $z=-3000\text{m}$  (Figure 6.11) and the resulting stress magnitudes (Figure 6.12a) clearly show that the boundary conditions do not generate sufficient horizontal stresses to generate strike-slip or transtensional tectonic regimes,

respectively. For 10000yrs  $S_h$  magnitudes can be matched, however  $S_H$  is too low. Increasing the loading magnitude to 20000yrs results in slightly higher  $S_H$  but also yields unrealistic, negative  $S_h$  magnitudes. The resulting  $S_H$  orientations (Figure 6.12b,c) have distinct orientations of N5°E – N30°E but the differences to WSM orientations are greater than those of the submodeling procedure.

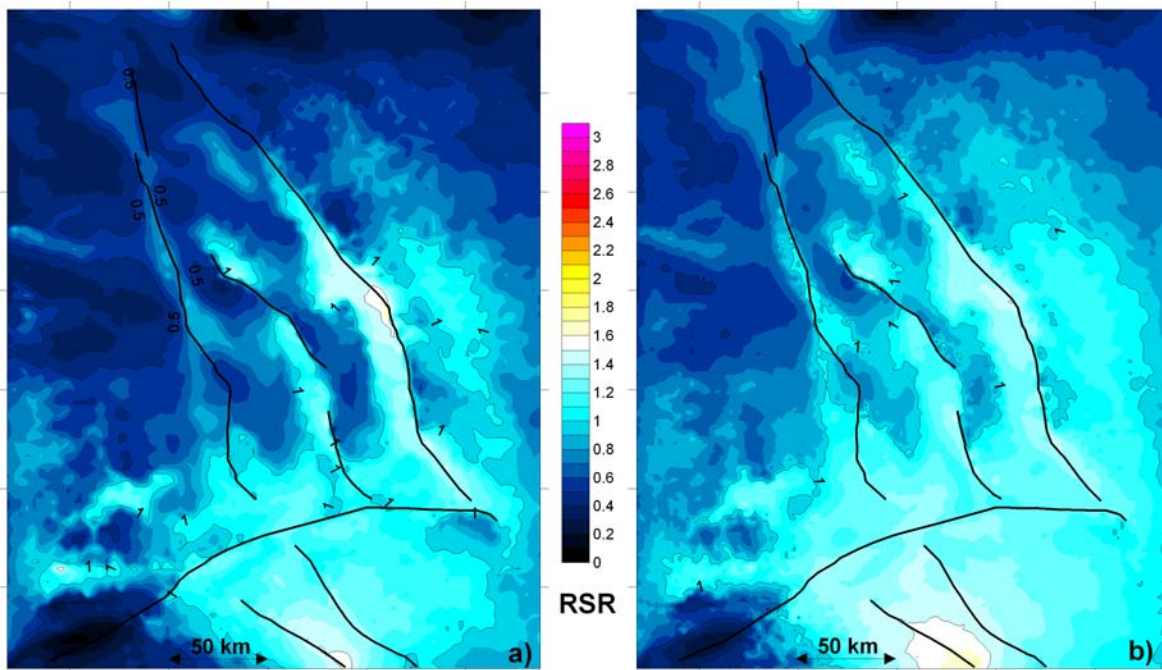


**Figure 6.11:** Regime-Stress-Ratio (RSR) at  $z=$ -3000m for 10000yrs (a) and 20000yrs (b) of GPS velocity based tectonic loading. Compared to the submodeling analysis from the SAF scale model the transtensional influence is insufficient. The models are dominated by extension.

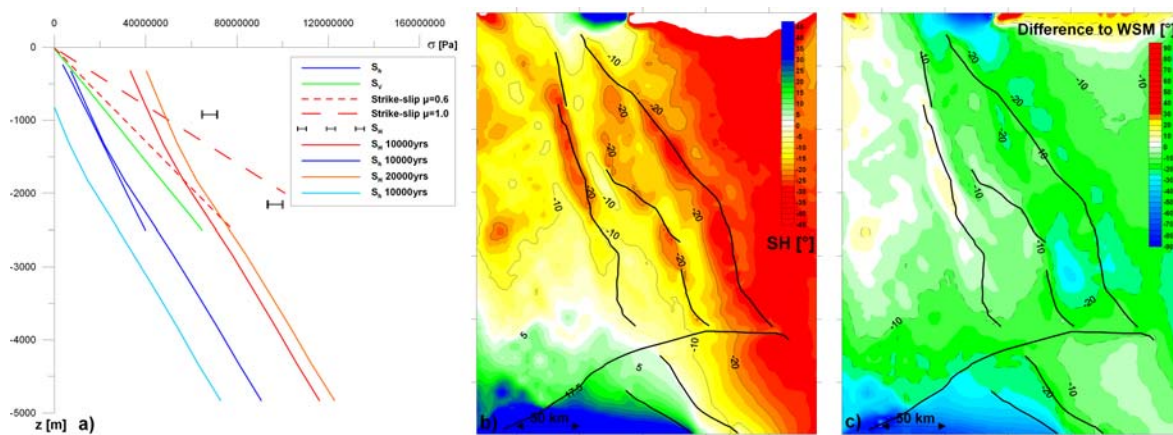


**Figure 6.12:** a) Stress magnitudes for GPS based 10000yrs and 20000yrs loading.  $S_H$  is significantly underestimated for both time periods and for 20000yrs  $S_h$  is negative close to surface. b)  $S_H$  orientations also yield distinct stress field of N5°E – N30°E but difference to WSM orientations (c) are greater.

## 6.5. Fracture Potential

The state of stress and the resulting Fracture Potential distribution based on different post-processing rheologies (defined by cohesion and coefficient of internal friction) is compared to the spatial distribution of seismicity in the ECSZ (Figure 6.13a,b). A correlation of seismic clusters and elevated shear Fracture Potential (sFP) can be observed in the Mojave Block at the southern tip of the Blackwater Fault, in the Coso Range, in the southern Death Valley, and south of the Owens Valley.

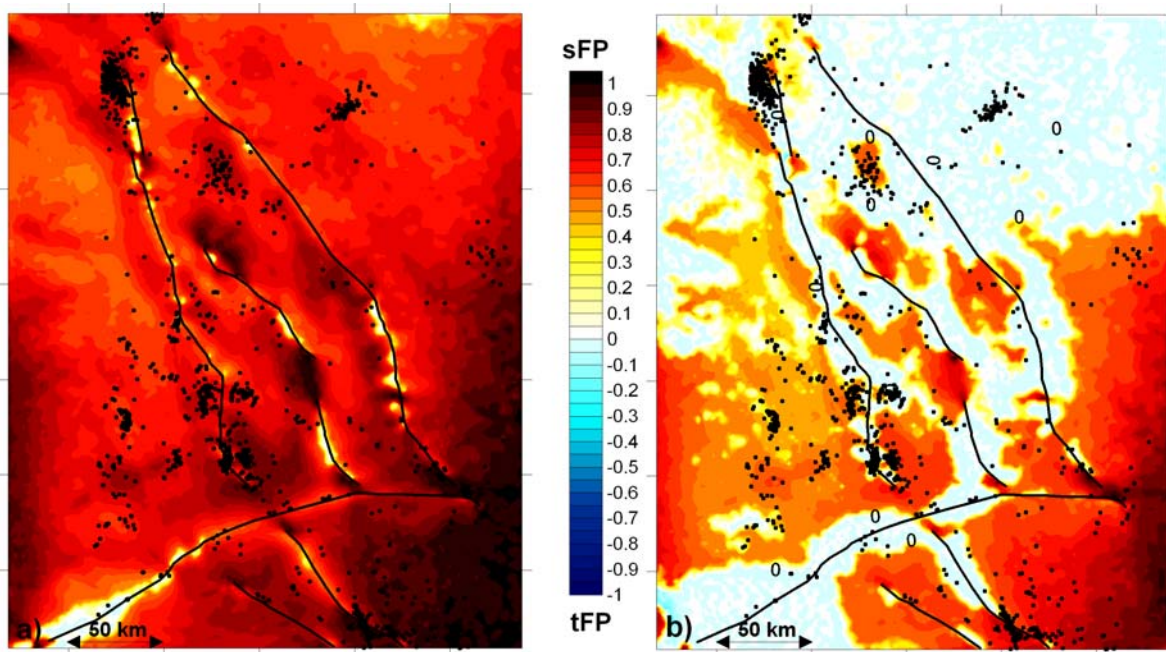


**Figure 6.13:** Fracture Potential for two post-processing rheologies. A) Post-processing rheology 1 defined by a cohesion ( $c_0$ ) of 30MPa and a coefficient of internal friction ( $\mu$ ) of 0.6 representing intact granitic rock. b) Post-processing rheology 2 ( $c_0=20$ Mpa and  $\mu=0.4$  representing weaker rock). Both FP contours are compared to the spatial distribution of ECSZ seismicity. Correlation of seismic clusters and FP exist in the Coso Range, the Mojave Block, in the southern Death Valley and south of the Owens Valley.

## 6.6. State of stress in the ECSZ

In combination, the Regime-Stress-Ratio (RSR) and the stress ratio  $R = \sigma_2 - \sigma_3 / \sigma_1 - \sigma_3$  (Figure 6.14) can be used to analyze the state of stress. While the RSR distribution shows extensional (B&R, SN), transtensional (in most regions of the ECSZ) and strike-slip (DVF, PVF, OVF) regimes, the stress ratio shows a more uniform state of stress, i.e.  $0.8 > R > 0.5$ . End-member cases ( $R > 0.8$ ) correlate to topographic maxima. For  $z=-3000\text{m}$  the Owens Valley Fault ( $R=0.5$ ) is located in a corridor of pure strike-slip and the Independence Fault ( $R=0.7$ ) exhibits transtension.

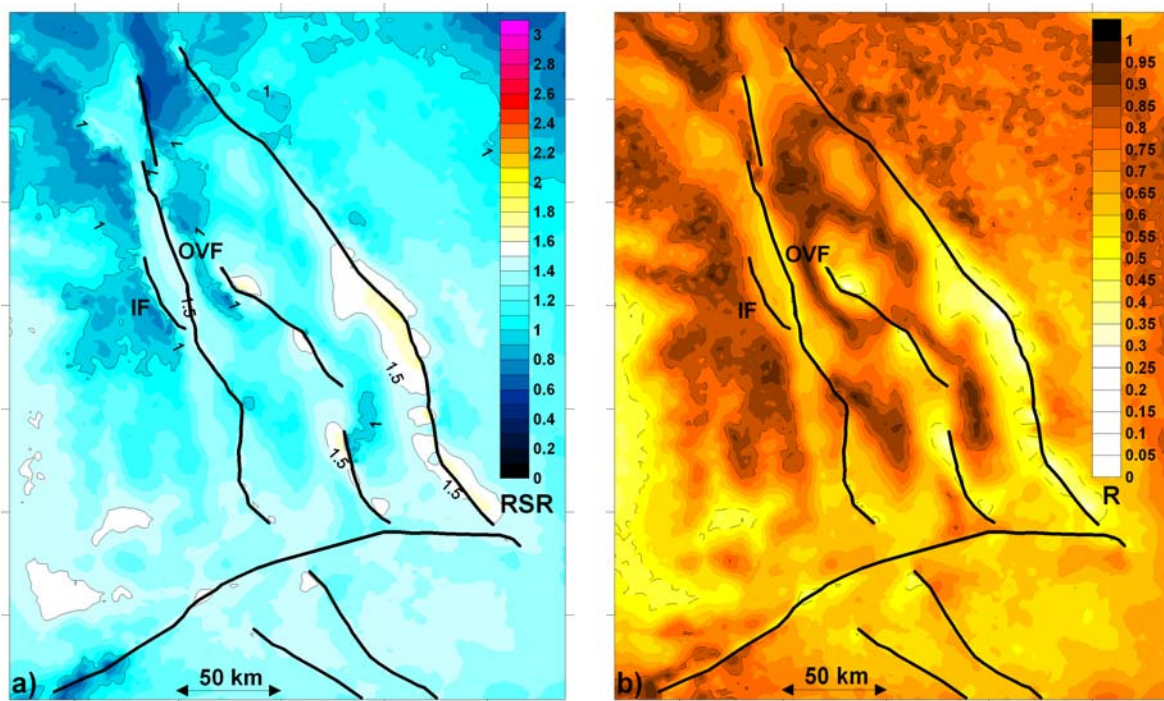


**Figure 6.14:** a) Regime-Stress-Ratio (RSR) at  $z=-3000\text{m}$  showing extension in the B&R and in the SN, transtension in most regions of the ECSZ and strike-slip regimes along the major faults including the OVF. The Independence Fault (IF) is situated in a transition zone between transtension and extension. b) Stress ratio R for the ECSZ showing a consistent state of stress ( $0.8 > R > 0.5$ ) for most parts of the ECSZ. R maxima coincide with topographic highs.

### 6.6.1. State of stress of the Owens Valley Fault and the Coso Range

The Owens Valley Fault (OVF) plays a major role in accommodating dextral shear in the ECSZ and is characterized by strike-slip and oblique slip deformation. Studies by Beanland and Clark (1987) indicate an average ratio of 6:1 of lateral to vertical slip. The modeled tectonic regimes (RSR, Figure 6.15) on the surface of the fault yield strike-slip tectonics near surface ( $z>-3000\text{m}$ ) and transtensional regimes until depths of  $z=-6000\text{m}$ . This indicates that strike-slip deformation on the OVF is possible until depths of  $\sim 8\text{km}$ . The RSR distribution on the fault also shows that strike-slip deformation is predicted throughout the Coso Range. The regional RSR distribution (for  $z=-3000\text{m}$ ; Figure 6.16) for the Coso Range illustrates that the ALFZ-OVF is situated along regions of pure strike-slip tectonics (white contours) while the bulk of the Coso Range exhibits more transtension.

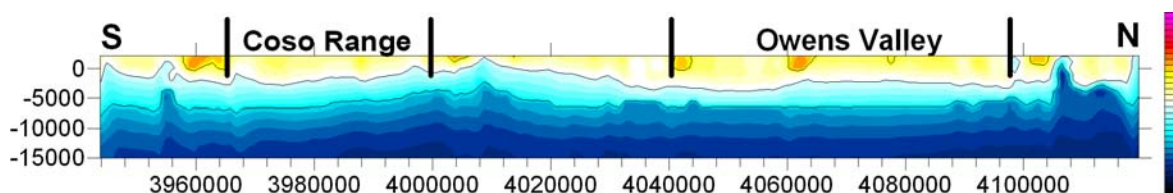


**Figure 6.15:** Regime-Stress-Ratio (RSR) distribution on the OVF from the S in the ALFZ to the northern Owens Valley. Near surface the fault exhibits strike-slip tectonics on the entire length. Strike-slip deformation is possible to depths of  $z=-6000\text{m}$ .

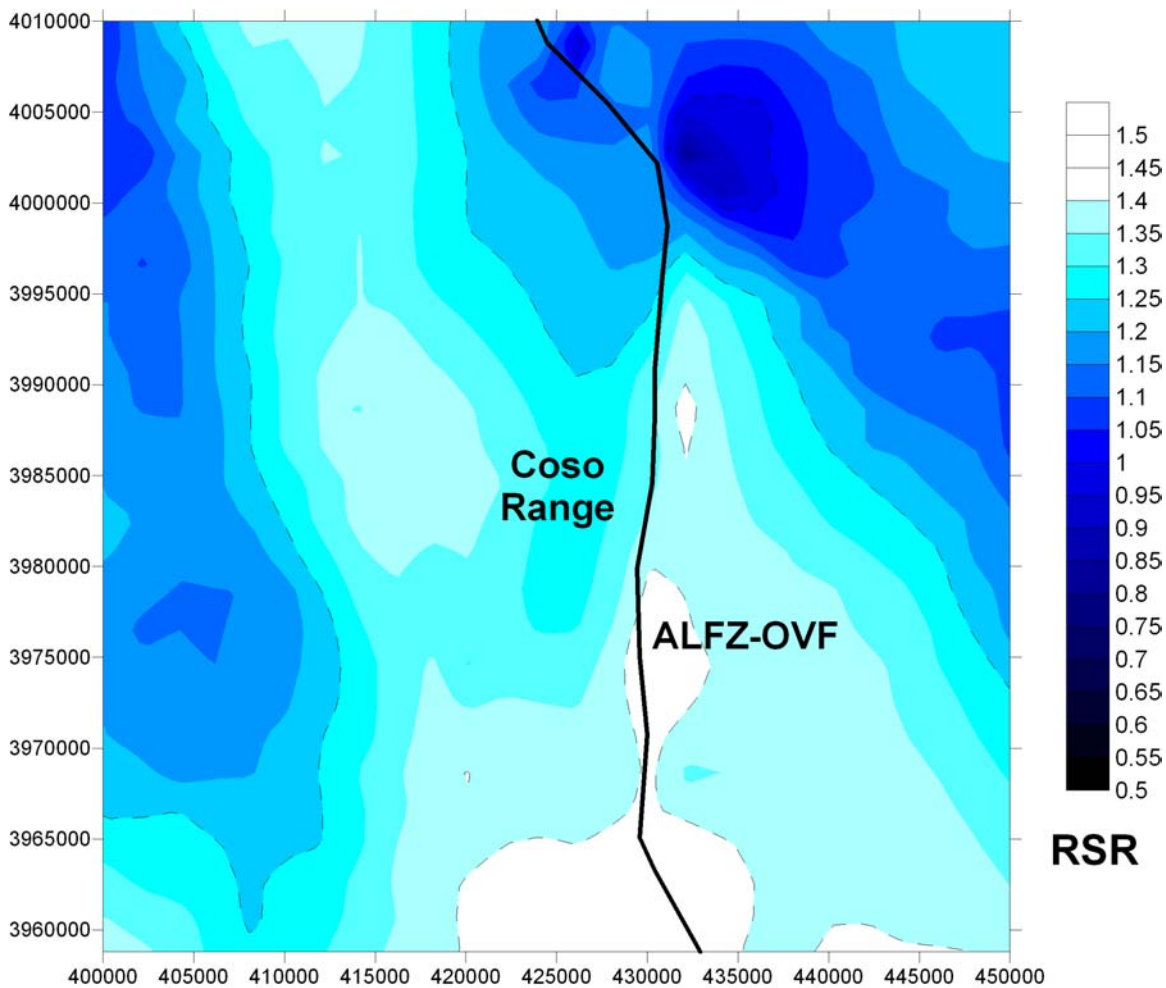


**Figure 6.16:** Regime-Stress-Ratio (RSR) distribution for the ALFZ-OVF and the Coso Range. The through-going fault is situated in regions of strike-slip while the bulk of the Coso Range exhibits more transtensional tectonics.

## 6.7. Discussion

The ECSZ has been the focus of many studies and is being recognized as a transition zone between strike-slip tectonics from the North America–Pacific Plate boundary and extensional tectonics from the Basin and Range. Unruh et al. (2003) present a transtensional model for the Sierra Nevada frontal fault system in which the Owens Valley Fault–Airport Lake Fault Zone (OVF-ALFZ) is the southernmost section of a releasing step-over towards the Mohawk Valley Fault in the north. Consequently transtensional deformation in the ECSZ is widely expressed both by dextral strike-slip on major faults (OVF-ALFZ, PVF, DVF) associated to Sierra Nevada motion relative to stable North America as well as normal faulting associated to crustal thinning.

Hearn and Humphreys (1998) model the Walker Lane Belt kinematics in the northern ECSZ using a 2D FE model consisting of various tectonic blocks separated by active faults. In their model they use the concept of split and slippery nodes for the contact surfaces (faults; Melosh and Raefsky, 1981). They solved their models for tectonic block motions and fault slip rates and then derived deformation styles. A similar approach is

undertaken by Eckert & Connolly (2004) who showed that 2D FE models can be used to model the seismicity and strain pattern due to the releasing bend geometry of the OVF-ALFZ in the vicinity of the Coso Range. The driven fault slip approach is applicable for geodetic models that focus on the resulting fault slip rates. However, using active fault slip to drive the model is a) not applicable for complex 3D fault geometries, and b) it does not represent an energetically correct approach to model the in-situ state of stress. Faults react in response to tectonic forces, such as block motions, basal tractions or slab pull. These forces, together with gravitational loading, have to be mimicked using loading conditions, which are applied on the model geometry boundaries. In summary, these models do not represent the actual lithospheric stress magnitudes, as mentioned by Hearn and Humphreys (1998), and are hence not applicable for determining the actual “tectonic” state of stress.

The modeling procedure presented here is based on gravitational potential energy differences ( $\Delta GPE$ ) due to crustal thickness variations and tectonic loading and generates a 3D state of stress for the ECSZ that matches independent observations both for stress orientations and magnitudes. Furthermore, surface deformation after the 1000yrs GPS displacement step match observed GPS velocities. The models generate a transtensional tectonic regime in the ECSZ and at shallow depths (>-3000m) the major active faults of the ECSZ are situated in corridors of pure strike-slip deformation. This shows the role of these faults in the tectonic regime. The Owens Valley Fault, the Panamint Valley Fault and the Death Valley Fault accommodate dextral strike-slip whilst bulk deformation is accommodated by transtensional and extensional deformation between the fault sets. With increasing depth (<-3000m) transtension and extension becomes more dominant and pure strike-slip tectonics are absent. At these depths the faults still exhibit transtension while extension is widely expressed in the Basin and Range and in the Sierra Nevada. This is consistent with findings by Vetter and Ryall (1983) who conclude that the vertical stress magnitude  $S_V$  increases with depth more rapidly than  $S_H$ .

The modeled state of stress of the Coso Range exhibits strike-slip to transtensional tectonics which is consistent with focal mechanism data (e.g. Walter and Weaver, 1980; Feng and Lees, 1998; Bhattacharyya and Lees, 2002). Focal mechanism derived stress ratios ( $R = \sigma_2 - \sigma_3 / \sigma_1 - \sigma_3$ ) by Feng and Lees (1998) yield R ranging from 0.4 to 0.86 with an average of 0.685. This corresponds to Regime-Stress-Ratio (RSR) values ranging from 1.6 to 1.14 with an average of 1.385. These RSR values relate very well to the modeled ones (Figure 6.14) for the Coso Range which are in the Range of 1.45-1.2 (at z=-3000m, which represents the average depth of regional seismicity, Walter and Weaver, 1980). Derived  $S_H$  orientations are N10°E – N15°E and match independent data from the WSM (Figure 6.7) and results by Roquemore (1980) who infers  $S_H$  to be N15°E-N25°E. The RSR distribution on the surface of the ALFZ-OVF shows that strike-slip deformation is predicted throughout the Coso Range, supporting the hypothesis of a connected ALFZ-OVF structure (Unruh et al., 2002).

The modeled state of stress in the Owens Valley is characterized by strike-slip tectonics near surface and transtensional tectonics at greater depths. RSR distribution on the entire ALFZ-OVF indicates that strike-slip regimes are most pronounced in the Owens Valley and that strike-slip deformation is possible for depths < 8km. Zoback's (1989)

analysis of fault slip vectors concludes that the Owens Valley Fault is situated in a stress field that has  $R=1.0$ . This corresponds, both for strike-slip and extensional regimes, to a RSR of 1.0 representing transtension and allowing strike-slip and extensional faulting. The coexistence of both normal and strike-slip faulting on the Independence Fault and the Owens Valley Fault, respectively, have lead to two different interpretations for the state of stress of the Sierra Nevada frontal zone in the western part of the ECSZ. One hypothesis is based on temporarily or spatially varying regional stresses (Zoback and Zoback, 1989; Zoback, 1989; Bellier and Zoback, 1995; Monastero et al., 2002) and the other on fault slip partitioning within a single regional stress field (Wesnousky and Jones; 1994; Le et al., 2007). The results presented in this modeling study (although not capable to account for temporal changes in stress) suggest a consistent state of stress ( $0.8 > R > 0.5$ , Figure 6.14) in the ECSZ regionally varied by topography.  $R$  maxima ( $R > 0.8$ ) are associated with topographic maxima. The major faults are situated in structural depressions and thus exhibit a greater influence of strike-slip loading. At  $z=-3000\text{m}$  the Owens Valley Fault ( $R=0.5$ ) is located in a corridor of pure strike-slip and the Independence Fault ( $R=0.7$ ) exhibits transtension. Furthermore, the steep fault dip of the Owens Valley Fault ( $85^\circ$ , Wesnousky and Jones, 1994) compared to the dip on the Independence Fault ( $60^\circ$ , Wesnousky and Jones, 1994) additionally favors strike-slip tectonics. Thus, the scenario of a consistent regional stress field where slip is partitioned to account for the different deformation styles seems appropriate.

It is important to emphasize that the modeled state of stress is the result of the submodeling procedure driven by the displacement results from the SAF scale modeling. These boundary conditions incorporate the effect of the bending geometry of the SAF, which transfers increased horizontal stresses into the ECSZ (Figure 4.6, chapter 4), and thus is a major cause for the state of stress observed in the ECSZ. These findings are consistent with studies from Du and Aydin (1996) and Li and Liu (2006) who both conclude that the Big Bend perturbs and amplifies the surrounding state of stress and induces a zone of shearing coinciding with the ECSZ. This effect becomes even more evident when the ECSZ is driven with boundary conditions interpolating contemporary GPS displacements. While the surface displacement field is matched, these boundary conditions do not generate sufficient horizontal stresses to result in strike-slip or transtensional tectonic regimes at depth ( $<-1000\text{m}$ ), respectively. Hence it is possible to conclude that the contemporary GPS surface displacements do not contribute essentially to the state of stress observed in the ECSZ.

## 6.8. Conclusions

The modeling procedure presented has shown that the state of stress in a tectonically complex region like the ECSZ can be successfully simulated. The FE results are in agreement with independent data for stress magnitudes and orientations and yield a consistent state of stress in the ECSZ characterized by transtensional tectonic regimes with the major active faults being situated in corridors of strike-slip tectonics. The influence of the SAF geometry by using the ABAQUS submodeling technique is necessary to generate the observed state of stress since boundary conditions derived from contemporary GPS

displacements do not generate sufficient horizontal stress magnitudes to result in bulk transtension in the ECSZ.

## 7. State of stress in the Coso Range

### 7.1. Introduction

The Coso Geothermal Field in the Coso Range is located within the Eastern California Shear Zone (ECSZ) north of the Indian Wells Valley (IWV) and directly east of the Sierra Nevada frontal scarp. Current kinematic studies of this region (McCluskey et al., 2001) show that an average of 6.5mm/yr of dextral shearing is accommodated across the Coso Range. Unruh et al. (2002) suggest that the shear is transferred from the Airport-Lake-Fault-Zone via a right releasing bend setting northwards across the Coso Range to become the Owens Valley Fault. This transtensional transition zone drives crustal extension in the Coso Range and active strike slip and normal faults accommodate northwestward translation of the rigid Sierra Nevada micro-plate and (Unruh et al., 2002). A recent study by Monastero et al. (2005) concludes that the releasing bend hosts a nascent metamorphic core complex. Necessary crustal thinning is widespread over the Coso Range and is accommodated on high and low angle normal faults that nucleate on a shallow (~4km depth) brittle ductile transition zone (b-d-t). The geometry of the shallow b-d-t and the listric fault distribution resemble fully developed metamorphic core complexes.

Various stress and strain measurements/investigations have been undertaken in the Coso Range. Roquemore (1980), Feng and Lees (1998) and Unruh et al. (2002) conclude that the Coso Range is under NNE-SSW compression and WNW-ESE extension. Sheridan and Hickman (2004) conclude that the Coso Geothermal Field is dominated by a state of stress resulting in strike-slip tectonics. In summary, the stress and strain data support hypothesis of a current dextral transtensional stress regime in the ECSZ.

The scope of the submodeling study of the Coso Range scale is to construct a model that incorporates the complex structure and faulting pattern of the Coso Range and to establish a state of stress that is consistent with independent data and measures. Once this is achieved the modeled state of stress can be used to derive 2<sup>nd</sup> order fracture networks and fluid flow pathways (see chapter 8).

#### 7.1.1. Structure and faulting

In the southern Indian Wells Valley the dextral shear is mainly accommodated on a left stepping en-echelon fault zone, the Airport lake Fault Zone (ALFZ, Figure 7.1). Near the Coso Range and at the northern reach of the ALFZ, it splits up into a western branch, the Little Lake Fault (LLF) trending into the Rose Valley, and an eastern other branch, striking northwards, crosses the White Hills anticline and trends along the western margin of the Coso Wash (Figure 7.1). This fault is referred as the Coso Wash Fault (CWF) and along its trend it exhibits fumaroles, hot springs and steaming fissures. In detail this fault is represented by a series of left-stepping en-echelon fault segments. The Coso Wash Fault extends northwards to the Haiwee Springs Fault Zone (HSFZ). On the east of Coso Wash deformation occurs in the Wild Horse Mesa by a series of N-NE striking, west dipping normal faults, which Duffield and Bacon (1980) referred to as a “step-faulted terrain”.

Evidence of late Cenozoic faulting is widespread in the Coso Range and has been mapped by Duffield and Bacon (1980) and Whitmarsh (1998, Figure 7.3). Generally, two

sets of faults are observed in the Coso Range. High angle ( $60^{\circ}$ - $70^{\circ}$ ) faults striking between N15E and N25E are common throughout the Coso Range and generally exhibit extensional displacement with a varying dextral component. NW trending faults bound the south side of the Coso Range and are generally well developed within the southern and western parts of the range.

In the north of the Coso Range, the Owens Valley Fault (OWF) is the major active structure along the eastern boundary of the Sierra Nevada. Slip rates of  $\sim 6\text{mm/yr}$  on the OWF and  $5\text{mm/yr}$  on the ALFZ suggest that the faults in the Coso region transfer the dextral slip from the ALFZ in the Indian Wells Valley (IWV) to the OWF in the north of the Coso Range (Unruh et al., 2002).

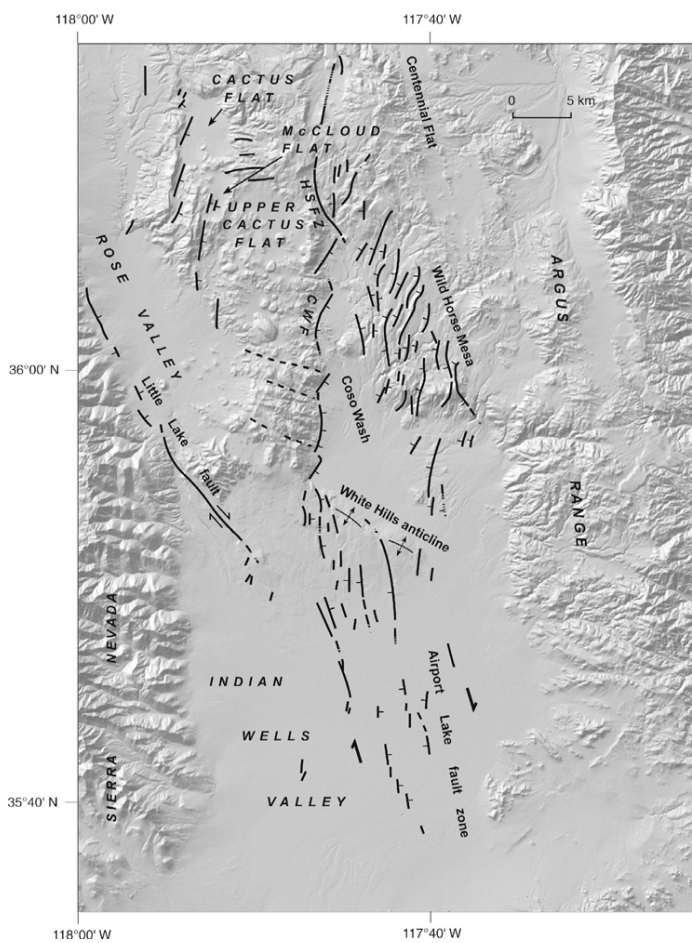


**Figure 7.1: Structural map of the Coso Region after Unruh et al., 2002.**

### 7.1.2. Seismicity

The Coso Range (CR) and the Indian Wells Valley (IWV) have a long history of earthquake swarms related to both tectonic and geothermal activity. The majority of earthquakes are relatively small, i.e.  $M < 3.0$  and locate at depths of 1 to 8 km. However, several large earthquakes, i.e.  $M > 5.0$ , between 1995 and 1998 (Bhattacharyya and Lees, 2002), emphasize the importance of monitoring seismicity in this region. The seismicity in the Coso Range and the Indian Wells Valley is due to rupture along tectonically active structures (e.g. Bhattacharyya and Lees, 2002) whilst seismicity in the Coso Geothermal Field (CGF) is associated to injection and production of geothermal fluids (e.g. Feng and

Lees, 1998). The Little Lake Fault and the Airport Lake Fault Zone (ALFZ) are the most significant active structures in the Indian Wells Valley whilst seismicity in the Coso Range is mostly located in the CGF and in the northern Coso Range. Focal mechanisms in the Coso Range –Indian Wells Valley region are heterogeneously distributed forming clusters of normal, oblique and strike-slip faulting styles (Figure 7.2, after Bhattacharyya and Lees, 2002) reflecting the transition of extensional to strike-slip tectonics. It should be noted that also reverse faulting mechanisms are not uncommon, especially in the ALFZ and in parts of the CGF. Bhattacharyya and Lees (2002) conclude that the central CGF belongs to a transtensional tectonic regime surrounded by a region under transpression.

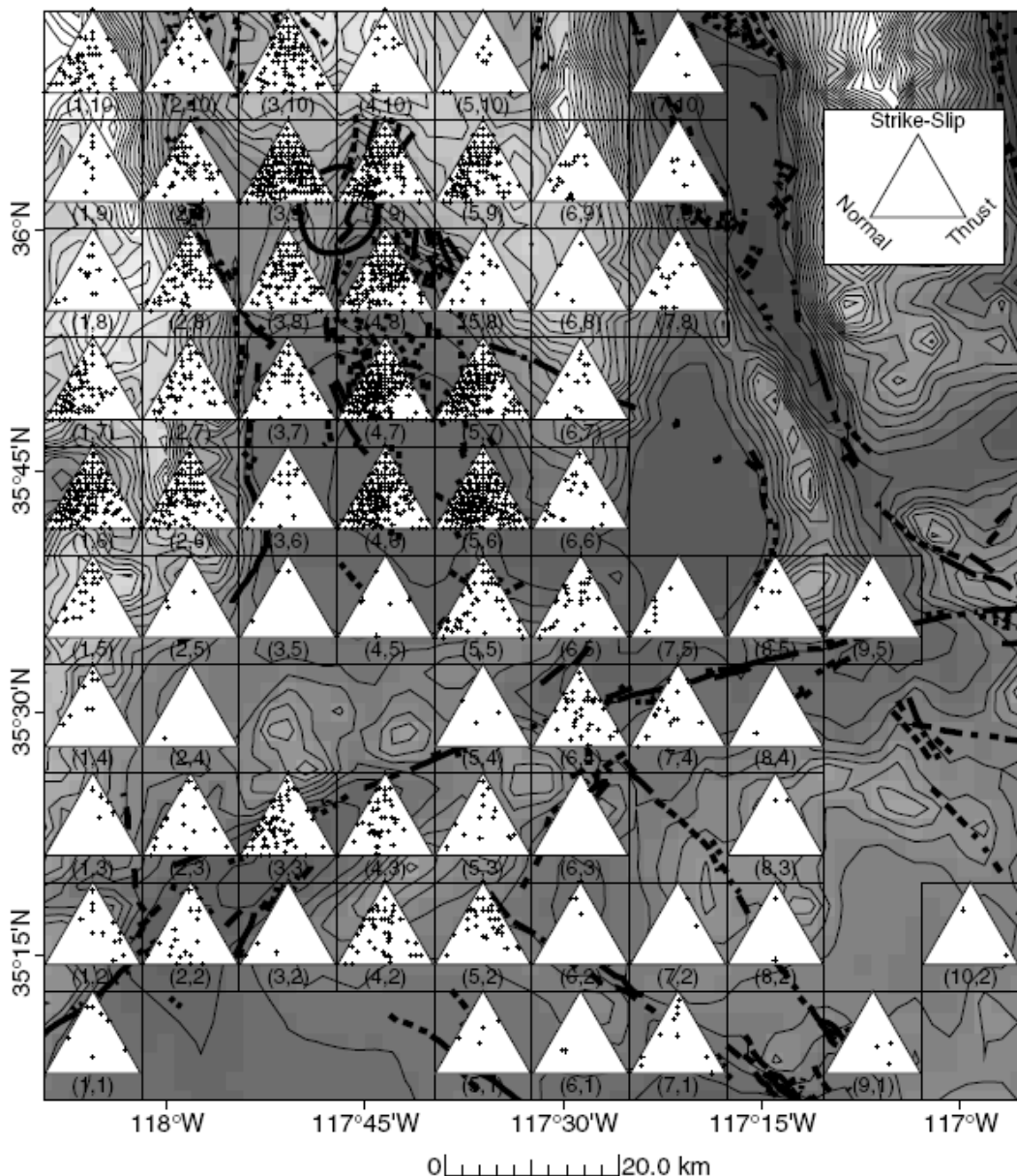


**Figure 7.2:** Seismicity shown of the Coso Range - Indian Wells Valley region shown on ternary diagrams (Frohlich, 1992, Figure after Bhattacharyya and Lees, 2002). Faults in the region generally accommodate normal to strike-slip tectonics. Note the presence of reverse faulting mechanisms in the ALFZ and in the Coso Geothermal Field highlighted by the circle at 36°N latitude.

## 7.2. Model construction

The model geometry comprises the Coso Range, the Indian Wells Valley and the southern Owens Valley. The model has dimensions of 70km\*100km\*45km. The average mesh density is 500m-1km and a total of ~1,800,000 tetrahedral elements are used.

**Topography:** Surface topography is based on a DEM model with a resolution of 500m.

**Faults:** The surface fault distribution in the Coso Range is based on the GIS map of Whitmarsh (1996, Figure 7.3a). Based on analysis by Unruh et al. (2002) faults in the Coso Range, namely the Coso Wash fault set and the Wild Horse Mesa faults, are constructed so that these faults have a listric shape detaching on the brittle-ductile-transition zone (b-d-t). Due to the complexity of the fault distribution in the Coso Range, 44, active, faults are included in the model (Figure 7.3b). These are:

- faults of the Airport Lake Fault Zone (after Jennings, 1994)
- set of faults defining the Coso Wash Fault
- Wild Horse Mesa faults
- Faults in the area of the Cactus Flat
- Southern branches of the Owens Valley Fault (after Jennings, 1994)

Table 7.1 lists the corresponding fault dips modeled.

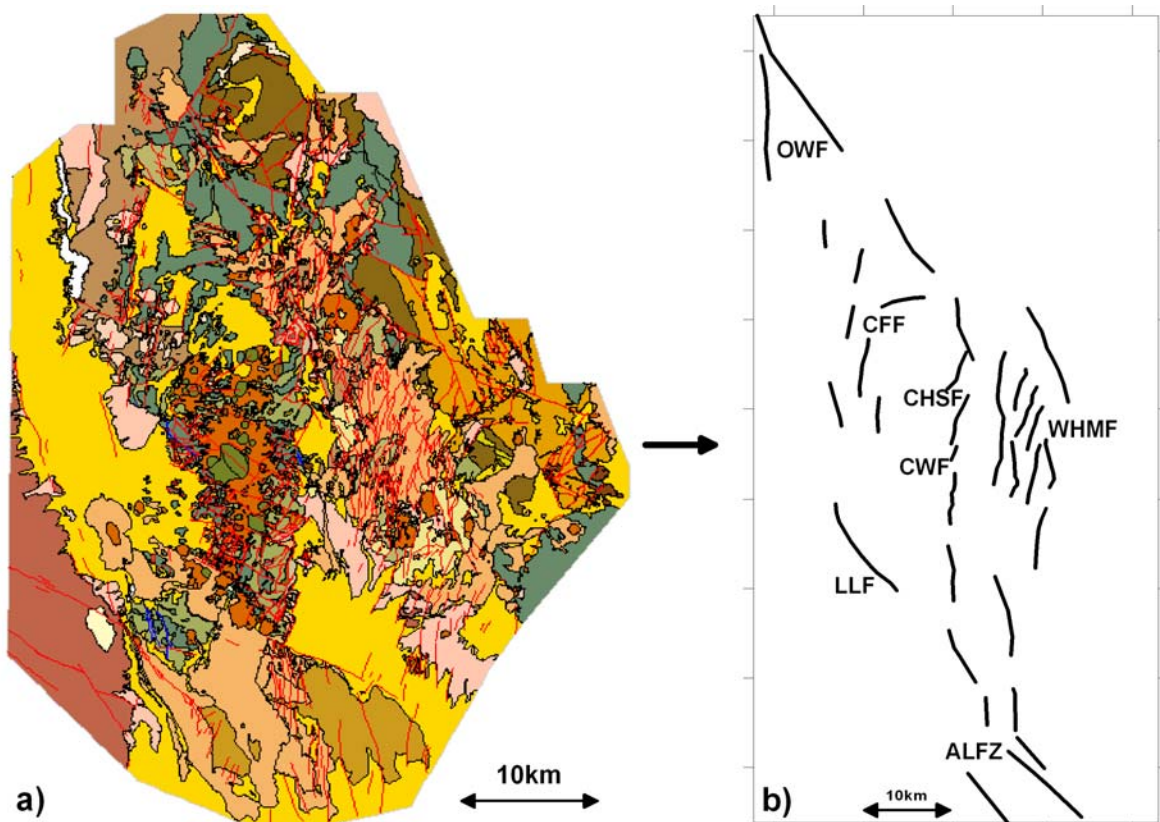
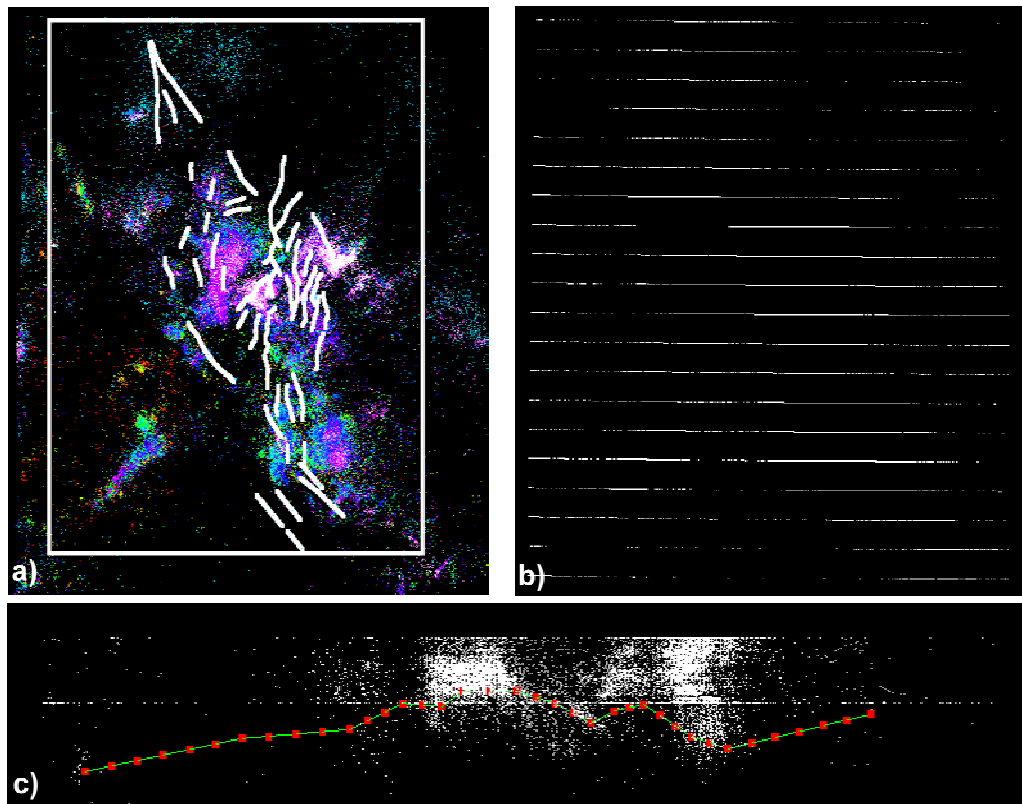


Figure 7.3: a) Geologic map of the Coso Range (Whitmarsh, 1998). Red lines are faults exported to pre-processing software. b) Faults of the Coso Range used in the modeling study. ALFZ (Airport Lake Fault Zone), WHMF (Wild Horse Mesa Fault), CWF (Coso Wash Fault), LLF (Little Lake Fault), CHSF (Coso Hot Springs Fault), CFF (Cactus Flat Fault), OVF (Owens Valley Fault).

Fault	Dip [°]	comment	Reference
Coso Wash Fault	70	listric	Unruh et al., 2003
Airport Lake Fault Zone	90	near vertical	Roquemore (1980)
Coso Hot Springs Fault	45-50		Roquemore (1980)
Wild Horse Mesa Faults	65	for strike-slip events	Unruh et al., 2003
Owens Valley Fault	85		<a href="http://www.consrv.ca.gov/CGS">www.consrv.ca.gov/CGS</a>
Little Lake Fault	90		<a href="http://www.consrv.ca.gov/CGS">www.consrv.ca.gov/CGS</a>
Sierra Nevada Front	60		<a href="http://www.consrv.ca.gov/CGS">www.consrv.ca.gov/CGS</a>

**Table 7.1:** Fault dips for modeled faults.

**BDT:** An important factor influencing the state of stress in the Coso Range is the location of an elevated, shallow brittle-ductile-transition zone (b-d-t, Unruh et al., 2002, Monastero et al., 2005). A surface representing the b-d-t is included, its' geometry based on the local seismicity data. The change in rheology is defined by the base of seismicity. Earthquake data from 1980-2005 (SCEC) is used to generate cross sections throughout the model area (Figure 7.4a,b). The seismicity data is projected to 20 cross sections distributed over the Coso Range. In each cross section a line defines the base of seismicity (Figure 7.4c). The 20 lines are then used to generate a regular grid in GOCAD to construct a surface of the b-d-t.



**Figure 7.4:** a) Distribution of regional seismicity from 1980-2005 in the Coso Range (Data from SCEC). b) Seismicity data is projected to 20 vertical cross sections. c) At each cross section the base of seismicity is digitized and then a surface of the b-d-t is constructed from the digitized lines.

**Moho:** The implementation of a Moho surface posed a problem since, unfortunately, no dataset for a continuous Moho map is available for the ECSZ and the Coso Range. Although the crust2.0 data set (Bassin et al., 2000) is available, it is based on  $2^\circ$  by  $2^\circ$  resolution which is larger than the model dimensions. Thus Moho data from two studies by Zhu and Kanamori (2000) and Fliedner et al. (2000) are combined and a composite surface constructed.

The final FE mesh comprises ~2,000,000 tetrahedral elements with a total of 44 faults implemented as contact surfaces.

**Rheology:** As for the previous scale models only linear elastic rheologies are used (Table 7.2). Although the b-d-t is included in the model the lower crust is represented by an elastic material contrast. The elastic parameters used are derived from seismic velocity analysis in the Coso Range. The Coso Range has p-wave velocities of 15000-20000 ft/s (Unruh et al. 2001). Standard empirical equations (equation 6-1, chapter 6) allow inversion of a corresponding Young's modulus (Table 7.2).

Viscoelastic material parameters have not been used since the shape of the b-d-t forces the model to “flow apart” and unrealistic, or at least unobserved, surface displacements to occur. Thus, stable boundary conditions have not been found that keep the model in equilibrium with viscoelastic materials.

	Density $\rho$ [kg/m <sup>3</sup> ]	Young's Modulus [GPa]	Poisson's ratio $\nu$
Upper Crust	2670	65	0.25
Lower Crust	2850	85	0.275
SN Upper Crust	2690	70	0.275
SN Lower Crust	2850	90	0.3
Mantle	3280	150	0.325

Table 7.2: Elastic parameters used.

### 7.3. Loading procedure

The loading procedure for the Coso Range scale model comprises the following steps:

- Gravitational pre-stressing and fit to Sheorey model
- Submodel analysis from tectonic loading step of the ECSZ scale
- Submodel analysis from displacement loading step of the ECSZ scale

#### 7.3.1. Sheorey calibration

The Sheorey curve of 80GPa is used as an average for the crust in the model (Figure 7.5).

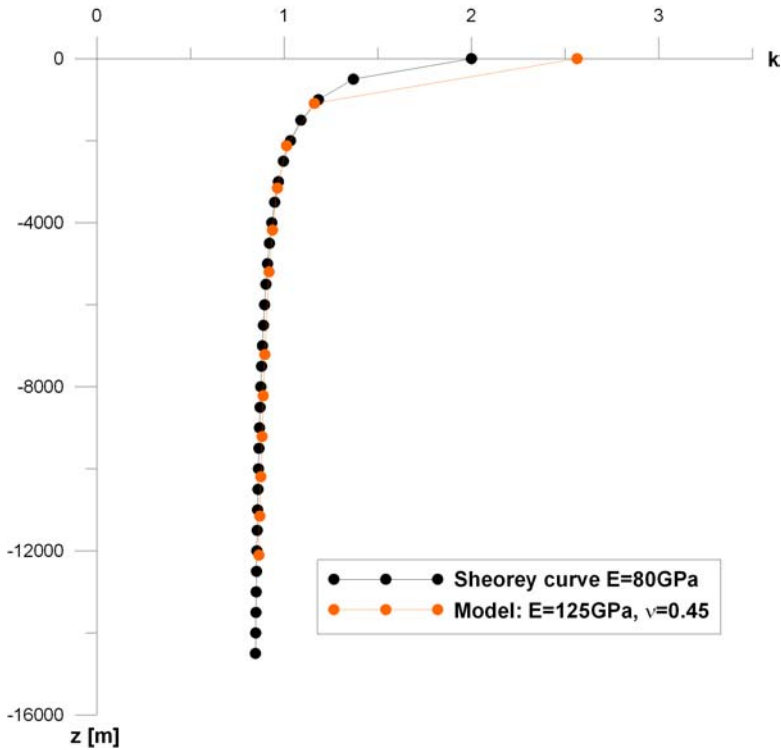


**Figure 7.5: Sheorey calibration for the gravitational initial state of stress. The model is matched against the Sheorey curve of 80GPa as an average E for the crust in the model.**

### 7.3.2. Tectonic loading submodel analysis - Model calibration

**Regime-Stress-Ratio (RSR; see chapter 2.7):** The modeled tectonic regimes at  $z=-1000\text{m}$  (Figure 7.6a) yield strike slip tectonics, i.e.  $\text{RSR}=1.5$ , for the ALFZ, the IWV and the southern Coso Range. Within the Coso Range the Coso Wash Fault (CWF) is situated in a corridor of increased strike slip influence, indicating that the dextral shear is accommodated along this fault. The northern Coso Range is under transtension. At  $z=-3000\text{m}$  (Figure 7.6b) the Coso Range is under transtension and pure strike slip tectonic are restricted to the Airport Lake Fault Zone. The CWF still exhibits more strike-slip influence than the bulk of the Coso Range.

**$S_H$  orientation (Figure 7.6c):** In general, a very distinct stress field of  $N5^\circ\text{E}-N20^\circ\text{E}$  can be observed across the Coso Range. Slight variations from this trend can be observed locally near faults, where  $S_H$  is oriented  $>N20^\circ\text{E}$ . The modeling results (green ticks) show a very good fit to data from the WSM (blue ticks). Only slight variations occur at single data points. It should be noted that a difference grid compared to the WSM orientations (as conducted for the SAF and ECSZ scale) is not possible for the Coso Range since the data is spatially concentrated on the central and southern Coso Range and thus a complete grid would be based on interpolation. Hence, for the quality of  $S_H$  orientations individual data points have to be compared.

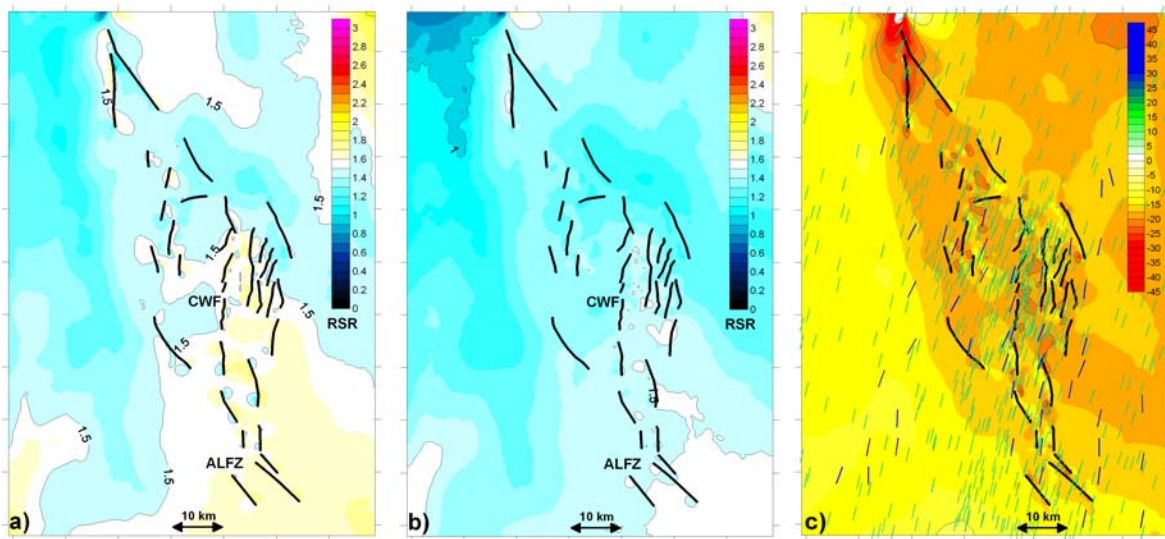


**Figure 7.6:** a) Regime-Stress-Ratio (RSR) at  $z = -1000\text{m}$  yields more strike-slip influence. b) RSR at  $z = -3000\text{m}$  yields transtension for the Coso Range. c)  $S_h$  orientation does not change compared to previous models.

**Stress magnitudes:** The modeled stress magnitudes for  $S_h$ ,  $S_v$  and  $S_h$  provide a good fit to the measured stresses (Figure 7.7). Although the modeled  $S_h$  seems to be slightly too high, it should be noted that the interpolated stresspath by Sheridan et al. (2004) is based on a single measurement.  $S_v$  is slightly overestimated since the model density of  $\rho = 2670\text{kg/m}^3$  is slightly higher than the density of  $\rho = 2630\text{kg/m}^3$  used by Sheridan and Hickman (2004).

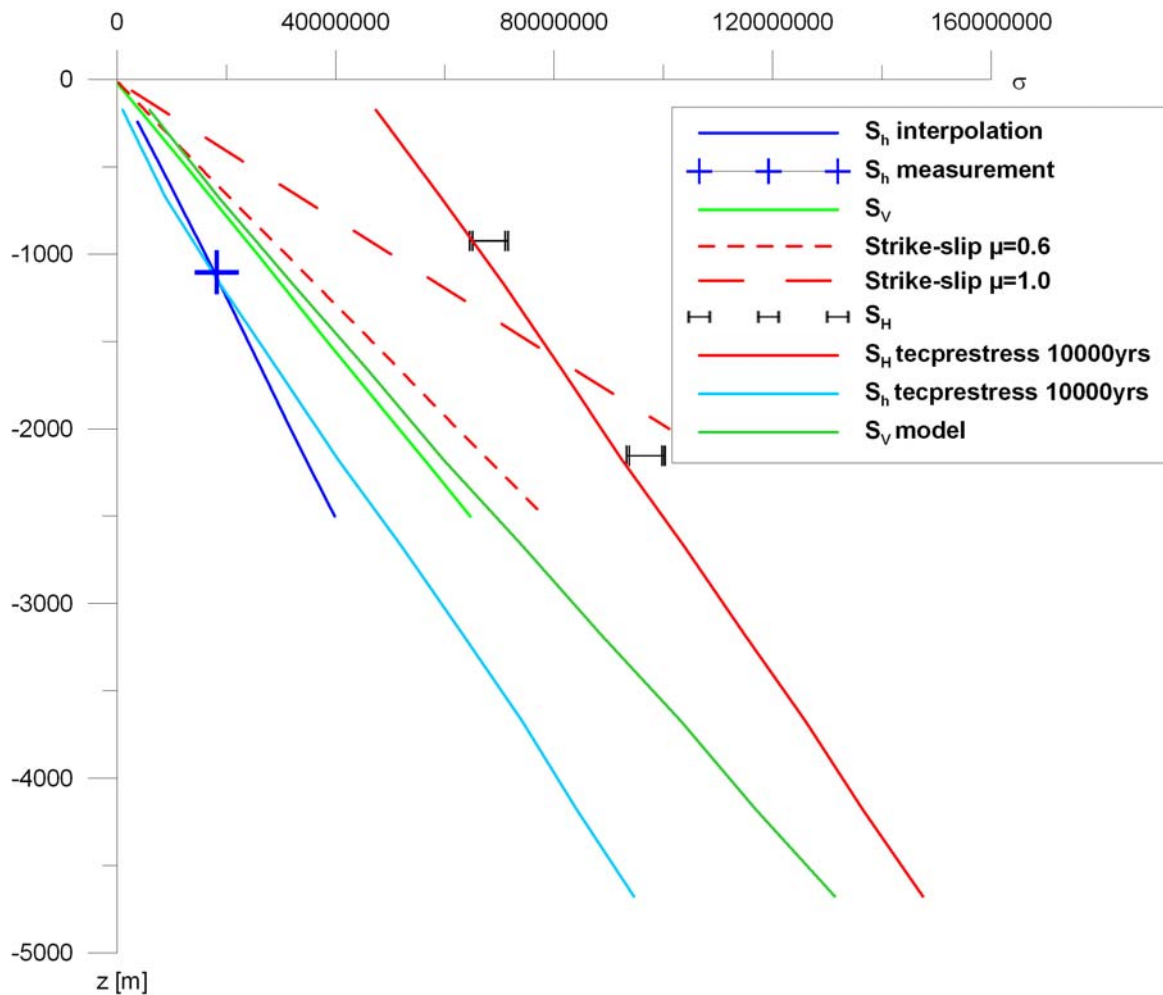


**Figure 7.7: Stress magnitudes for the new tectonic pre-stressing. The modeled paths for  $S_H$ ,  $S_h$  and  $S_v$  provide a good fit to the measures.**

### 7.3.3. State of stress in the Coso Range after displacement loading submodel analysis

The addition of 1000yrs of GPS velocity derived displacement loads does not significantly change the modeled state of stress. The strike slip influence at  $z=-1000\text{m}$  is slightly increased (Figure 7.8a,b). At  $z=-3000\text{m}$  most of the Coso Range is transtensional and strike-slip tectonics are restricted to the Airport Lake Fault Zone and east of the Coso Wash Fault (CWF). The stress orientations remain essentially unchanged (Figure 7.8c). The stress ratio  $R$  for the Coso Range yields a uniform state of stress that has  $0.8 > R > 0.45$  (Figure 7.8d).  $R$  maxima of  $>0.8$  are associated to topographic maxima in the Sierra Nevada and in the northern Coso Range. Stress magnitudes for  $S_H$  and  $S_h$  are slightly greater (Figure 7.9) but still match the data by Sheridan and Hickman (2004).

The slight overestimation of modeled  $S_h$  magnitudes results from the calibration to the 80GPa Sheorey curve as an average for the crust. Using a smaller calibration curve of Sheorey (i.e. 70GPa as for the ECSZ scale) results in negative  $S_h$  magnitudes and is thus considered unrealistic.

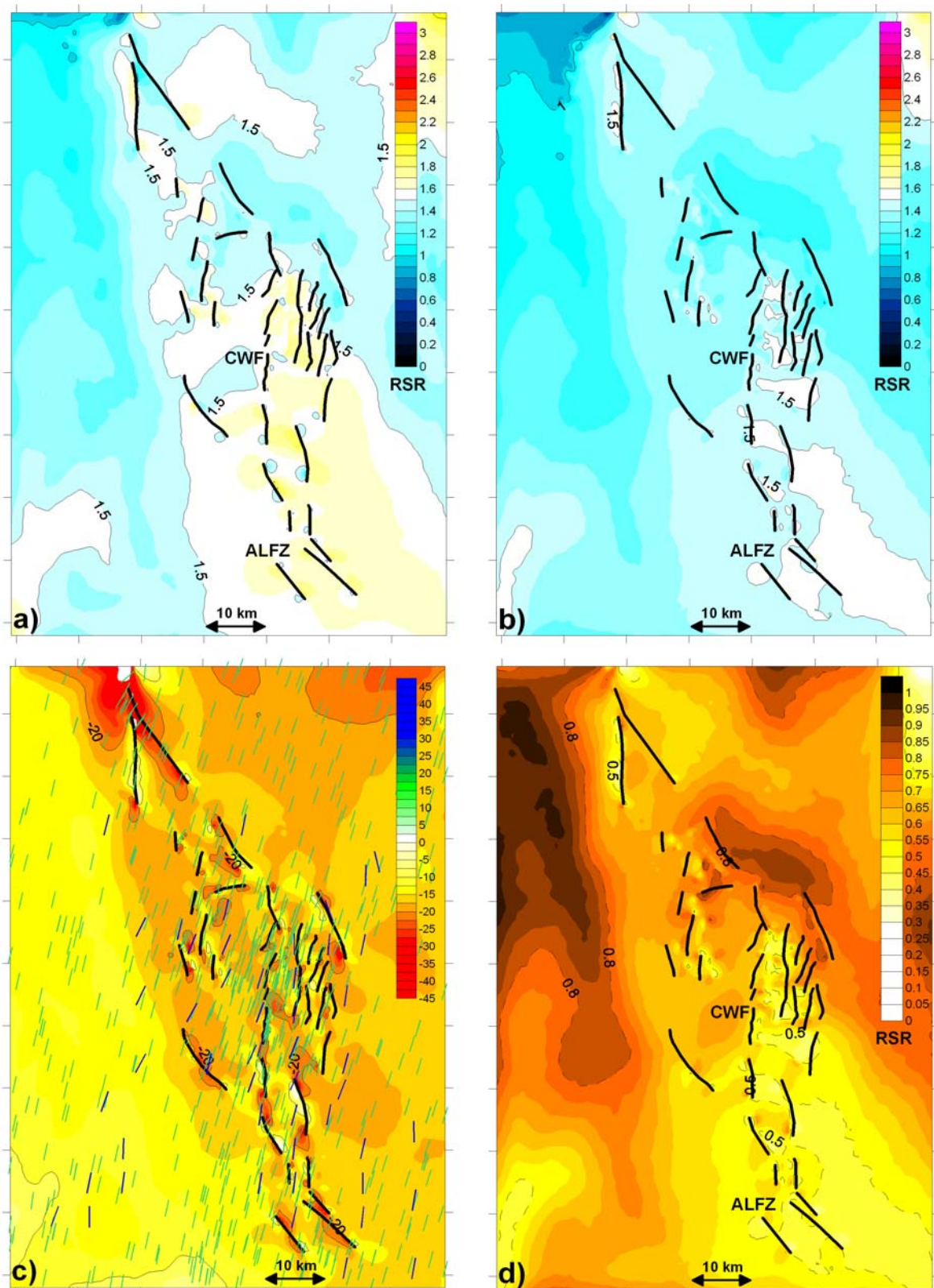


**Figure 7.8:** a) Regime-Stress-Ratio (RSR) at  $z=-1000\text{m}$ : strike-slip influence is slightly reduced. b) RSR at  $z=3000\text{m}$  yields transtension for the Coso Range. c)  $S_H$  orientation does not change compared to previous models.

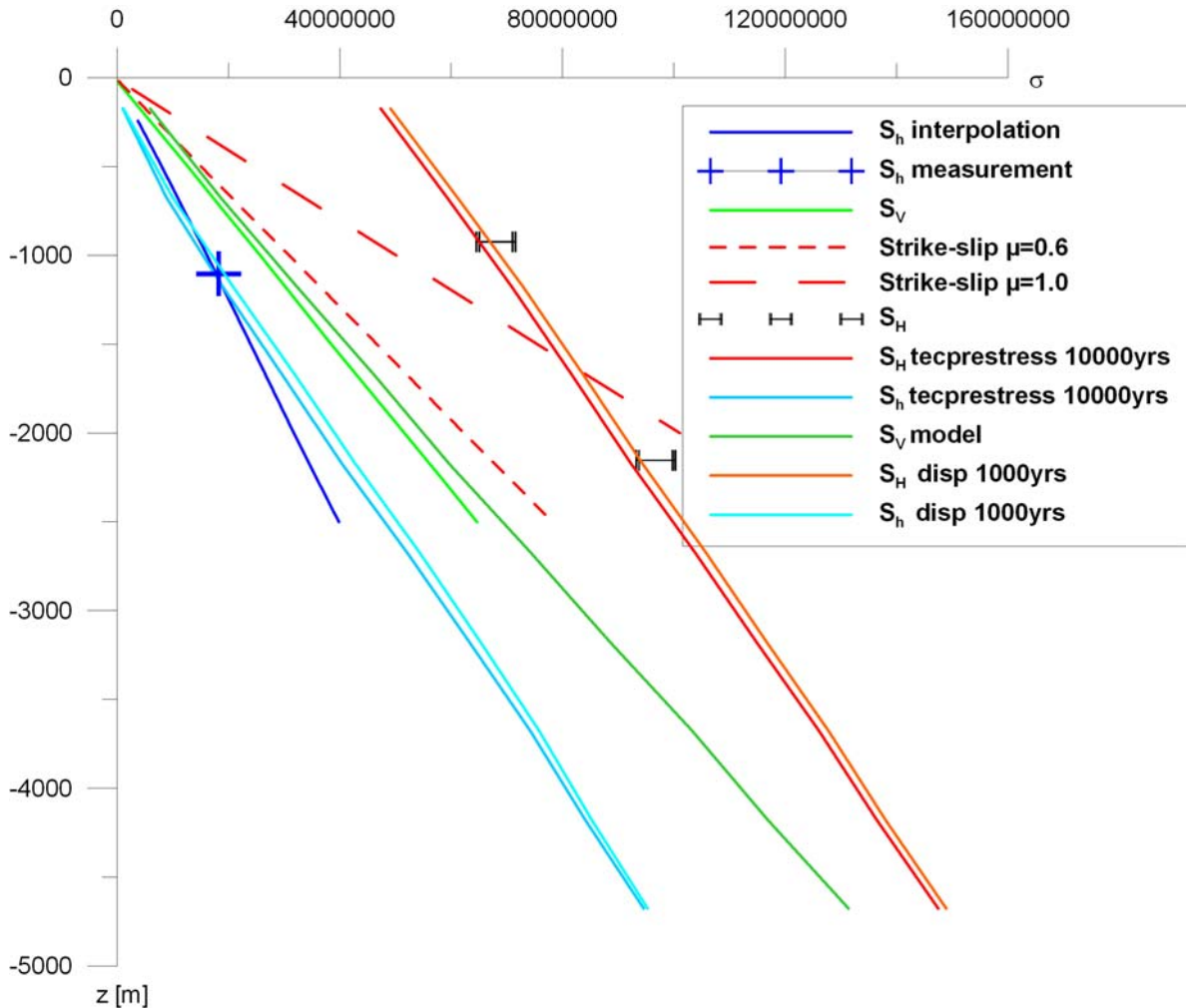


**Figure 7.9: Stress magnitudes after the 1000yrs displacement loading step are only slightly increased and still match the stress measurement in the Coso Geothermal Field.**

#### 7.4. State of stress for the Coso Geothermal Field

In context of the following fracture and fluid flow analysis the state of stress in the vicinity of the Coso Geothermal Field (CGF) becomes of particular interest. Focal mechanisms inversions, strain data and well bore data (Feng and Lees, 1998; Unruh et al., 2002; Sheridan and Hickman, 2004) observe a transitional state of stress between extensional and strike-slip faulting, i.e. transtension in the Coso Range. In general, the Coso Range is under NNE compression and WNW extension. Davatzes and Hickman (2006) observe a consistent mean  $S_H$  orientation of  $N18^\circ E \pm 24^\circ$  based on borehole data and focal mechanism inversions in the area of the CGF. The modeled and spatially gridded  $S_H$  orientations for the vicinity of the CGF yield a mean orientation of  $N16.5^\circ E \pm 4.3^\circ$  which correlates very well to Davatzes and Hickman's (2006) observations. The modeled state of stress in the area of the CGF is characterized by strike-slip tectonics near surface and transtensional tectonics with increasing depth (Figure 7.8 a,b). Stress ratios for the area of the CGF ( $R = \sigma_2 - \sigma_3 / \sigma_1 - \sigma_3$ ) derived from focal mechanism data by Feng and Lees (1998) yield  $R$  ranging from 0.69 to 0.8 with an average of 0.73. This corresponds to Regime-Stress-Ratio (RSR; see chapter 2.7) values ranging from 1.2 to 1.3 with an average

of 1.27. The  $S_h$  upper bound estimates from Sheridan and Hickman (2004) yield a RSR=1.79 at  $z\sim 0$ m and RSR=1.63 at  $z\sim -1000$ m. These RSR values relate very well to the modeled ones (Figure 7.8a) for the Coso Range which are in the range of 1.5-1.6 at  $z=-1000$ m, and in the range of 1.3-1.4 at  $z=-3000$ m.

Davatzes and Hickman (2006) updated and reanalyzed the stress magnitude measurements for  $S_h$  and upper bounds for  $S_h$  for two wells (34-9RD2 and 38C-9) in the East Flank of the CGF (Figure 7.10). Based on a geophysical density log ( $2.65\text{g/cm}^3$ ) and on Coulomb frictional failure theory, normal faulting would occur at a critical  $S_h$  magnitude of (Jaeger and Cook, 2007):

$$S_{h,crit} = (S_V - P_p)/[(\mu^2 + 1)^{1/2} + \mu]^2 + P_p \quad (7-1)$$

Given the close proximity of the  $S_h$  measures to equation 7.1 Davatzes and Hickman (2006) inferred a preferred normal faulting regime for the CGF. They also argue that if the actual  $S_h$  magnitudes are close to the upper bounds for  $S_h$  which are greater or equal than the critical values required for strike-slip faulting, the state of stress in the CGF is then characterized by transtensional to strike-slip regimes. However, the absence of prevalent breakouts limits  $S_h$  estimation to upper bounds and thus  $S_h$  could be much smaller, leaving the propensity for strike-slip faulting uncertain. The conclusion of a normal faulting regime in the CGF agrees with previous studies based on InSAR and GPS derived surface displacements (Fialko and Simmons, 2000, Wicks et al., 2001) indicating subsidence above the CGF.

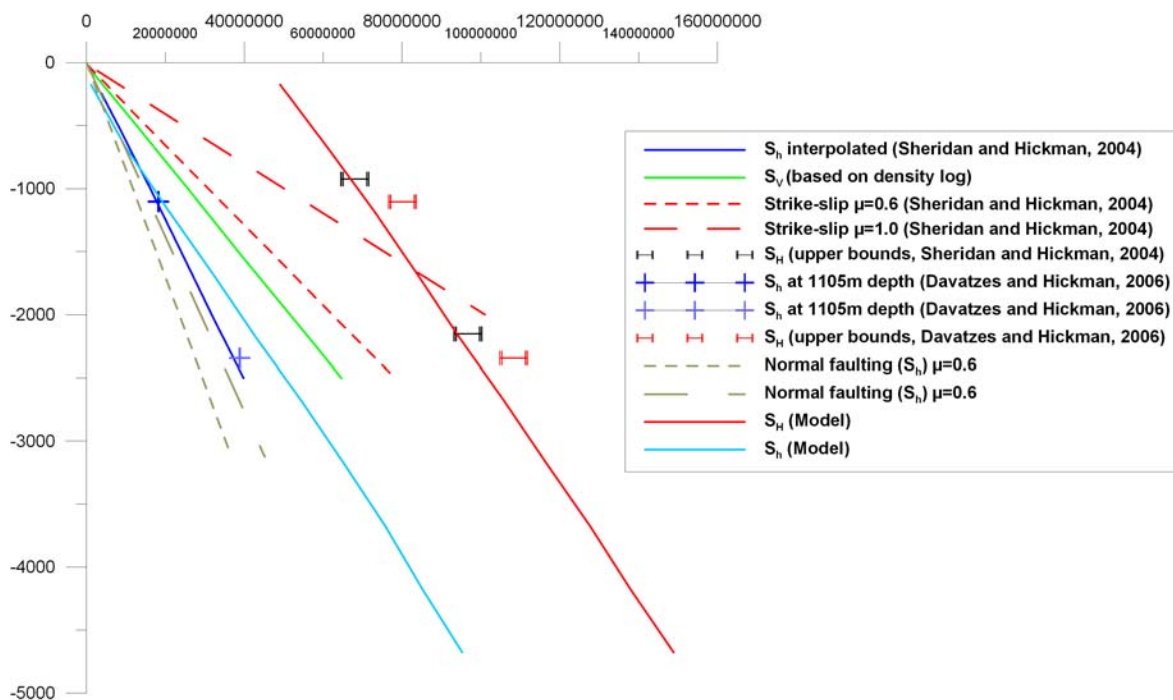


**Figure 7.10: Stress measurements, upper bounds for  $S_h$ , critical stresses for normal and strike-slip faulting for wells 34-9RD2 and 38C-9 by Davatzes and Hickman (2006) in the CGF East Flank.**

In order to further constrain the state of stress of the CGF, Regime-Stress-Ratio (RSR) based  $S_H$  magnitudes for extensional, transtensional and strike-slip regimes have been calculated using the measured data-points of Davatzes and Hickman (2006). For a pure extensional (i.e. normal) faulting regime  $RSR = 0.5 = (n + 0.5) + (-1)^n(R - 0.5)$  and with  $\sigma_1=S_V$ ,  $\sigma_2=S_H$ ,  $\sigma_3=S_h$ ,  $S_H$  can be derived from  $R = \sigma_2 - \sigma_3/\sigma_1 - \sigma_3$ . Using  $S_h=38.85\text{MPa}$  and  $S_V=60.96\text{MPa}$  (Davatzes and Hickman, 2006) gives  $S_H=49.91\text{MPa}$  at 2345m depth. For extensional as well as strike-slip faulting in a transtensional regime ( $RSR=1$ )  $S_H=S_V=60.96\text{MPa}$  and for pure strike-slip faulting ( $RSR=1.5$  and  $\sigma_1=S_H$ ,  $\sigma_2=S_V$ ,  $\sigma_3=S_h$ )  $S_H=83.07\text{MPa}$ . Correspondingly,  $S_H$  magnitudes have been calculated for 1105m depth, where  $S_h=18.24\text{MPa}$  and  $S_V=28.95\text{MPa}$  (Table 7.3).

	Normal faulting in normal faulting regime	Normal or strike-slip faulting in transtensional regime	Strike-slip faulting in strike-slip regime
$S_H(z=1105\text{m})$	23.59MPa	28.95MPa	39.66MPa
$S_H(z=2345\text{m})$	49.91MPa	60.96MPa	83.07MPa

**Table 7.3: Regime-Stress-Ratio (RSR) derived  $S_H$  magnitudes for various tectonic regimes.**

A pure normal faulting regime for the East Flank of the Coso Geothermal Field (CGF) as inferred by Davatzes and Hickman (2006) requires  $S_H$  to be very small, e.g. 10MPa smaller than  $S_V$  for  $z=2345\text{m}$ . Given the variety of focal mechanisms for the CGF, Bhattacharyya and Lees (2002) report a majority of strike-slip and normal faulting but also thrust faulting mechanisms for the CGF, a pure extensional or normal faulting regime is considered to be unlikely. Based on focal mechanism inversions Bhattacharyya and Lees (2002) conclude that the central CGF is situated in a transtensional tectonic regime surrounded by a region under transpression. This is consistent with the average stress ratio of  $R=0.73$  derived by Feng and Lees (1998) which indicates a transition of a transtensional to a strike-slip faulting regime ( $RSR=1.27$ ). The modeling results are also indicating that a transtensional to strike-slip tectonic regime in the upper 4km of the crust of the Coso Range is more plausible. Modeled  $S_H$  magnitudes are lower than the upper bounds and the state of stress facilitates normal faulting, strike-slip and reverse faulting, consistent with the observation of earthquake focal mechanisms (Bhattacharyya and Lees, 2002). Subsidence maxima (Figure 7.11) coinciding with the Coso Wash Fault and the Wild Horse Mesa Fault suggest that normal faulting is present in the Coso Range, but the state of stress is transtensional and faults also accommodate strike-slip deformation.

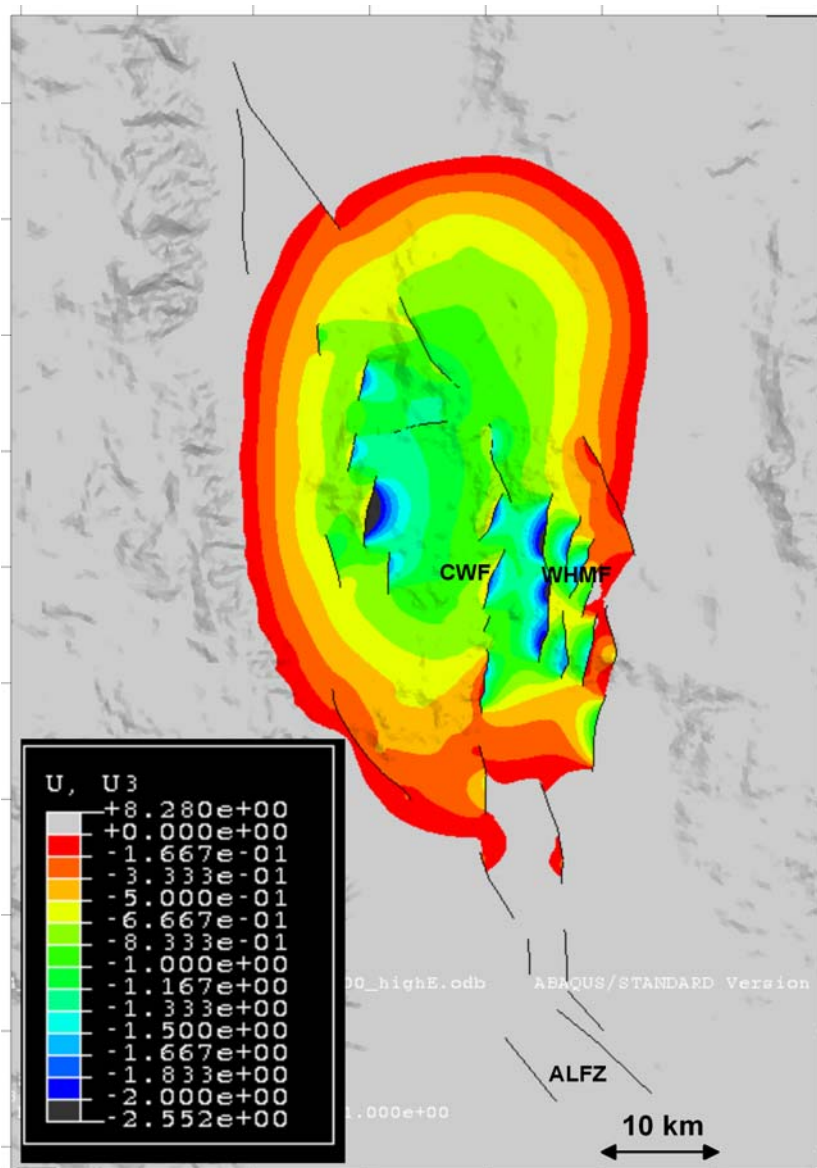


**Figure 7.11:** Vertical displacement for the Coso Range. The area of the Coso Geothermal Field is situated in a region of subsidence, indicating the influence of the releasing bend setting, forming a pull-apart structure. Regions of increased subsidence are associated to the Coso Wash Fault (CWF) and the Wild Horse Mesa Fault (WHMF) indicating strong normal faulting character.

## 7.5. Conclusions

The loading procedure consisting of gravitational pre-stressing, tectonic loading based on the multi scale submodeling analysis and contemporary loading based on GPS velocities of the Coso Range yields a state of stress which provides a very good fit to independent observations. The tectonic regimes in the Coso Range exhibit strike-slip and transtensional tectonics. Stress orientations are distinct ( $\sim N5^\circ E$ - $N20^\circ E$ ) and do not vary significantly from observations of the WSM. The modeled stress magnitudes in the Coso Geothermal Field match actual measures. The addition of the GPS loading provides a result set which is consistent for both stresses and displacements.

Based on the good fit to the various calibration parameters the modeled state of stress is used for the stress dependent fluid flow-fracture networks analysis.

## 8. Fracture networks and fluid flow pathways for the Coso Geothermal Field

### 8.1. Introduction

The Coso Geothermal Field (CGF) in eastern California produces up to 240MWe from fractured rocks. The efficiency of geothermal energy production at the CGF is reliant on the knowledge of fluid flow directions associated with fracture networks. Improved exploitation of the field is sought by gaining a better understanding of the fracture networks controlling the sub-surface fluid flow.

As a consequence of both large and small scale tectonic processes, the in-situ 3D state of stress defines tectonic regimes, determines the seismically most active and hazardous regions and gives indications on crucial fault parameters. In a reservoir, both hydrocarbon and geothermal, information on the 3D state of stress is essential to optimize drilling, production and stability. Furthermore, crucial parameters such as the likelihood of fracture generation, fracture orientation, fluid pathways, optimal drilling direction and reservoir pressure are directly dependent on the 3D state of stress.

The most important factor for fluid migration in the crust is the topography of the water table (Price, 1985). However, fluid flow may also occur associated with fluid pressure variations due to tectonic loading (e.g. Oliver, 1986; Sibson, 1990). In particular, it has been pointed out that the mean stress can be used as a proxy for the hydraulic head and thus be modeled as a driving force for fluid flow (e.g. Connolly and Cosgrove, 1999; Zhang et al., 2002). Mean stress gradient vectors are used to indicate probable first order fluid flow directions and, when combined with the distribution of predicted second order fractures, allow prediction of more local scale fluid flow networks (Connolly and Cosgrove, 1999). Recent studies have shown that faults favorably oriented for slip in the stress field tend to be the most active flow pathways (Barton et al., 1995; Finkbeiner et al., 1997).

In this study a multi-scale 3D finite element (FE) analysis approach is used to establish a mechanical model of the CGF in the Coso Range that is consistent in stress orientation and tectonic regimes with independent data. The Coso Range has recently been interpreted as being situated within a releasing bend structure that transfers dextral slip from the Airport Lake Fault Zone (ALFZ) to the Owens Valley Fault (OVF; Unruh et al., 2002). In such transtensional bends second order faulting is a key control on fluid flow (Connolly and Cosgrove, 1999). The modeled 3D state of stress is used to derive the distribution and likelihood of second order fractures and to investigate how the second order faulting corresponds to mean stress derived fluid flow pathways. It is important to note that the modeled state of stress is solely dependent on the application of gravity and the tectonic loading. Mean stress perturbations due to withdrawal of fluids since the beginning of production in the Coso Geothermal Field are neglected and thus the modeled state of stress represents conditions prior to the beginning of production at Coso.

### 8.2. Fracture networks

The type of fractures generated is critical in understanding fluid flow in the CGF and, therefore, a distinction between tensile and shear fractures must be made during the

analysis of the FE results. The likelihood of fracture generation due to the local stress state must also be considered. The concept of fracture potential (FP; Connolly, 1996) enables both of these distinctions to be made and is utilized herein (see chapter 2).

The model derived differential, mean and orientations of stress are used to calculate sFP data within the model assuming a bulk rheology approximating brittle failure of rock. Idealized rheologies are chosen to simulate igneous rocks, with cohesion ( $C_0$ ; assumed to be twice the tensile strength (Price and Cosgrove, 1990) and the coefficient of internal friction,  $\mu$ . Values of 10MPa and 20MPa for the cohesive strength and 0.4 and 0.6 for its frictional strength are chosen. The cohesion of 10-20MPa is significantly lower than the cohesive strength of 48.5MPa presented by Davatzes and Hickman (2006) for intact Coso rocks. Thus a combination of  $C_0=10\text{ MPa}$  and  $\mu=0.4$  and of  $C_0=20\text{ MPa}$  and  $\mu=0.6$  mimics pre-fractured rock volumes. The FP distribution is investigated at reference depths of  $z=0\text{ m}$  and  $z=-1000\text{ m}$ . Predicted fracture orientations relate to the stress tensor as follows: tensile fractures are orientated normal to the local minimum principal stress and shear fractures at  $45 \pm \tan^{-1} \mu$  to the maximum principal stress.

### 8.3. Fracture Potential (FP) in the Coso Range

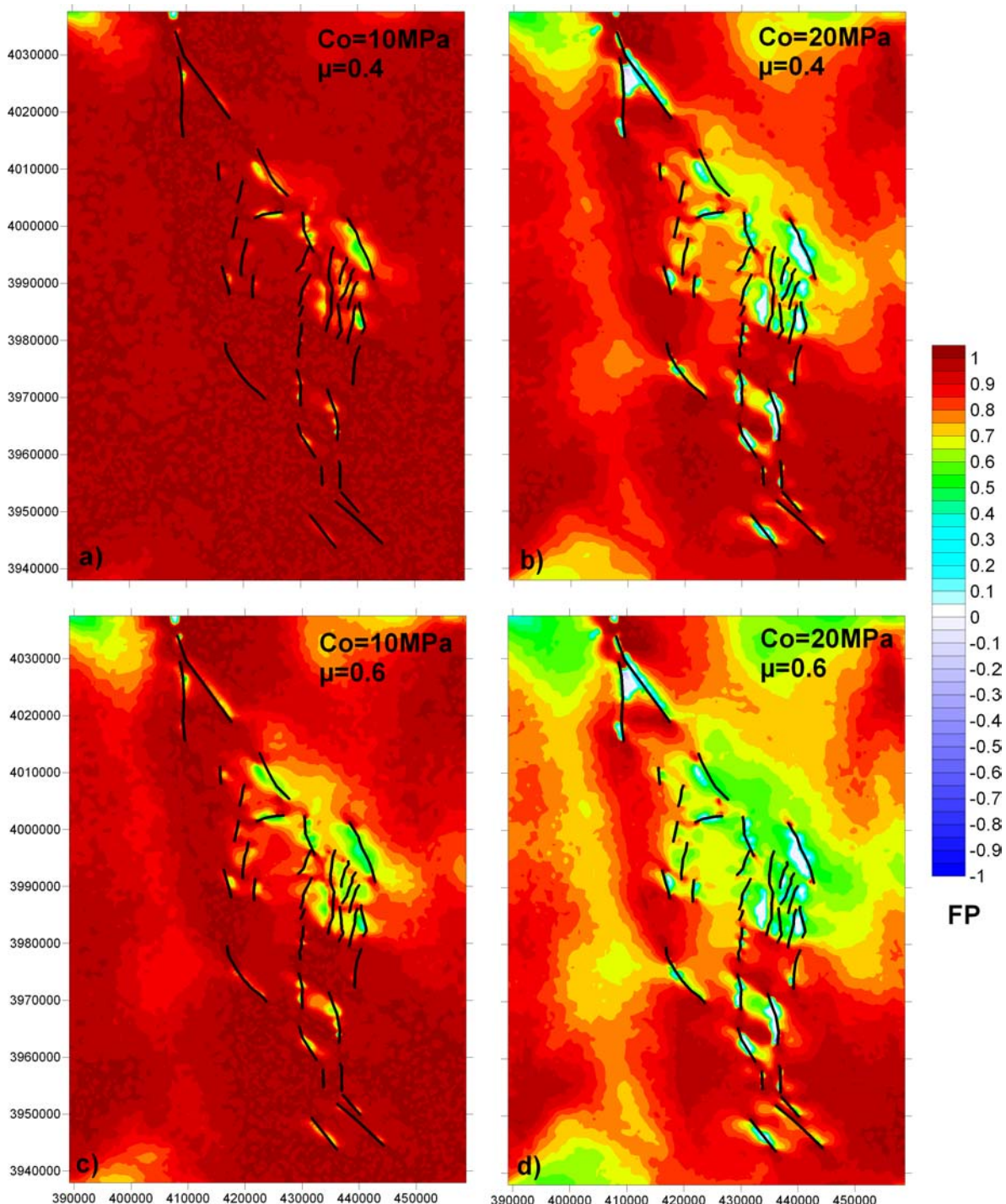
At the investigation depth of  $z=-1000\text{ m}$  the modeling results suggest that only shear fractures are likely to be generated, i.e.  $\text{FP}>0$ . Closer to surface local regions of tensile fracturing are predicted. The subsequent analysis is restricted to the  $z=0\text{ m}$  and  $z=-1000\text{ m}$  level since these represent typical production depths in the CGF.

At  $z=0\text{ m}$  (Figure 8.1) the distribution of shear FP (sFP) indicates a high likelihood of shear fracturing throughout the Coso Range. This is especially evident for the parameter sets of  $C_0=10\text{ MPa}$ ,  $\mu=0.4$  and for  $C_0=10\text{ MPa}$ ,  $\mu=0.6$  (Figure 8.1a,c) where the sFP is 1 in most regions of the Coso Range. Using a higher cohesion of 20MPa (Figure 8.1b,d) the distribution of sFP indicates a high likelihood of shear fracturing west and south of the Coso Range with peaks of FP in the vicinity of the Little Lake Fault (LLF), in the northern ALFZ and in the Indian Wells Valley. The CGF is situated in a region of relatively reduced sFP. At  $z=-1000\text{ m}$  the sFP for all parameter sets is lower than at  $z=0\text{ m}$  (Figure 8.2) but the sFP peaks remain the same as for the  $z=0\text{ m}$  level.

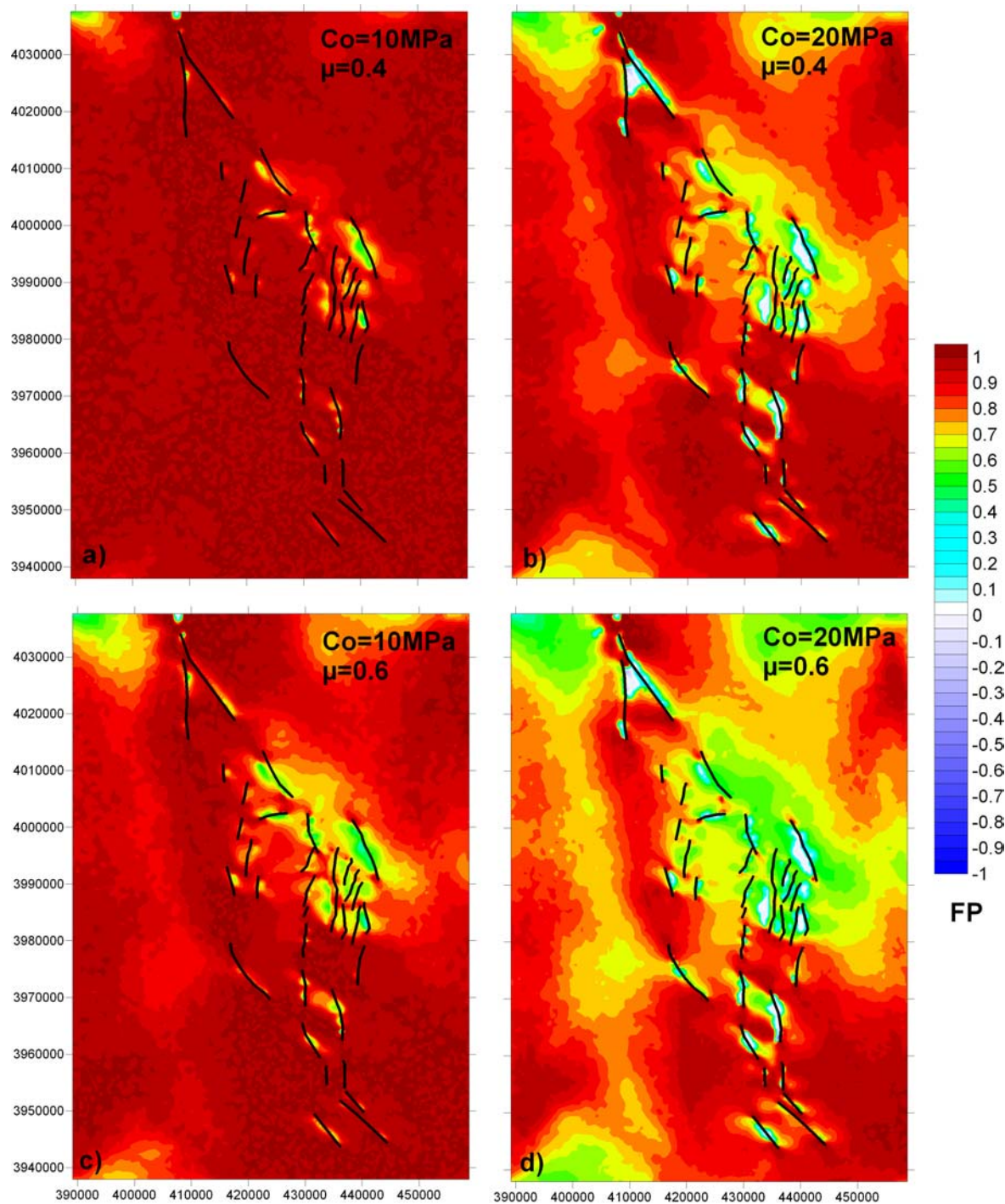
The parameter set of  $C_0=10\text{ MPa}$ ,  $\mu=0.4$  for both depths generally generates a sFP that is higher than expected since it predicts the whole Coso Range and adjacent regions to fail in shear. This is not indicated by the regional seismicity distribution (Figure 8.3). Furthermore, the parameter set of  $C_0=10\text{ MPa}$ ,  $\mu=0.6$  generates a sFP which predicts failure inconsistent to the seismicity. Therefore the parameter sets with cohesion of  $C_0=20\text{ MPa}$  provide the best estimate for the rock rheology in the CGF.

Figure 8.4 illustrates the sFP peaks (of  $C_0=20\text{ MPa}$ ,  $\mu=0.4$ ) and the regional seismicity. It can be seen that the FP maxima coincide with seismicity clusters in the ALFZ, south of the Wild Horse Mesa and in the Rose Valley. The dense clusters in the vicinity of the CGF are not reproduced by the modeled state of stress and the CGF is situated in a region of relatively reduced FP. Note however that active fracturing in the CGF is indicated by shallow seismicity, which Feng and Lees (1998) argue is associated with fluid injection and circulation. The modeling results are consistent with the model of

Bhattacharyya and Lees (2002) who infer that the LLF and the ALFZ are the most significant seismogenic zones/areas of seismicity in the vicinity of the CGF. East of the Coso Range the sFP significantly decreases, indicating that the regional tectonics (releasing bend) dominates the system.



**Figure 8.1: Fracture Potential (FP) for the Coso Range at  $z=0\text{m}$  for various idealized rock rheologies. Only shear failure is predicted. A cohesion of 10MPa seems too low since the whole Coso Range and adjacent regions are predicted to fail in shear.**



**Figure 8.2: Fracture Potential (FP) for the Coso Range at  $z = -1000\text{m}$  for various idealized rock rheologies.**

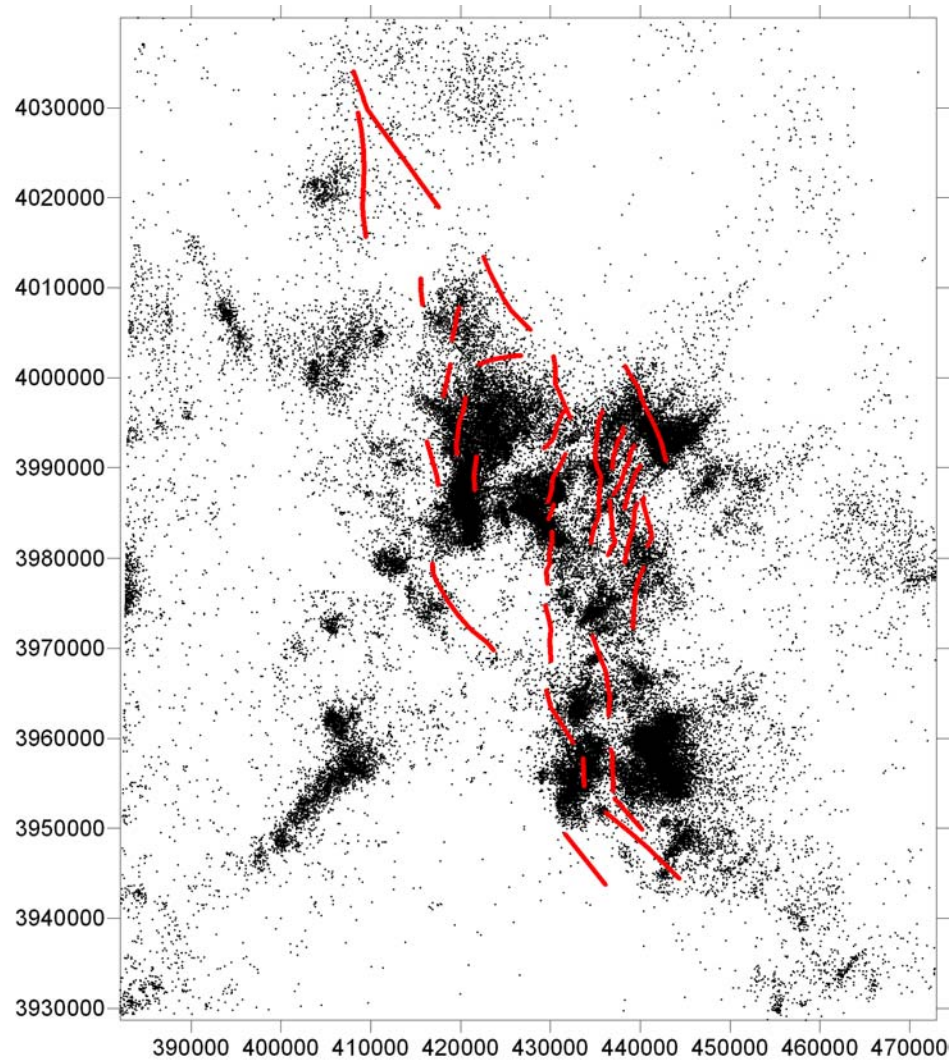


**Figure 8.3: Regional seismicity of the Coso Range and modeled faults. Peaks of seismicity occur in the ALFZ, in the vicinity of the CGF and in the northern Coso Range.**

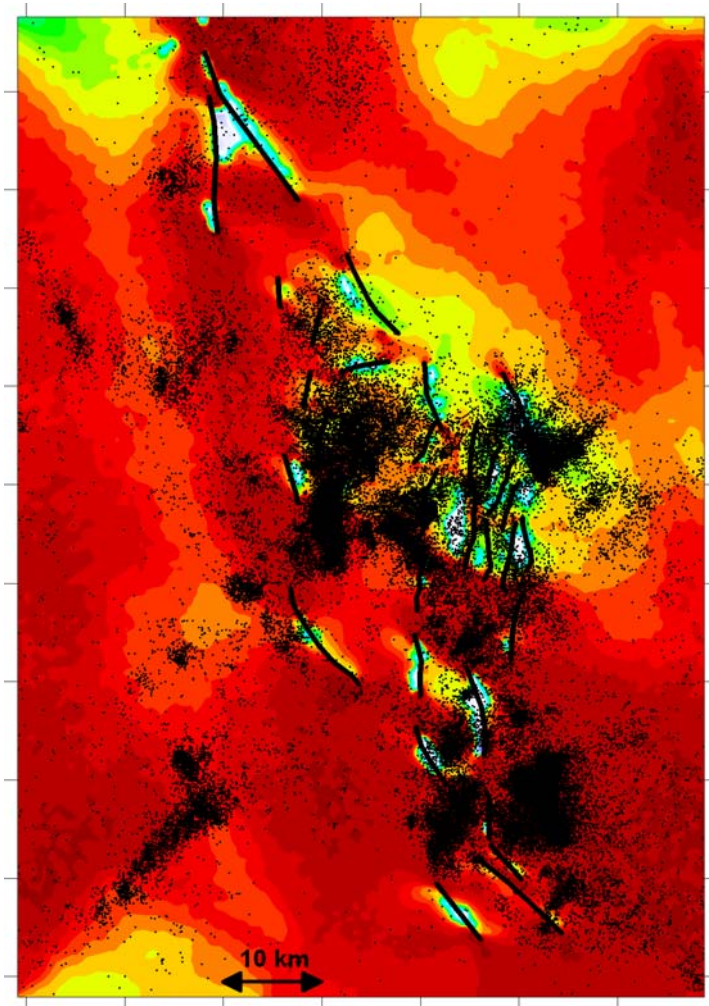


**Figure 8.4:** FP for  $C_0=20\text{ MPa}$ ,  $\mu=0.4$  at  $z=0\text{ m}$  and regional seismicity. The FP maxima coincide with seismicity clusters in the ALFZ, south of the Wild Horse Mesa and in the Rose Valley. The dense clusters associated by fluid injection and production in the CGF are not matched.

#### 8.4. Second order structures

Cenozoic faulting is widespread in the Coso Range and has been mapped by Duffield and Bacon (1980) and Whitmarsh (1998; Figure 8.5). Generally, two sets of faults are observed in the Coso Range. High angle ( $60^\circ$ - $70^\circ$ ) faults striking between  $N15^\circ E$  and  $N25^\circ E$  are common throughout the Coso Range and generally exhibit extensional displacement with a varying dextral component. WNW to NW trending faults bound the south side of the Coso Range and are generally well developed within the southern and western parts of the range. Table 8.1 lists the orientations of most mapped structures for several regions of the Coso Range.

Corresponding to the concept of Fracture Potential (FP) a shear FP (sFP) of 1 indicates the generation of a “new” second order fracture. The orientations of these 2<sup>nd</sup> order structures become of particular interest since, if dilatant, they are a major factor in the fluid flow field. Figure 8.6 illustrate syn – and antithetic pseudo shear fractures generated at locations of high FP in the Coso Range. The predicted 2<sup>nd</sup> order structures are compared to mapped structures in Table 8.1 for depths of  $z=0\text{ m}$  and  $z=-1000\text{ m}$ . Green

color coding indicates a good correlation between 2<sup>nd</sup> order structures predicted by the models and mapped structures. Yellow color represents fair agreement and red color a poor correlation.

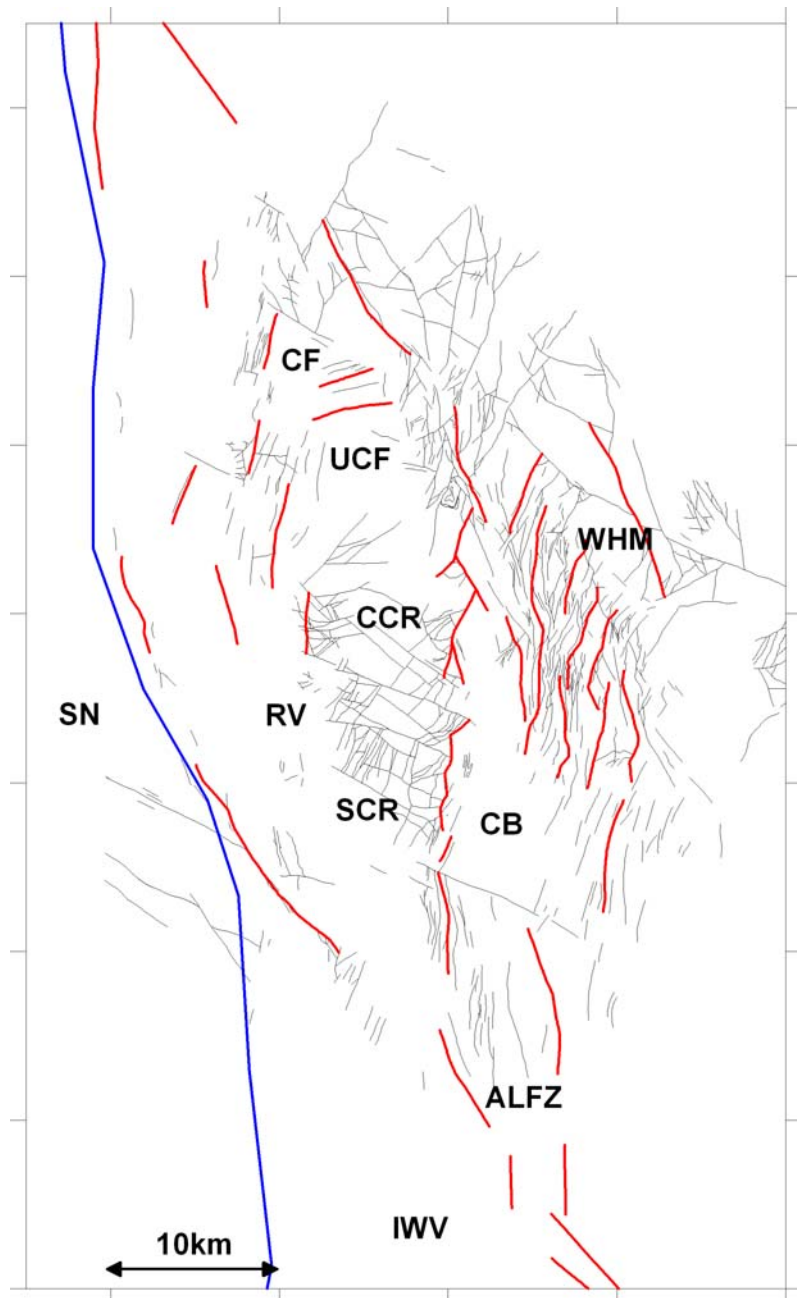


**Figure 8.5: Faults of the Coso Range.** Red lines indicate faults included in the model, blue line represents the SN outline. IWV=SN=Sierra Nevada, Indian Wells Valley, ALFZ=Airport Lake Fault Zone, CB=Coso Basin, RV=Rose Valley, SCR=southern Coso Range, CCR=central Coso Range, WHM=Wild Horse Mesa, UCF=Upper Cactus Flat, CF=Cactus Flat.

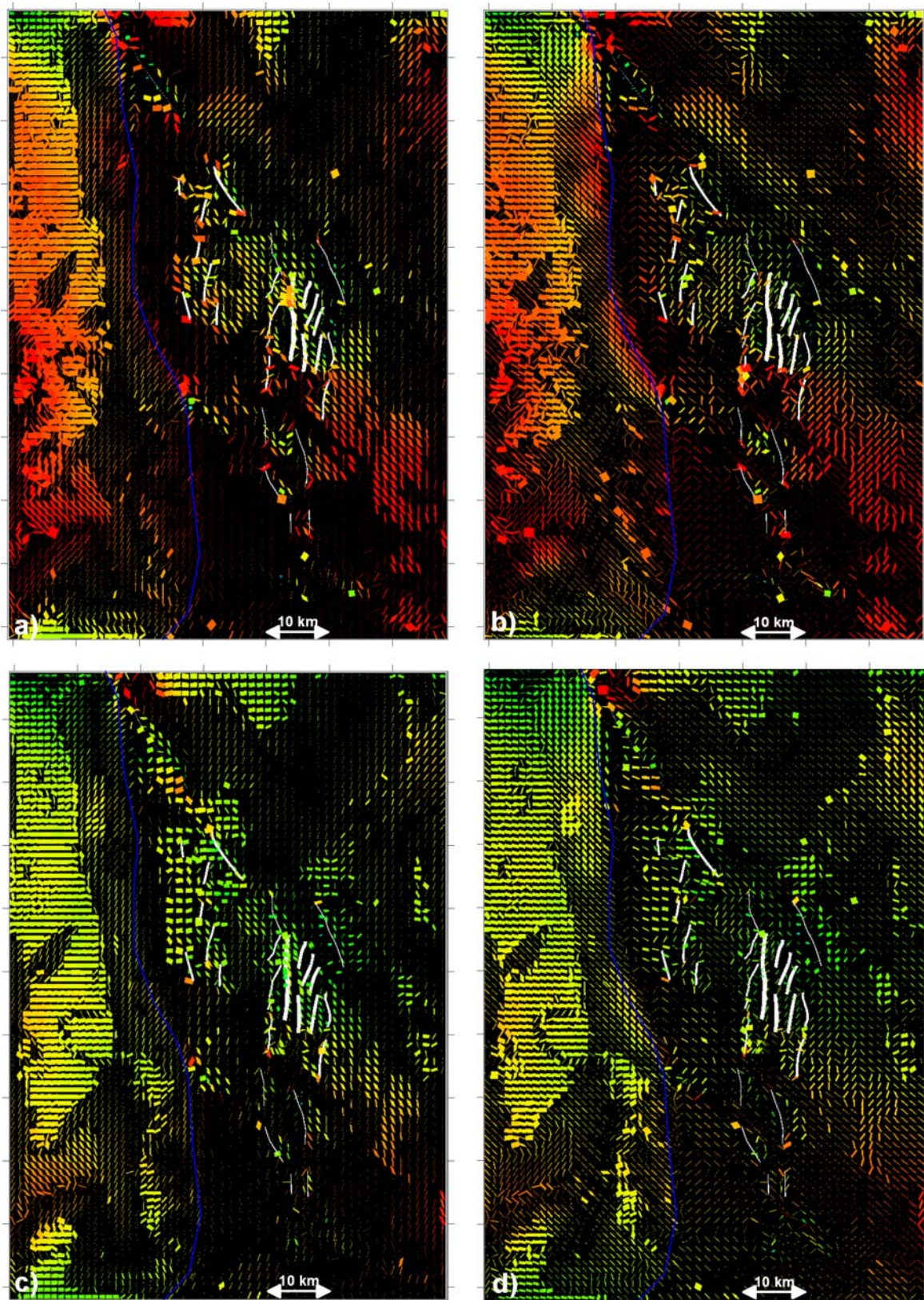


**Figure 8.6:** Predicted 2nd order fractures for the Coso Range. a) synthetic shears at  $z=0\text{m}$ , b) antithetic shears at  $z=0\text{m}$ , c) synthetic shears at  $z=-1000\text{m}$ , d) antithetic shears at  $z=-1000\text{m}$ . Description of orientations in Table 8.1.

Region	Orientation of mapped structures			Model results at z=0m			
				synthetic shears		antithetic shears	
ALFZ	N-S	N10°E	NNW-SSE	N15°E-N15°W		NW-SE	NE-SW
IWV	NW-SE	N-S		NNW-SSE		NE-SW	
RV	N10°E	N15°E		N15°E		NW-SE	
CB	NNE-SSW	N15°E-N25°E		N10°E		NW-SE	NNE-SSW
SCR	NNE-SSW	NW-SE	WNW-ESE	N15°E		NW-SE	NNE-SSW
CCR	NNE-SSW	NW-SE	WNW-ESE	N15°E	NW-SE	NW-SE	NNE-SSW
WHM	N-S	N15°E	NNW-SSE	NW-SE	NNW-SSE	NNE-SSW	NNW-SSE
UCF	N15°E	E-W		NW-SE	N15°E	NW-SE	NE-SW
CF	N15°E	E-W		NNW-SSE	N15°E	NNE-SSW	NW-SE

Region	Orientation of mapped structures			Model results at z=-1000m			
				synthetic shears		antithetic shears	
ALFZ	N-S	N10°E	NNW-SSE	N15°E-N15°W		NW-SE	NNE-SSW
IWV	NW-SE	N-S		NNW-SSE		NE-SW	NW-SE
RV	N10°E	N15°E		N15°E		NW-SE	
CB	NNE-SSW	N15°E-N25°E		N10°E		NW-SE	NNE-SSW
SCR	NNE-SSW	NW-SE	WNW-ESE	N15°E		NW-SE	NNE-SSW
CCR	NNE-SSW	NW-SE	WNW-ESE	N15°E		NW-SE	NNE-SSW
WHM	N-S	N15°E	NNW-SSE	NNW-SSE		NNE-SSW	
UCF	N15°E	E-W		NW-SE	N15°E	NW-SE	NE-SW
CF	N15°E	E-W		E-W	NW-SE	E-W	NNE-SSW



good agreement between model results and mapped faults (diff.<10°)

fair agreement between model results and mapped faults (10°<diff.<20°)

poor agreement between model results and mapped faults (diff.>20°)

**Table 8.1: Comparison of predicted 2nd order fractures at z=0m and z=-1000m to mapped faults in the Coso Range. The color code indicates the quality of correlation. At each location at least one set of predicted shears agrees well with orientations of mapped structures. Only in the IWV and the ALFZ fair correlations are observed.**

In general, predicted 2<sup>nd</sup> order fractures at both depths provide a good fit to mapped structures. At each location at least one set of predicted shears agrees well, i.e. the difference in orientation is less than 10°, with orientations of mapped structures. Only in the Indian Wells Valley (IWV) and in the ALFZ fair correlations are observed.

At z=-1000m the orientations of the 2<sup>nd</sup> order structures in most model regions are very similar to those at 0m. Exceptions occur in the IVW, where NW-SE orientations consistent with mapped faults are present at z=-1000m, and in the vicinity of Cactus Flat (CF), where E-W oriented faults relate to predicted shears.

The predicted 2<sup>nd</sup> order structures provide a good fit in the central Coso Range and in the southern Coso Range where both sets match observed structures. In general, the modeled state of stress predicts 2<sup>nd</sup> order fracture orientations which match the strike of most mapped structures.

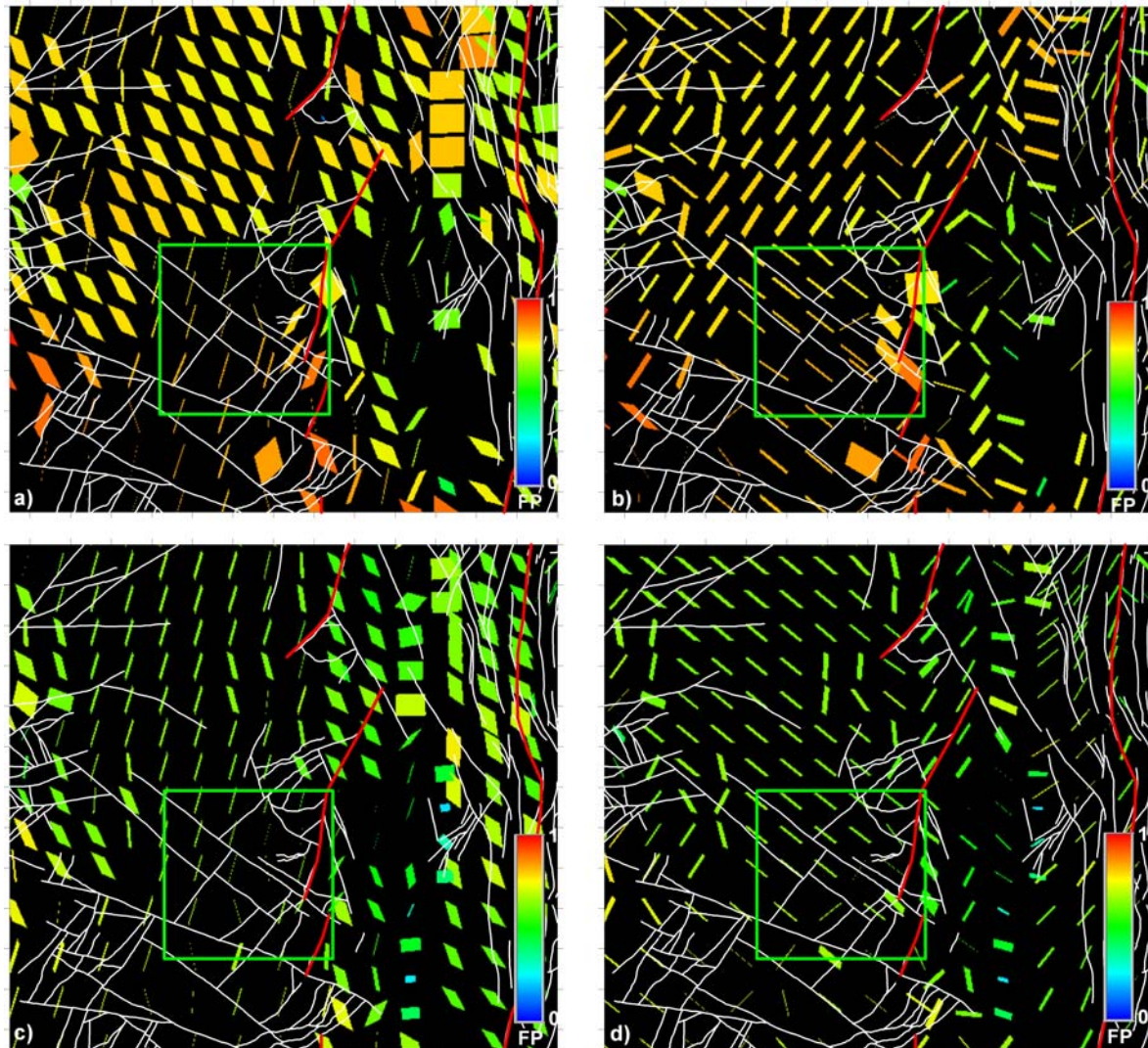


**Figure 8.7: Predicted 2nd order synthetic and antithetic shear fractures for depths of  $z=0\text{m}$  (a,b) and  $z=-1000\text{m}$  (c,d).** Fractures are color scaled with the corresponding sFP. In the vicinity of the CGF (green box) synthetic shears oriented  $\sim\text{N}10^\circ\text{E} - \text{N}20^\circ\text{E}$  closely align with mapped structures (white lines) oriented NNE-SSW or NE-SW and antithetic shears closely align to mapped NW-SE structures.

A more detailed fracture orientation analysis is performed for the CGF location at depths of  $z=0\text{m}$  (Figure 8.7a,b) and  $z=-1000\text{m}$  (Figure 8.7c,d). Here, the second order fractures are color-scaled with the corresponding sFP magnitude (Figure 8.7).

For  $z=0\text{m}$  synthetic shear fractures are oriented  $\text{N}10^\circ\text{E}-\text{N}20^\circ\text{E}$  within the CGF and  $\sim\text{NNW-SSE}$  north of it. Antithetic shear fractures are oriented NW-SE within the CGF and NE-SW north of it. At  $z=-1000\text{m}$  the sets of predicted shears show a more uniform orientation. Synthetic shears have an orientation of  $\sim\text{N}10^\circ\text{E} - \text{N}20^\circ\text{E}$  both within the CGF

and north of it, and antithetic shears are oriented NW-SE, with only some fractures NW-SE within the CGF. In general, the sets of predicted 2<sup>nd</sup> order shears closely correspond to mapped sets of NNE-SSW, NE-SW or NW-SE oriented structures in the vicinity of the CGF. The sFP of the predicted fractures at z=0m is in the range of 0.7-0.8 indicating high likelihood of active faulting. It should be noted that the highest sFP magnitudes occur in the southeastern part of the CGF near the southern tip of the CWF. The sFP for z=-1000m is slightly lower, i.e. 0.6-0.7 also with higher magnitudes in the southern part of the CGF.

### 8.5. Discussion of fracture analysis

The modeled state of stress generates second order structures that, especially in the vicinity of the CGF, align with mapped faults. It is therefore very likely that the releasing bend fault structure of the Coso Range is influenced by the present state of stress and that active fracturing is driven by contemporary tectonic boundary forces. It should be noted that 2<sup>nd</sup> order fractures predicted by the sFP method are inherently optimally oriented. Thus the close alignment of predicted and mapped structures may indicate that active fracturing in the Coso Range reflects fault reactivation processes rather than fracturing intact rock.

Additional active faulting/fracturing associated with production processes in the CGF are not considered since the production history has not been modeled. However, these processes might elevate the present differential stresses and/or reduce the mean effective stress and thus increase the FP in the Coso Range. This would be consistent with the regional distribution of seismicity in the CGF which mostly reflects production induced events.

### 8.6. Mean stress derived fluid flow networks for the Coso Geothermal Field

The following analysis of the interaction between fluid flow and fractures assumes that fluid migration is directly related to the mean stress magnitude such that fluids will flow from regions of high mean stress to regions of low mean stress, as indicated by vectors of the mean stress gradient (e.g. Connolly and Cosgrove, 1999; Zhang et al., 2002). This approach is reasonable for analyzing the first order fluid flow pathways since mean stress represents the isotropic part of the stress tensor and is hence an indicator of pressure. This analysis considers mean stresses that do not account for pressure reductions due to fluid withdrawal and hence represents a state of stress before the beginning of production and injection operations at the Coso Geothermal Field (CGF). Further implicit assumptions are that all fluids in the system are connected and that the hydraulic head is directly proportional to the calculated mean stress. Since it is impossible to illustrate the 3 dimensional directions of the vectors the mean stress distribution and the derived fluid flow vectors are presented at depths of z=500m, 0m, -1000m and -2000m. In order to infer first order (regional) flow directions (arrows in Figure 8.8) the Coso Range mean stress distribution at z=-1000m is analyzed.

The FE results predict that the CGF is surrounded by high mean stress regions in the northwest, the north and the west. South of the Coso Range a dominant low in the Indian Wells Valley exists. The high precipitation in the western Sierra Nevada results in

this area being the regional source of fluids for the Coso Range. More local flow directions indicate N-S flow from the northern Coso Range to the Indian Wells Valley.

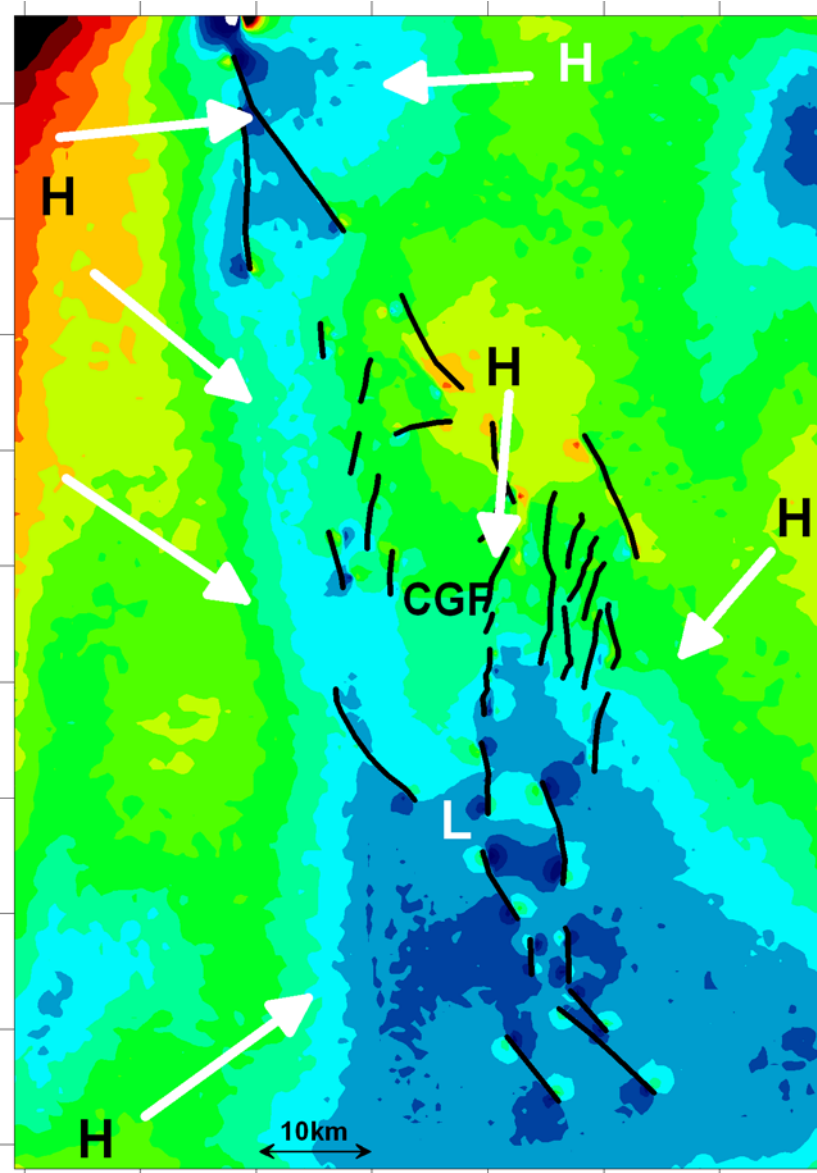


**Figure 8.8: Regional mean stress derived fluid flow pattern for the Coso Range. Fluids migrate from high mean stress (H) to low mean stress (L).**

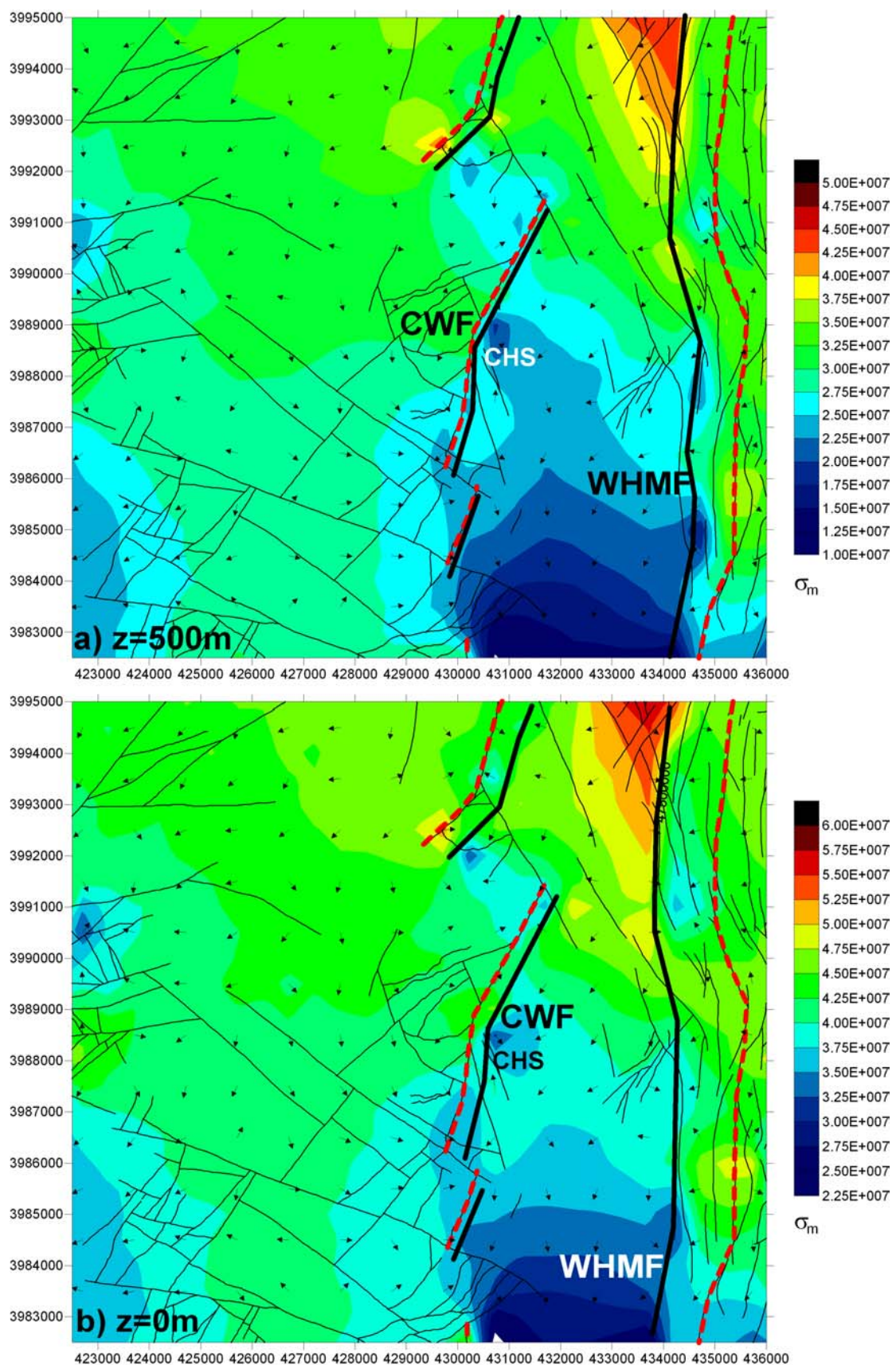


**Figure 8.9: Fluid flow vectors for  $z=500\text{m}$  and  $z=0\text{m}$ . Red=modeled faults at surface, thick black lines=modeled faults at depth, grey=mapped faults, CWF=Coso Wash Fault, CHS=Coso Hot Springs, WHMF=Wild Horse Mesa Fault.**

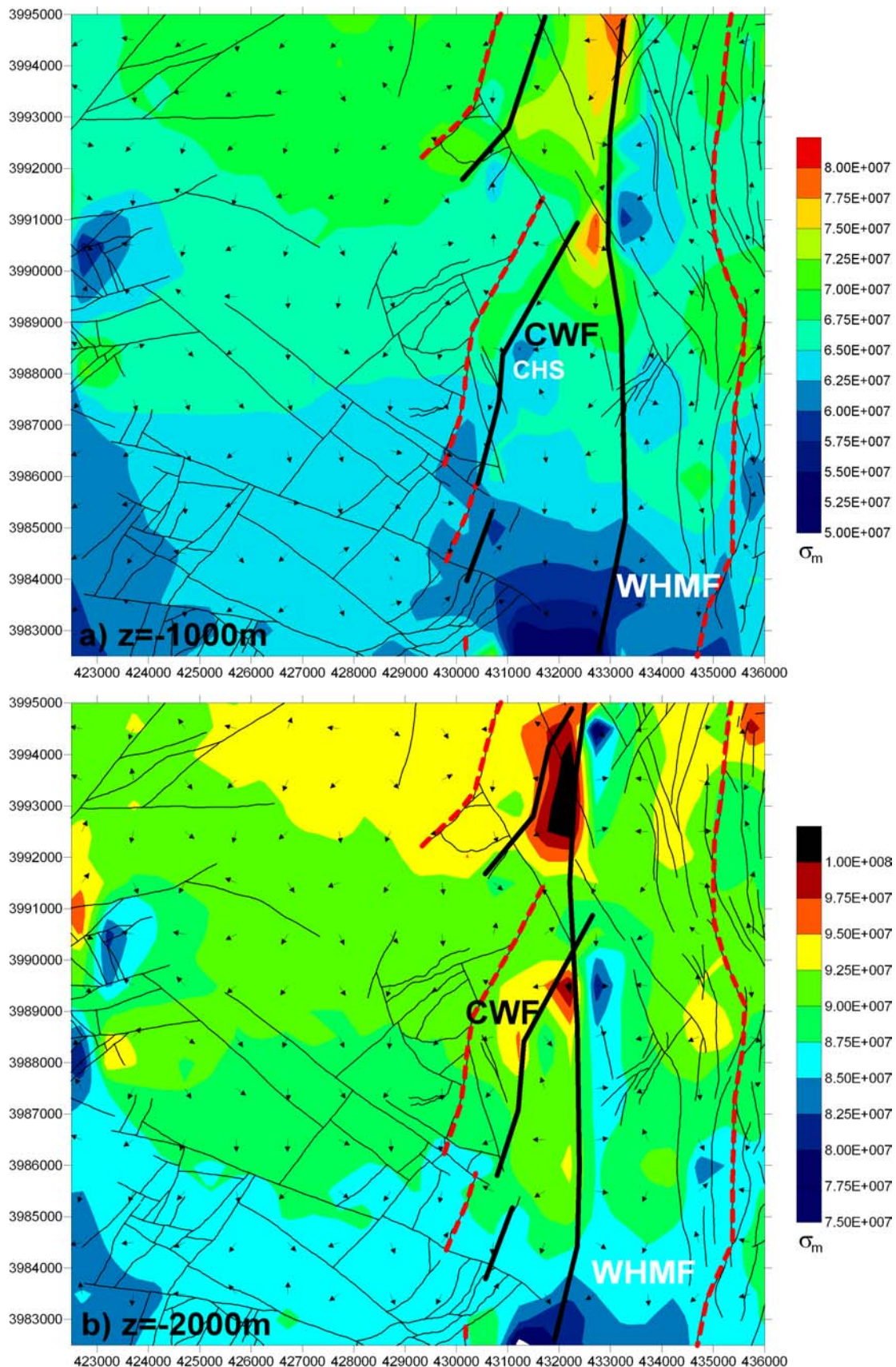


**Figure 8.10:** Fluid flow vectors for  $z = -1000\text{m}$  and  $z = -2000\text{m}$ . Red=modeled faults at surface, thick black lines=modeled faults at depth, grey=mapped faults, CWF=Coso Wash Fault, CHS=Coso Hot Springs, WHMF=Wild Horse Mesa Fault.

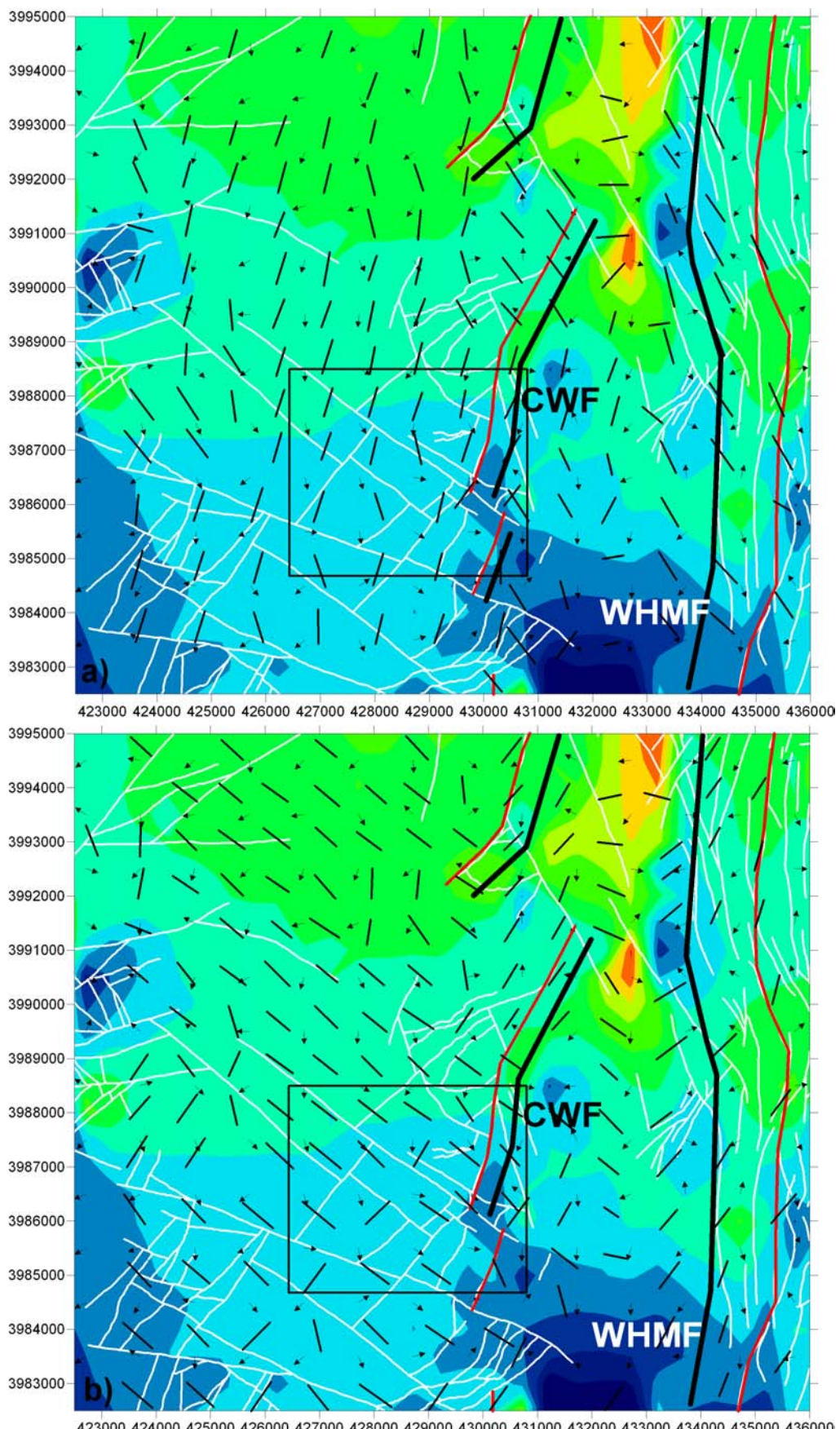


**Figure 8.11: synthetic shears (a) (grey ticks) and (b) antithetic shears (grey ticks) at  $z=0\text{m}$ . Vectors are fluid directions and thin white lines mapped 2<sup>nd</sup> order structures.**

At the local scale, significant variations in the predicted fluid flow pathways are present. These local fluid flow vectors are shown for the region of the CGF (Figures 8.9, 8.10). For all depths considered a general flow of fluids into the main production area from the north and northwest can be observed. In the western part of the CGF mean stress vectors rotate to trend from N-S to NW-SE or W-E. Closer to surface (at  $z=500\text{m}$  and  $z=0\text{m}$ ) the vectors are more W-E and finally driven towards a mean stress low at the southern tip of the Coso Wash Fault (CWF) in the region of the CGF East Flank. This mean stress low can be observed at depths of  $z=0$  and  $z=-1000\text{m}$  and is likely to be a sink for fluids in all directions. At  $z=500\text{m}$  and  $z=-2000\text{m}$  this low is less pronounced, since a dominant low in the Coso Basin at  $z=500\text{m}$  overprints it, and at  $z=-2000\text{m}$  compression caused by the intersection of the Coso Wash Fault (CWF) and the Wild Horse Mesa Fault (WHMF) reduces the mean stress gradient. Furthermore, at  $z=500\text{m}$ ,  $z=0\text{m}$  and  $z=-1000\text{m}$  another closed mean stress low exists at the location of Coso Hot Springs (CHS). This “low” is located at a kink in the CWF clearly demonstrating that fault geometry has a significant influence on the mean stress distribution.

Northeast and east of the CGF, fluids are focused between the CWF and the WHMF and driven N-S from a mean stress high in the northern Coso Range to the mean stress low in the Coso Basin. Close to the CWF these fluids are attracted by the mean stress lows at CHS and the CWF and migrate towards the CGF. At  $z=-2000\text{m}$  the CWF and the WHMF intersect at depth and the compression imposed drives fluids E-W into the CGF. Hence there is also a potential for fluids from the E to reach the CGF.

In the northeast of the CGF a closed mean stress low (for  $z=500\text{m}$ ,  $z=0\text{m}$  and  $z=-1000\text{m}$ ) at the northern tip of the CWF might act as an additional fluid accumulation site, possibly preventing fluids from this region entering the current area of the CGF.

### 8.7. 2<sup>nd</sup> order fractures and fluid flow

In order to infer integrated fracture/fluid flow pathways the fluid flow vectors are also compared to the strike of predicted and mapped 2<sup>nd</sup> order faults. This analysis is conducted at a depth of  $z=-1000\text{m}$  since the orientations for the syn- and antithetic shears are more uniform than at  $z=0\text{m}$  (Figure 8.11).

The second order structures in the CGF generally enhance the flow directions inferred from the mean stress field. Mapped and predicted antithetic shears are oriented NW-SE enhancing permeability ( $k$ ) towards the Coso Wash Fault. This zone is favorably situated to accumulate fluids (i.e. mean stress low) and is coincident with the location of the present East Flank expansion of the CGF. Predicted synthetic shears are oriented  $\sim N10^\circ E$  and might transport fluids from the north until the set of NW-SE faults is reached. Within the CGF this set of fractures is likely to impede fluid migration by enhancing permeability ( $k$ ) parallel to their strike. After coalescing into high  $k$  lineaments the fluids will get focused into locations along mapped structures. Thus, fluid flow is expected to be locally redirected until reaching the mapped faults. Note that this assumes, not unreasonably given the level of shallow seismicity in the ECSZ, that the mapped faults are leaking over a hydrologically significant time 1-10's/100's of years.

North of the CGF, along the Coso Wash Fault, a mean stress low attracts fluids from the NE and NW and might prevent that fluids adjacent to this region reaching the CGF. However, predicted 2<sup>nd</sup> order structures east of this mean stress low are at high angle to the flow directions impeding fluid migration and possibly preventing fluids from the north reaching this site. Rather the northern derived fluids maybe transferred southwards into the CGF.

### 8.8. Discussion and conclusions

The numerical modeling generated a calibrated 3D state of stress for the Coso transtensional bend setting which is consistent with independent data for the orientation of S<sub>H</sub> and observed transtensional tectonic regimes. The derived likelihood of second order fracture generation (FP) shows that the Coso releasing bend is a region of active fracturing corresponding to tectonic boundary forces. The most active regions are south and west of the Coso Range. The CGF is situated in a zone of tectonically reduced sFP. This is consistent with observations of regional seismicity in the Airport Lake Fault Zone and the Indian Wells Valley region (Bhattacharyya and Lees, 2002) and with local seismicity in the Coso Range associated to fluid injection (Feng and Lees, 1998). Predicted 2<sup>nd</sup> order shear fractures closely align with mapped structures of the Coso Range (Whitmarsh, 1998). This probably indicates that active fracturing processes in the Coso Range reflect fault reactivation and/or elongation processes. This conclusion is consistent with observations by Taylor and Dewey (2006) who argued that regional transtension in the Coso Range is accommodated by strain partitioning and kinematic reactivation of existing structures.

Additional active faulting/fracturing associated to production processes in the CGF are not reproduced since the production history has not been modeled. It should also be noted that the FP analysis is based on a state of stress which does not account for pore fluid pressure and thus effective stresses. Effective stresses will reduce the mean stress whilst maintaining differential stress (Price and Cosgrove, 1990) thus increases the shear FP (sFP).

The modeled mean stress is used to derive fluid flow directions at the CGF. In combination with the orientations of predicted second order fractures a combined fluid flow-fracture network is inferred for the CGF. It is important to note that the derived fluid flow directions in this study are only dependent on mean stress variations due to gravitational potential energy differences and tectonic loading. Furthermore, fluids are modeled to be redirected to flow parallel to first and second order fractures. Intrinsic permeability, thermal processes and the feedback of fracture permeability on transient and static pore fluid pressure affecting fluid migration are not considered.

The mean stress distribution for the Coso Range and the Geothermal Field indicates regional fluid flow from the west (Sierra Nevada) and the northern Coso Range to the south into the IWV. In the area of the CGF fluids migrate from the north into the system and then flow south-eastwards to the Coso Wash Fault (CWF). Here, west of the southern tip of the CWF, a closed mean stress low attracts fluids from all directions. This region of low mean stress coincides with the area of the recent East Flank expansion of the CGF. The fluid directions derived in this study are reasonably consistent with porosity derived

permeabilities by Lees and Wu (2000), who observe eastward flow in the southern CGF. This coincides with the predicted NW-SE (for  $z=-1000\text{m}$  and  $z=-2000\text{m}$ ) to W-E (for  $z=500\text{m}$  and  $z=0\text{m}$ ) flow directions in the western and southern part of the CGF.

In contrast to this study, Lees and Wu (2000) predict fluid flow to be S→N in the northern part of the field, but state that N→S flow is observed in the CGF. Both options are considered reasonable/likely given the orientations of the mapped and predicted fractures. Unfortunately, analysis of the interaction of predicted second order structures with the fluid flow vectors does not provide a conclusive answer to this issue. As expected, some regions have 2<sup>nd</sup> order fractures that align with the fluid flow directions (e.g. close to the CWF) whilst others have predicted fractures that impede the optimal migration pathway (e.g. in the northern part of the CGF). In general, the mapped structures align with the predicted fluid flow pattern. The sub-mapable structures probably influence transit times by enhancing or retarding fluid flow rather than acting as fluid domain boundaries.

The loosely coupled analysis presented here indicates the importance of understanding the influence of second order fracture networks for fluid migration in tectonically active regions and suggests that future work with tighter integration of coupled continuum and discontinuum mechanics is necessary.

## 9. Synthesis and discussion of the thesis

### 9.1. Goal of the thesis

The objective of this research study was to investigate the 3D crustal state of stress in the Western United States (WUS) and to infer its implications on the San Andreas Fault (SAF), Eastern California Shear Zone (ECSZ) tectonics and fracture networks and fluid flow interaction in the Coso Range. Since the state of stress in the WUS is the result of the complex interaction between tectonic boundary forces, gravitational potential energy differences ( $\Delta GPE$ ), basal tractions (which are neglected in this study) and complex structural geometries, 3D finite element models have been used to simulate the complete 3D state of stress. The knowledge of the 3D state of stress is essential both for understanding geodynamic processes as well as for optimizing reservoir processes in geothermal systems. The purpose of this modeling study was two-fold:

- Develop a series of multi-scale FE models to simulate the full crustal stress tensor in the WUS. The models are applied to scales of the SAF, the ECSZ and the Coso Range.
- Use results of modeled 3D state of stress on the scale of the Coso Geothermal Field (CGF) in the ECSZ to analyze second order fracture networks and associated fluid flow pathways from tectonically induced mean and differential stress variations.

### 9.2. Numerical methodology

In this process a multi-scale modeling approach based on elastic material parameters has been developed that integrates large scale tectonic processes of the San Andreas Fault system to local, small scale processes of the ECSZ and the Coso Geothermal Field in the Coso Range (Figure 9.1). The ABAQUS™ submodeling technique provides a framework that enables to study the influence of plate-scale boundary conditions on local models of the ECSZ and the Coso Range. Thus, the ABAQUS submodel analysis technique applied over various scales is a useful method to model the state of stress acting in a local region like the Coso Range, where the local boundary conditions are difficult or impossible to distinguish. The importance/value of the submodeling technique becomes most evident when boundary conditions interpolating the contemporary GPS displacement field have been applied to the model of the ECSZ. These boundary conditions failed to generate sufficiently large horizontal stresses to result in strike-slip and transtensional tectonic regimes in the ECSZ.

Another important factor in simulating the present-day state of stress is the application of an initial gravitationally induced stress state that represents the long-term genesis of a geological volume. The so-called near surface horizontal stress paradox (Engelder, 1993), in which the horizontal stresses near surface become larger than the vertical ones, poses a significant problem in the 3D numerical modeling of in-situ stresses. To address these problems a loading procedure has been developed that yields initial in-situ stress conditions that equilibrate gravitationally induced stresses and which are consistent with the observations from in-situ stress measurements and analytical models

(Sheorey, 1994). In summary, the model loading procedure consists of the following steps: gravitational loading and tectonic loading. At scales of the ECSZ and the Coso Range an additional loading step accounting for contemporary GPS displacements has been applied. The additional step was necessary to generate realistic surface displacements for the Coso Range scale submodel, since the rather homogeneous SAF scale model does not resolve the strain partitioning occurring in the WUS.

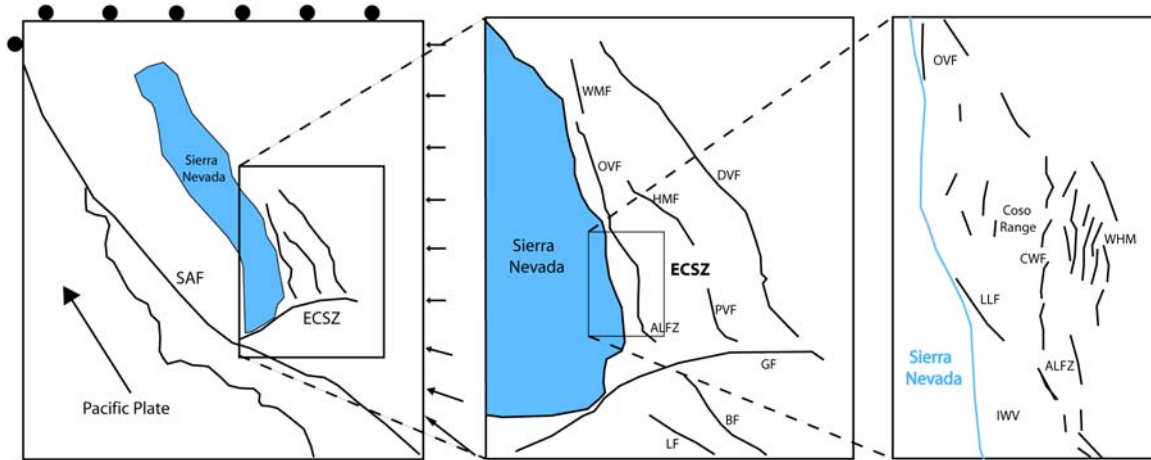


**Figure 9.1: Concept of the Abaqus submodeling procedure. Boundary conditions of the large scale model are transferred via the displacement results to the smaller scale models.**

### 9.3. Model calibration

Careful emphasis was placed on the calibration of the various model results to independent data and measurements. The FE results for all scales considered were calibrated against stress magnitudes, derived tectonic regimes and stress orientations (Figure 4.4 and 4.5 for the SAF scale; Figure 6.7-6.9 for the ECSZ scale and Figures 7.8-7.9 for the Coso scale). In order to establish a state of stress that sufficiently agrees with independent measurements it is again important to emphasize the significance of the pre-stressing procedure generating equilibrated, gravitationally induced stresses. This gravity induced state of stress is calibrated to Sheorey's model (1994), which observes horizontal stresses that become larger than the vertical stress component near surface. This is consistent to a compilation of world-wide stress magnitude data. If this approach was not followed a state of stress would result that significantly underestimates horizontal stress magnitudes, i.e.  $k=S_H/S_V=0.33$ , and that is not capable to reproduce the transition of strike-slip and extensional tectonic in the WUS.

In combination with the pre-stressing procedure based on the calibration to Sheorey's observations, it is possible to simulate the absolute state of stress and thus compare predicted stress magnitudes to observed stress measurements or estimations. This is a significant development and improvement in 3D numerical modeling approaches, since the modeled state of stress no longer represents only a relative state of stress. Rather, it closely matches the majority of published measurements for all the scales considered. Once the models matched all three parameters the results have been used for subsequent analysis.

## 9.4. Modeling results

In this section a short summary of the most important results of the various model scales is presented. The results presented are inferred from calibrated models against stress magnitudes and orientations from independent data.

### 9.4.1. SAF scale

The state of stress in the WUS at the scale of the SAF system can be explained by the combination of gravitational pre-stressing and tectonic loading. Topography induced gravitational potential energy differences ( $\Delta GPE$ ) in the gravitational pre-stressing (“gravity only”) model result in a dominant extensional tectonic regime with a large variability for the orientation of  $S_H$ . After the tectonic loading the following tectonic regimes are obtained (Figure 4.4a):

- (1) Strike-slip to transpression in central California adjacent to the SAF (0-200km).
- (2) A transition of transpression in the Big Bend area to strike-slip and transtensional regimes in the Mojave Block.
- (3) The ECSZ is transition zone of extension in the Basin and Range and strike-slip in the Mojave Block.
- (4) Extensional deformation in the Basin and Range.

The tectonic loading significantly influences the far-field state of stress in the Sierra Nevada, in the ECSZ and in the Basin and Range. The plate boundary forces result in distinct  $S_H$  orientations and transfer compressional stresses into the far-field. The bending geometry of the SAF is the main factor for generating these increased horizontal stresses and for transferring strike-slip deformation into the ECSZ. This becomes most evident when the difference in Regime-Stress-Ratio (RSR, see chapter 2.7) between the tectonic loading model and the gravity loading only model is considered (Figure 4.6). The tectonic loading results a region of increased compression, i.e. relatively increased horizontal stresses, imposed in the Mojave Block (0.5 - 1).

The strength of the SAF has been investigated by conducting a sensitivity analysis of the coefficient of friction,  $\mu$ , on the SAF. Generally, a strong fault ( $\mu=1.0$ ) should predict low angles ( $\beta$ ) of the maximum horizontal stress component,  $S_H$ , to the fault, and a weak fault ( $\mu=0.1$ ) should predict high angles of  $S_H$ . The FE results indicate that  $\mu$  has only a minor impact on  $S_H$  orientations. The difference between a weak fault scenario and a strong fault scenario is less than  $5^\circ$  in the far-field, i.e. for distances greater than 5 km from the fault, and in the range of  $0^\circ$ - $10^\circ$  on the fault surface. This leads to the assertion that  $S_H$  orientation data may not be an adequate approach for inferring the strength of the SAF. It is suggested that this insensitivity to the coefficient of friction is the main reason for the different interpretations and conclusions drawn from focal mechanism inversions.

### 9.4.2. ECSZ scale

The state of stress in the ECSZ is characterized by a transtensional tectonic regime. At shallow depths ( $>3000\text{m}$ ) the major active faults of the ECSZ are situated in corridors of pure strike-slip deformation (Figure 6.7). This shows the role of these faults in the

tectonic regime. The Owens Valley Fault, the Panamint Valley Fault and the Death Valley Fault accommodate dextral strike-slip whilst bulk deformation is accommodated by transtensional and extensional deformation between the fault sets. RSR distribution on the entire Airport Lake Fault Zone-Owens Valley Fault indicates that strike-slip regimes are most pronounced in the Owens Valley and that strike-slip deformation is possible for depths < 8km.

The distribution of the stress ratio R ( $0.8 > R > 0.5$ , Figure 6.14) suggests a consistent state of stress in the ECSZ regionally varied by topography. R maxima ( $R > 0.8$ ) are associated with topographic maxima. The major faults are situated in structural depressions and thus exhibit a greater influence of strike-slip loading. Thus, the scenario of a consistent regional stress field where slip is partitioned to account for the different deformation styles seems appropriate.

#### 9.4.3. Coso Range scale

The modeled state of stress in the area of the Coso Geothermal Field (CGF) is characterized by strike-slip tectonics near surface and transtensional tectonics with increasing depth (Figure 7.8 a,b). Obtained regions of slightly transpressional regimes are consistent with focal mechanism distributions in the Coso Range and adjacent regions (Bhattacharyya and Lees, 2002). A pure normal faulting regime for the East Flank of the CGF as inferred by Davatzes and Hickman (2006) is not supported by the modeling results which yield much higher  $S_H$  magnitudes than necessary for pure extensional faulting. Subsidence maxima (Figure 7.11) coinciding with the Coso Wash Fault (CWF) and Wild Horse Mesa Fault suggest that normal faulting is present in the Coso Range, but the state of stress is transtensional and faults also accommodate strike-slip deformation.

The analysis of the likelihood of second order fracture generation (FP) shows that the Coso releasing bend is a region of active fracturing corresponding to tectonic boundary forces. The most active regions are south and west of the Coso Range coinciding with the regional seismicity distribution (Figure 8.4). The close correlation of predicted 2<sup>nd</sup> order shear fractures with mapped structures of the Coso Range (Table 8.1; Figure 8.7; Whitmarsh, 1998) probably indicates that active fracturing processes in the Coso Range reflect fault reactivation.

The modeled mean stress is used to derive fluid flow directions at the Coso Geothermal Field (CGF). In combination with the orientations of predicted second order fractures a combined fluid flow-fracture network is inferred for the CGF. In the area of the CGF fluids migrate from the north into the system and then flow south-eastwards to the Coso Wash Fault (CWF). Here, west of the southern tip of the CWF, a closed mean stress low attracts fluids from all directions. This region of low mean stress coincides with the area of the recent East Flank expansion of the CGF. The analysis of the interaction of predicted second order structures with the fluid flow vectors does not provide a conclusive answer to this issue. As expected, some regions have 2<sup>nd</sup> order fractures that align with the fluid flow directions (e.g. close to the CWF) whilst others have predicted fractures that impede the optimal migration pathway (e.g. in the northern part of the CGF).

## 9.5. Discussion

When compared to previous numerical modeling studies of the WUS, the approach presented in this thesis shows significant improvements since it successfully numerically models the absolute crustal state of stress at a range of scales. Due to the large number of modeling studies of the WUS state of stress this discussion is restricted to those that used very similar approaches or are directly relevant to it.

### 9.5.1. SAF and ECSZ scale

2D modeling studies of the WUS tectonics and especially the ECSZ by Hearn and Humphreys (1998), Eckert and Connolly (2004) and McCaffrey (2005) account for fault slips, block displacements and block rotations and yield good matches of the WUS strain field and derived stress orientations. These models are capable of improving the understanding of WUS dynamics and kinematics but, since they lack the implementation of gravitational potential energy differences ( $\Delta GPE$ ), do not yield information on absolute stress magnitudes and dependent parameters.

3D models (for example Stein, 1999; Parsons et al., 1999; and Freed and Lin, 2002) have been used to model the static and dynamic stress transfer due to major earthquakes on segments of the SAF. Calculating the difference in Coulomb failure stress ( $\Delta CFS$ ), conclusions are drawn on whether faults are brought closer to failure or not. However, these models only account for stress changes due to co-seismic slip on specific fault segments and body forces are not implemented. Since only stress differences are considered, these kinds of analysis only account for the relative change in stress in respect to an arbitrarily chosen initial state of stress. Hence, these models are not capable of yielding information on the absolute in-situ state of stress.

Flesch et al. (2000, 2007), Humphreys and Coblenz (2007) use numerical models to simulate the composition of the state of stress in the WUS. Their models account for the various contributions ( $\Delta GPE$ , plate boundary forces and basal tractions) to the state of stress and help to improve the understanding of the relative impact/influence of these contributions. However, these models represent only a pseudo 3D approach where stresses due to  $\Delta GPE$  are averaged over the crustal thickness. Furthermore, structural inhomogeneities (faults) are not included. Thus, although modeled stress orientations provide a good fit to independent data, derived stress magnitudes represent a crustal average and must be carefully used when subsequent conclusions are based on them.

The 3D FE modeling approach by Li and Liu (2006) associates stress and strain changes in southern California to the complexity of the geometry of the SAF, especially in the Big Bend region. They show that active faults and seismicity in the ECSZ might be directly related to the geometry of the SAF, as observed by Du and Aydin (1996) and confirmed in this study. However, Li and Liu (2006) similar to the  $\Delta CFS$  studies consider relative stress changes due to tectonic loading and do not consider absolute stress magnitudes.

A comparison to a similar 3D FE modeling approach used by Parsons (2006) points out the importance of how to apply plate boundary forces in 3 dimensions. Parsons investigated the tectonic differential stressing in California and exposed his model to

$\Delta$ GPE and loading conditions simulating the observed surface displacement field. The highest differential stressing rates coincide with regions of greatest seismic energy release in a 200km wide corridor along the plate boundary.  $S_H$  orientation is mostly perpendicular to the strike of the SAF, but significant misfits to independent data occur in the far-field of the SAF. Parsons results indicate that GPS derived surface loads yield appropriate results for short term processes in correlation to recent seismicity, but do not seem to reproduce the 3D state of stress, which has evolved over geologic time scales, correctly. This is consistent with findings of this study where GPS derived boundary conditions on the scale of the ECSZ fail to reproduce the observed state of stress in the ECSZ.

As mentioned above, the state of stress in the ECSZ has been investigated using 2D models (Hearn and Humphreys, 1998; Eckert and Connolly, 2004) or by using 3D models studying the coseismic, postseismic and interseismic stress changes using Coulomb failure stress analysis (e.g. Freed et al., 2007). As discussed above these models are not capable of yielding information on the absolute in-situ state of stress.

Further studies on the state of stress in the ECSZ are based on specific local analysis of earthquake focal mechanisms and fault slip data (Zoback, 1989) or a local state of stress within the ECSZ is inferred from a variety of data (e.g. Monastero et al., 2002, Unruh et al., 2002). The deductions from these studies may be applicable for the general state of stress in the ECSZ, but in detail they are only valid for specific regions and do not give a consistent result for the entire ECSZ state of stress.

In summary, the various modeling studies published to date have focused on one specific purpose and are not capable of integrating several types of analysis. Whilst these studies might include more sophisticated rheological parameters (e.g. Parsons, 2006) or account for total crustal thickness variations and basal tractions (e.g. Flesch et al., 2000, 2007; Humphreys and Coblenz, 2007) none of these studies successfully reproduces the complete 3D state of stress in the WUS, which is consistent both in magnitude and orientation.

In contrast, the modeling approach followed in this study yields a 3D state of stress that matches independent data both for magnitudes and orientations. The derived tectonic regimes match observations for the various tectonic provinces of the WUS. It is worth emphasizing how well, even with the clearly limiting assumptions of neglecting total crustal thickness variations (SAF scale) and basal tractions (all scales) and the implementation of linear elastic rheologies for all models, the modeling results calibrate to the independent data available.

Furthermore, the integration of the SAF scale and the ECSZ scale models illustrates the importance of plate boundary forces transferring increased horizontal stresses via the bending geometry of the SAF into the ECSZ. Hence, a fundamental understanding of the transitional state of stress in the ECSZ can only be obtained when such effects are considered and accounted for. This deduction is clearly valid for a region where anything more than minor geometric variations exist. Thus numerical modeling of the state of stress requires care and a thorough assessment of relevant boundary conditions and processes at all relevant scales. The main conclusion to arise for the ECSZ is that it's transitional state of stress is due to the bending geometry of the SAF whereby the higher convergence

between the Pacific Plate and the continent causes compressional stresses, and transfers increased horizontal stresses into the ECSZ. In response to the increased stresses, strain energy is transferred and thus the ECSZ accommodates 25% of relative plate motion (Figure 9.2).

The fully integrated and calibrated modeling study of the WUS at both the SAF scale and the ECSZ scale furthermore enables subsequent “case” studies. For example, the SAF scale model provides as an excellent base for a submodel investigating the state of stress in the southern ECSZ in the Mojave Block where several large earthquakes occurred (Landers earthquake  $M_w$  7.3, 1992; Hector Mine earthquake  $M_w$  7.1, 1999). Consequently the much better (higher model resolution, total crustal thickness) ECSZ model can be used as a global model for specific local “submodeling” stress analysis, e.g. in the Death Valley or Panamint Valley.

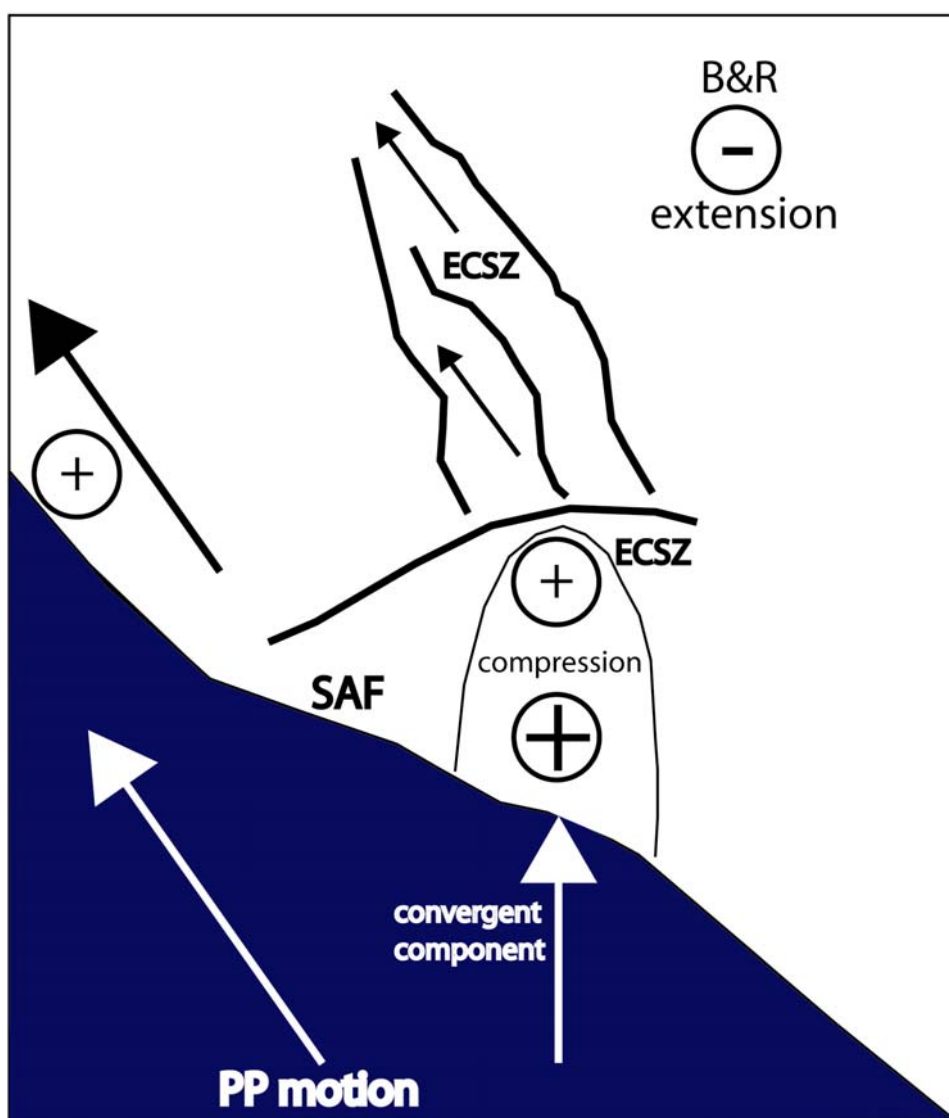


**Figure 9.2:** The higher convergence between the Pacific Plate and the continent at the bending segment of the SAF causes compression (+), i.e. increased horizontal stresses and thus strain is transferred into the ECSZ. This process causes the ECSZ to accommodate up to 25% of relative plate motion.

### 9.5.2. Coso Range scale

Modeling studies on the Coso Range and the Coso Geothermal Field are restricted to analogue sandbox models by Dooley and McClay (1997, 2003). These models provide great detail for analyzing the kinematic behavior of the releasing bend setting of the Coso Range. The agreement between the fault evolution in the analogue models and the real fault distribution and fault behavior is remarkable and, together with the applied boundary conditions, conclusions on the present state of stress can be made. The main drawback of such types of analysis is that no absolute stress magnitudes can be obtained to investigate processes or parameters dependent on the state of stress.

Analysis of the state of stress in the Coso Range is conducted by a variety of analysis (e.g. Roquemore, 1980; Feng and Lees, 1998; Unruh et al., 2002; Sheridan and Hickman, 2004; Davatzes and Hickman, 2006), all concluding that the Coso Range is characterized by NNE compression and WNW extension in a transitional state of stress between extension and strike-slip tectonics. The modeled state of stress agrees with the independent data and predicts strike-slip tectonics near surface and transtensional tectonics with increasing depth. The close correlation of the modeled tectonic regimes to R-ratio derived RSR values from focal mechanism analysis (Feng and Lees, 1998) and stress estimates for  $S_H$  (Sheridan and Hickman, 2004) illustrates that the state of stress is significantly influenced by the boundary conditions inferred from large scale tectonic loading.

The advantage of 3D FEA is that it allows the implementation of complex fault geometries, especially at the scale of the CGF, and material parameters and thus enables the analysis of their influence on the state of stress and vice versa. Due to the thorough model calibration the state of stress represents a close approximation to the complete 3D crustal state of stress and thus an analysis on stress dependent 2<sup>nd</sup> order fracture generation and mean stress associated fluid flow pathways is possible. Figure 9.3 shows the inferred fluid flow regime for the Coso Range and the Coso Geothermal Field.

The derivation of fluid flow pathways along 2<sup>nd</sup> order structures, as conducted in this study, is consistent with other studies which have shown that faults favorably oriented for slip in the stress field tend to be the most active flow pathways (Barton et al., 1995, Finkbeiner et al., 1997). Similar analysis inferring possible fluid flow pathways associated to fractures in stressed rocks are based on the application of slip and dilation tendency, e.g. the analysis conducted for the Yucca Mountain repository (Ferrill et al., 1999). This analysis is based on stress measurements at Yucca Mountain (Stock et al., 1985) and slip and dilation tendency are inferred for a 3D fault model. However, the main drawback of the Yucca Mountain analysis is that it is based on homogeneous stress magnitude measurements. An inhomogeneous state of stress, as calculated in 3D FE models, is much more appealing, since depth or density dependent stress variations are accounted for.

Other analysis types inferring fluid flow along active faults are based on the actual stress and fracture measurements in specific boreholes (Barton et al., 1995, Sheridan et al., 2003) and do not give indications about the regional fluid flow pattern as long as numerous spatially distributed measurements have not been undertaken.

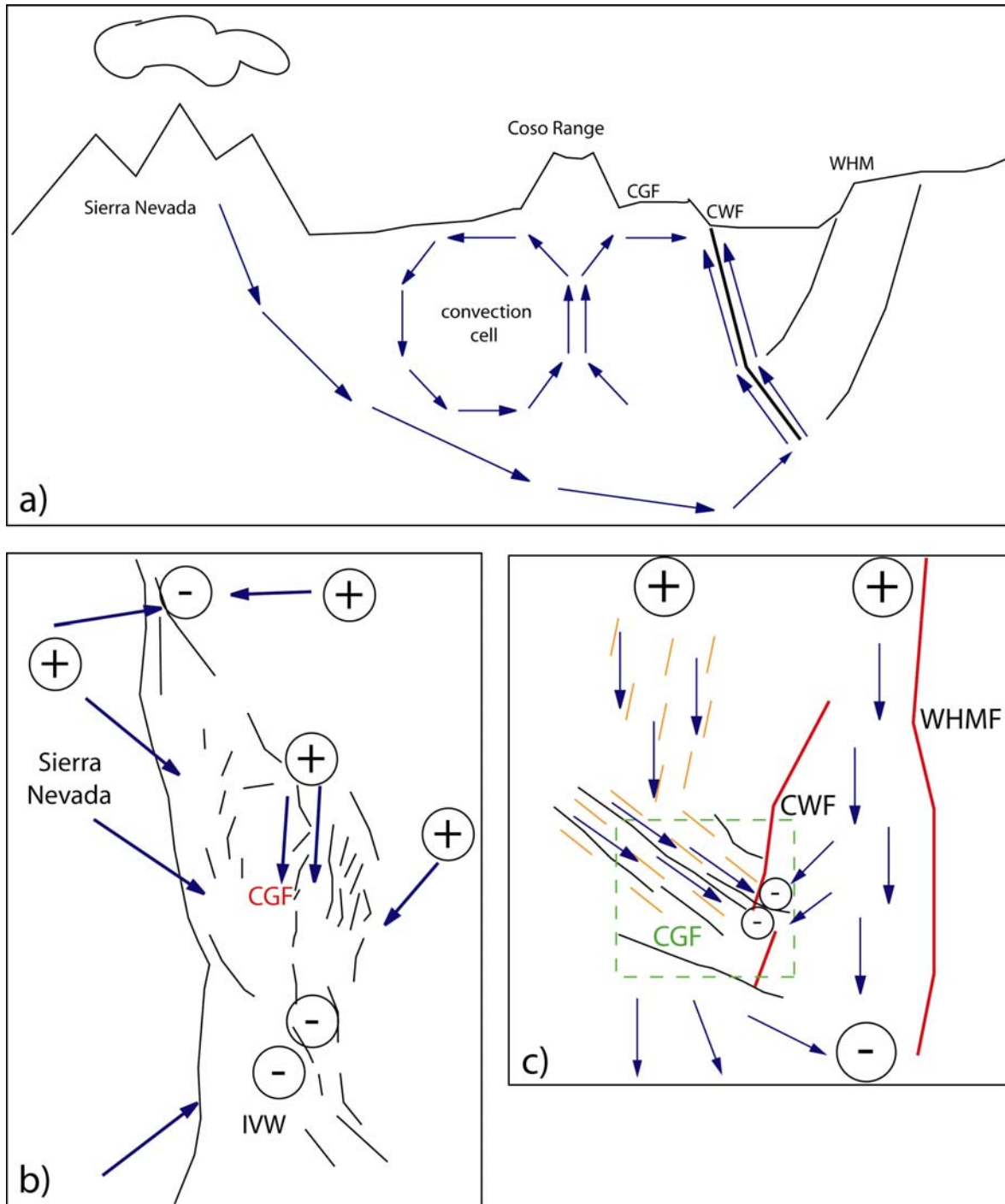


**Figure 9.6: Inferred fluid flow regimes for the Coso Range and the geothermal system.** a) Vertical, regional profile inferring the regional source of cold fluids in the Sierra Nevada. These fluids migrate eastbound until under the geothermal system they are heated and transported upwards along the major active structures. Within the geothermal system fluids are probably transported by convection processes. b) Map-view of the regional fluid flow regime. (+) indicates high pressure, (-) low pressure. Regional source of fluids is the Sierra Nevada. Within the Coso Range fluids migrate southwards through the CGF into the IVW. c) Local fluid flow regime inferred for the region of the CGF. Fluids migrate southwards from the north along NNE oriented 2<sup>nd</sup> order fractures (orange ticks), until they are redirected to flow ~SE towards the mean stress low at the southern tip of the Coso Wash Fault (CWF). This flow direction is favored along both predicted and mapped structures.

## 9.6. Main conclusions

This modeling study provides the following set of main conclusions:

- Initial equilibrated gravitational state of stress accounting for increasing horizontal stresses near surface is necessary when absolute state of stress is modeled.
- Crustal state of stress in California is the result of the interaction between gravitational potential energy differences and plate boundary forces.
- Pacific Plate motion is the main driving force for a distinct regional stress field.
- Bending geometry of the San Andreas Fault (SAF) transfers increased horizontal stresses into the Eastern California Shear Zone (ECSZ), i.e. causes strain energy release to accommodate part of the relative plate motion.
- Insensitivity of  $S_H$  orientations to the coefficient of friction indicates that  $S_H$  orientation data is not an adequate approach for inferring the strength of the SAF.
- ECSZ has consistent state of stress, characterized by transtensional tectonic regimes with the major active faults being situated in corridors of strike-slip tectonics.
- The influence of the SAF geometry by using the ABAQUS submodeling technique is necessary to generate the observed state of stress in the ECSZ.
- State of stress in the Coso Range is characterized by strike-slip tectonics near surface and transtensional tectonics with increasing depth.
- Correlation of Fracture Potential (FP) and seismicity distribution in the Coso Range – Indian Wells Valley region shows that the Coso releasing bend is a region of active fracturing corresponding to tectonic boundary forces.
- Predicted 2<sup>nd</sup> order shear fractures align with mapped structures in the area of the Coso Geothermal Field (CGF) and thus fracturing processes in the CGF may represent fault reactivation and/or fracture growth processes.
- In the area of the CGF fluids migrate from the north into the system and then flow south-eastwards to the Coso Wash Fault. Fluid directions are probably redirected along 2<sup>nd</sup> order structures within the CGF.
- CGF East Flank expansion is favorably situated for fluid production.
- In general, the predicted 2<sup>nd</sup> order and mapped structures align with the predicted fluid flow pattern indicating the strong influence of fractures for optimal fluid migration.

## 9.7. Drawbacks and improvements

Although the modeling approach determined during the work reported in this thesis yields good agreements to independent stress orientations and magnitudes, several assumptions and limitations of the different models provide room for improvements.

At the SAF scale there is no implementation of the Moho surface. Including total crustal thickness variations might further resolve the influence of  $\Delta GPE$  on the WUS state of stress. Unfortunately, current Moho data for the WUS has either a very coarse resolution (e.g. 2x2 degree for crust2.0, Bassin et al., 2000) or is restricted to specific areas (e.g. Richards-Dinger, 1997; Zhu and Kanamori, 2000; Fliedner et al., 2000) and different datasets show discrepancies in the order of kilometers. Using presently available Moho

maps would result in either an implementation in which the Moho has little influence on  $\Delta GPE$  or one in which the data used for modeling is an interpolation and thus likely to have significant errors.

Another limitation of the models, in particular for analyzing shear stresses on the SAF, is the use of a homogeneous linear elastic rheology for the upper crust. Accounting for crustal strength profiles (Kohlstedt et al., 1995) and thus using an upper elastic and a lower viscoelastic crust is generally considered a more appropriate approach for modeling lithospheric stresses. Implementing a model with a viscoelastic rheology that maintains the dominant Californian topography proved to be a very time consuming task that was not achieved during the coarse of this study. It is recommended that this topic should remain a focus of ongoing research.

When considered out of context, the model of the Coso Range shows a poor correlation of Fracture Potential (FP) and seismicity in the area of the CGF. The dense seismic clusters within the Coso Range are mainly associated to fluid circulation associated with production in the CGF (e.g. Feng and Lees, 1998). This shows that the modeled state of stress represents conditions prior to production at the CGF. Since these production related fluid pressure changes are not included in the models, the state of stress obtained is considered to represent conditions prior to production at the CGF. In order to analyze the present day induced seismicity completely, a fully coupled reservoir effective stresses modeling study using poro-elasto-plastic materials would have to be conducted. Together with existing reservoir pressures this would significantly increase the FP (reduce effective stress), whilst maintaining the tectonically induced differential stress in the area of the CGF.

Furthermore, additional driving mechanisms for the fluid flow, such as thermal convection processes, would significantly improve the knowledge of fluid pathways and provide a better understanding of the geothermal system.

## 9.8. Summary and concluding remarks

The modeling approach presented in this thesis is based on an initial gravitational state of stress which is subjected to tectonic loads. The resulting state of stress and derived parameters are critically dependent on the ratio of horizontal to vertical stress. This emphasizes the inherent need of a Sheorey type calibration for modeling realistic horizontal stresses. Numerical models not accounting for gravitationally equilibrated initial stresses based on Sheorey's model (1994) or similar models and which have not been thoroughly calibrated for both stress magnitude and orientation, must be carefully used when subsequent parameters are analyzed. This implies that any potential process and/or forces that may contribute to the stress state must be carefully analyzed before being neglected. The fully integrated and calibrated FE modeling approach for all scales presented yields a realistic crustal state of stress and thus consistent analysis of present tectonic regimes, fault parameters and fracture potential are enabled.

The modeled state of stress represents a close approximation of the complete 3D crustal state of stress. Modeling the complete state of stress is especially relevant for the analysis of the Coso Geothermal Field of 2<sup>nd</sup> order fracture networks and mean stress

associated fluid flow pathways. Both likelihood, distribution and orientation of second order fractures as well as the mean stress derived fluid flow vectors are directly dependent on the complete state of stress. This analysis cannot be correctly accomplished in a state of stress that does not correspond to in-situ stress conditions.

The main advantage of the FE modeling approach presented in this thesis is that it can be regarded as a multi-purpose approach. The modeling procedure enables subsequent analysis from regional tectonic to small scale processes. The modeled state of stress can be used for a variety of analysis: e.g. stress based fracture potential, slip tendency, shear and normal stress on specific fault surfaces or coulomb failure stress. The type of modeling and analysis presented shows a great potential for improvements and further, more specific types of analysis, in particular at a local scale such as the Coso Range. The results presented in this thesis couple stresses induced by tectonic loading to possible 2<sup>nd</sup> order fracture generation or reactivation and derived fluid flow pathways. Further fields of study may be the combination of the modeled state of stress with poro-elasticity. This would enable the modeling of effective stresses, i.e. more realistic FP for the CGF, with permeabilities both for fractures and rock matrix. Additionally, fluid budgets could be handled by applying steady-state or transient fluid flow boundary conditions. In order to achieve a more complete understanding of the geothermal system, dilation tendency analysis may provide additional indications on fracture permeability directions and thermal convection processes may add a different driving mechanism for the fluid flow.

In summary, this thesis demonstrates that using relatively simple elastic 3D FE analysis is of successfully simulating the contemporary 3D crustal state of stress at multiple scales. In combination with other methods of study (seismicity, geomagnetics, geothermal, geodetics), a better understanding of in-situ regional and local tectonics and associated processes is now possible.

## 10. References

- ABAQUS/Standard User's manual, Abaqus Inc.
- Anderson, E.M., 1905. The dynamics of faulting, Edinburgh Geol. Soc. Transactions 8 (3), 387-402.
- Atwater, T., and J. Stock, 1998. Pacific-North America plate tectonics of the Neogene southwestern United States – an update, Int. Geol. Review, v.40, 375-402.
- Barton, C.A., M.D. Zoback, and D. Moss, 1995. Fluid flow along potentially active faults in crystalline rock, Geology, 23 (8), pp. 683-686.
- Bassin, C., Laske, G. and Masters, G., 2000. The Current Limits of Resolution for Surface Wave Tomography in North America, EOS Trans AGU, 81, F897.
- Beanland, S. and Clark, M.M., 1987. The Owens Valley fault zone, eastern California, and surface rupture associated with the 1872 earthquake, Seismol. Res. Lett., 58, 32.
- Beanland, S. and Clark, M.M., 1994. The Owens Valley fault zone, eastern California, and surface rupture associated with the 1872 earthquake, U.S. Geol. Surv. Bull., 1982, pp. 29.
- Bellier, O. and Zoback, M.L., 1995. Recent state of stress change in the Walker Lane zone western basin and Range Province-USA. Tectonics 14, pp. 564–593.
- Bennett, R.A., Wernicke, B.P., Davis, J.L., Elósegui, P., Snow, J.K., Abolins, J., House, M.A., Stirewalt, G.L. and Ferrill, D.A., 1997. Global Positioning System constraints on fault slip rates in the Death Valley region, California and Nevada, Geophys. Res. Lett., Vol.24, No.23, p. 3073-3076.
- Bennett, R.A., B. P. Wernicke, N. A. Niemi, A. M. Friedrich, and J. L. Davis, 2003. Contemporary strain rates in the northern Basin and Range province from GPS data, Tectonics, Vol. 22, No.2, 1008, doi:10.1029/2001TC001355.
- Bhattacharyya, J., and Lees, J.M., 2002. Seismicity and seismic stress in the Coso Range, Coso geothermal field, and Indian Wells Valley region, southeast-central California, Geological Society of America, Memoir 105, p. 243-258.
- Bohannon, R.G., and T. Parsons, 1995. Tectonic implications of post-30 Ma Pacific and North American relative plate motions, *GSA Bulletin*, v.107, no.8, 937-959.
- Bott, M.H.P., 1959. The mechanics of oblique slip faulting. Geological Magazine 96, 109-117.
- Brudy, M., M. D. Zoback, K. Fuchs, F. Rummel, and J. Baumgärtner, 1997. Estimation of the complete stress tensor to 8km depth in the KTB scientific drill holes: Implications for crustal strength, J. Geophys. Res., 102, 18,453-18,475.
- Brune, J. N., T. L. Henyey, and R. F. Roy, 1969. Heat flow, stress and rate of slip along the San Andreas fault, California, J. Geophys. Res., 74, 3821-3827.
- Buchmann, T. and P.T. Connolly, 2007. “Contemporary kinematics of the Upper Rhine Graben: a 3D finite element approach.” Global Planetary Change, in press.
- Byerlee, J. D., 1978. Friction of rocks, Pure Appl. Geophys., 116, 615-626.
- Chéry, J., M. D. Zoback, and R. Hassani, 2001. An intergrated mechanical model of the San Andreas Fault in central and northern California, , J. Geophys. Res., 106, 22,051-22,066.

- Chéry, J., M. D. Zoback, and S. Hickman, 2004. A mechanical model of the San Andreas fault and SAFOD Pilot Hole stress measurements, *Geophys. Res. Lett.*, Vol. 31, L15S13, doi:10.1029/GL019521.
- Chester, F. M., J. P. Evans, and R. L. Biegel, 1993. Internal structure and weakening mechanisms of the San Andreas Fault, *J. Geophys. Res.*, 98, 771-786.
- Connolly, P.T., 1996. Prediction of fluid pathways and secondary structures associated with dilatational jogs. Unpubl. Ph.D thesis, Imperial College, London.
- Connolly, P.T. and J.W. Cosgrove, 1999. Prediction of fracture induced permeability and fluid flow in the crust using experimental stress data. *AAPG Bull.* V.85, No.5, P. 757-777.
- Davatzes, N.C., and S.H. Hickman, 2006. Stress and faulting in the Coso geothermal Field: Update and recent results from the East Flank and Coso Wash, Proceedings 31st Workshop on Geothermal Reservoir Engineering, Stanford University, SGP-TR-179.
- Davis, R.O., and A.P.S. Selvadurai, 1996. Elasticity and Geomechanics, Cambridge University Press, Cambridge.
- Davis, R.O., and A.P.S. Selvadurai, 2002. Plasticity and Geomechanics, Cambridge University Press, Cambridge.
- De Mets C., R.G. Gordon, D.F. Argus, S. Stein, 1990. Current plate motions. *Geophys. J. Int.* (101) 425-478.
- Dixon, T.H., Robaudo, S., Lee, J. and Reheis, M.C., 1995. Constraints on present-day Basin and Range deformation from space geodesy, *Tectonics*, vol. 14, no. 4, p. 755-772.
- Dixon, T.H., M. Miller, F. Farina, H. Wang and D. Johnson, 2000. Present-day motion of the Sierra Nevada block and some tectonic implications for the Basin and Range province, North American Cordillera, *Tectonics*, 19, p. 1-24.
- Dokka, R.K. and C.J. Travis, 1990. Role of the Eastern California shear zone in accommodating Pacific-North American plate motion, *Geoph. Res. Lett.*, 17, p. 1323-1326.
- Dooley, T., and K. McClay, 1997. Analogue modeling of pull-apart basins, *American Association of Petroleum Geologists*, v.81, p. 1804-1826.
- Dooley, T., McClay, K. and Monastero, F.C., 2003. Scaled sandbox modelling of transtensional pull-apart basins – applications to the Coso Geothermal System, Eighth annual Geothermal Program Office technical symposium, Davis, California.
- Du, Y., and A. Aydin, 1996. Is the San Andreas big bend responsible for the Landers earthquake and the eastern California shear zone? *Geology*, v.24, no.3, 219-222.
- Duffield, A.W., Bacon, C.R. and Dalrymple, G.B., 1980. Late Cenozoic volcanism, geochronology, and structure of the Coso Range, Inyo County, California, *J. Geophys. Res.*, 85, p. 2381-2404.
- Eckert, A., and P.Connolly, 2004. 2D finite element modelling of regional and local fracture networks in the Eastern California Shear Zone and Coso Range, California USA, *GRC Transactions*, Vol. 28, 643-648.

- Eckert, A. and P. Connolly, 2005. Prediction of 3D crustal fracture networks and fluid paths in the Coso Range using a mechanistic approach based on finite element analysis. Contract N68936-03-C-0024, End Phase I report.
- Eisbacher, G., 1996. Einführung in die Tektonik, Enke Verlag, Stuttgart.
- Engelder, T., 1993. Stress regimes in the lithosphere, Princeton University Press, Princeton.
- Feng, Q. and J.M. Lees, 1998. Microseismicity, stress, and fracture in the Coso geothermal field, California. *Tectonophysics* 289, p.221-238.
- Ferrill, D.A., J. Winterle, G. Wittmeyer, D. Simms, S. Colton, and A. Armstrong, 1999. Stressed rock strains groundwater at Yucca Mountain, Nevada, *GSA Today*, Vol.9, no.5, p1-8.
- Fialko Y.A., and M. Simmons, 2000. Deformation and seismicity in the Coso geothermal area, Inyo County, California: Observations and modeling using satellite radar interferometry, *J. Geophys. Res.*, v.105, p. 21,781-21,794.
- Finkbeiner, T., C.A. Barton, and M.D. Zoback, 1997. Relationship among in-situ stress, fractures and faults, and fluid flow: Monterey Formation, Santa Maria Basin, California, *AAPG Bulletin*, v.81, p.1975-1999.
- Fitzens, D. D., and S. A. Miller, 2004. New insights on stress rotations from a forward regional model of the San Andreas fault system near its Big Bend in southern California, *J. Geophys. Res.*, 109, B08404, doi:10.1029/2003JB002890.
- Fleitout, L., P. England, and N. Kuznir, 1991. The sources of lithospheric tectonic stresses, *Phil. Trans. R. Soc. Lond. A*, Vol. 337, No. 1645, 73-81.
- Flesch, L. M., W. E. Holt, A. J. Haines, and B. Shen-Tu, 2000. Dynamics of the Pacific-North American Plate Boundary in the Western United States, *Science*, Vol. 287, 834-836.
- Flesch, L. M., W. E. Holt, A. J. Haines, L. Wen, and B. Shen-Tu, 2007. The dynamics of western North America: stress magnitudes and the relative role of gravitational potential energy, plate interaction at the boundary and basal tractions, *Geophys. J. Int.*, in press.
- Fliedner, M.M., S.L. Klemperer, and N.I. Christensen, 2000. Three-dimensional seismic model of the Sierra Nevada arc, California, and its implications for crustal and upper mantle composition, *J. of Geophys. Res.*, 105, B5, 10,899-10,921.
- Freed, A.M., and J. Lin, Accelerated stress buildup on the southern San Andreas fault and surrounding regions caused by Mojave Desert earthquakes, *Geology*, 30, 571-574, 2002.
- Freed, A.M., A. Syed Tabrez, and R. Bürgmann, 2007. Evolution of stress in Southern California for the past 200 years from coseismic, postseismic and interseismic stress changes, *Geophys. J. Int.*, Vol. 169, no.3, pp.1164-1179(16).
- Frohlich, C., 1992. Triangle diagrams: Ternary graphs to display similarity and diversity of earthquake focal mechanisms, *Physics of the Earth and Planetary Interiors*, v.75, p. 193-198.

- Fuis, G.S., T. Ryberg, N.J. Godfrey, D.A. Okaya, and J.M. Murphy, 2001. Crustal structure and tectonics from the Los Angeles basin to the Mojave desert, southern California, *Geology*, v.29, no.1, 15-18.
- Gan, W., Svarc, J.L., Savage, J.C., and Prescott, W.H., 2000. Strain accumulation across the Eastern California Shear Zone at latitude 36°30'N, *J. Geophys. Res.*, 105, No. B7, p.16229-16236.
- Hardebeck, J.L., and E. Hauksson, 1999. Role of fluids in faulting inferred from stress field signatures, *Science*, 285, 236-239.
- Hardebeck, J. L., and E. Hauksson, 2001. Crustal stress field in southern California and its implications for fault mechanics, *J. of Geophys. Res.*, 106, 21,859-21,882.
- Hardebeck, J. L., and A. J. Michael, 2004. Stress orientations at intermediate angles to the San Andreas Fault, California, *J. Geoph. Res.*, 109, B11303, doi :10.1029/2004JB003239.
- Hearn E., and Humphreys E. D., 1998. Kinematics of the southern Walker Lane Belt and motion of the Sierra Nevada block, California, *J. Geophys. Res.*, Vol. 103, No. B11, 27,033-27,049.
- Heidbach, O. et al. (eds.), 2007. The World Stress Map – Release 2005, Commission for the Geological Map of the World, Paris.
- Hickman, S., and M. D. Zoback, 2004. Stress orientations and magnitudes in the SAFOD Pilot Hole, *Geophys. Res. Lett.*, 31, L15S12, doi: 10.1029/2004/GL020043.
- Hickman, S. H., M. D. Zoback, and W. L. Ellsworth, 2005. Structure and composition of the San Andreas Fault Zone at Parkfield: Initial results from SAFOD Phases 1 and 2, *Eos Trans. AGU*, 86(52), Fall Meet. Suppl.,Abstract T23E-05.
- Humphreys, E.D., and D.D. Coblenz, 2007. North America dynamics and western U.S. tectonics, *Rev. Geophys.*, in press.
- Jaeger, J.C., N.G.W. Cook, and R.W. Zimmerman, 2007. *Fundamentals of Rock Mechanics*, 4<sup>th</sup> edition, Blackwell Publishing.
- Jennings, C. W., 1994. Fault activity map of California and adjacent area, with locations and ages of recent volcanic eruptions, *Geol. Data Map 6*, Calif. Div. Of Mines and Geol., Sacramento.
- Jones, C.H., G.L. Farmer, and J. Unruh, 2004. Tectonics of Pliocene removal of lithosphere of the Sierra Nevada, California, *GSA Bulletin*, v.116, no.11/12, 1408-1422.
- Jones, C. H., J. R. Unruh, and L. J. Sonder, 1996. The role of gravitational potential energy in active deformation in the southwestern United States, *Nature*, Vol. 381, 37-41.
- Kohlstedt, D.L., B. Evans, and S.J. Mackwell, 1995. Strength of the lithosphere: Constraints imposed by laboratory experiments, *J. Geophys. Res.*, VOL. 100, B9, 17,587-17,602.
- Lachenbruch, A.H., and J.H. Sass, 1992. Heat flow from Cajon Pass, fault strength, and tectonic implications, *J. Geoph. Res.*, 97, 4995-5015.
- Le, K., Lee, J., Owen, L.A., and Finkel, R., 2007. Late Quaternary slip rates along the Sierra Nevada frontal fault zone, California: Slip partitioning across the western margin

- of the Eastern California Shear Zone-Basin and Range Province: Geological Society of America Bulletin, v. 119, p. 240–256; doi: 10.1130/B25960.1.
- Lees, J. M. and H. Wu, 2000. Poisson's ratio and porosity at Coso Geothermal Area, California. *J. Volc. Geotherm. Res.* 95(1-4), 157-173.
- Li, Q., and M. Liu, 2006. Geometrical impact of the San Andreas Fault on stress and seismicity in California, *Geophys. Res. Lett.*, 33, L08302, doi : 10.1029/2005GL025661.
- Liu, M., Y. Yang, Q. Li, and H. Zhang, 2007. Parallel computing of multi-scale continental deformation in the Western United States, *Physics of the Earth and Planetary Interiors*, v.163, p. 35-51.
- McCaffrey, R., 2005. Block kinematics of the Pacific-North America plate boundary in the southwestern United States from inversion of GPS, seismological and geologic data, *J. Geoph. Res.*, Vol. 110, B07401, doi :10.1029/2004JB003307.
- McClusky, S.C., S.C. Bjornstad, B.H. Hager, R.W. King, B.J. Meade, M.M. Miller, F.C. Monastero and B.J. Souter, 2001. Present day kinematics of the Eastern California Shear Zone from a geodetically constrained block model.", *Geophys. Res. Lett.*, v.28, 3369-3372.
- Melosh, H.J., and A. Raefsky, 1981. A simple and efficient method for introducing faults into finite element computations, *Bull. Seismol. Soc. Am.*, 71, 1391-1400.
- Melosh, H.J., 1996. Dynamical weakening of faults by acoustic fluidization, *Nature*, 379, 601-606.
- Miller, M.M., D.J. Johnson, T.H. Dixon, and R.K. Dokka, 2001. Refined kinematics of the eastern California shear zone from GPS observations, *J. Geophys. Res.*, 106, B2, 2245-2263.
- Monastero, F.C., J.D. Walker, A.M. Katzenstein, and A.E. Sabin, 2002. Neogene evolution of the Indian Wells Valley, east-central California. Pp. 199-228 in Glazner, Allen F., Douglas Walker, and John M. Bartley, 2002. Geologic evolution of the Mojave Desert and southwestern Basin and Range. Memoir 195. Boulder, CA: Geological Society of America, 2002.
- Monastero, F.C., A.M. Katzenstein, J.S. Miller, J.R. Unruh, M.C. Adams and K. Richards-Dinger, 2005. The Coso geothermal field: A nascent metamorphic core complex. *GSA Bulletin*, v.117, no.11/12, 1534-1553.
- Mount, V. S., and J. Suppe, 1987. State of stress near the San Andreas Fault: Implications for wrench tectonics, *Geology*, v.15, 1143-1146.
- Müller, B., V. Wehrle, S. Hettel, B. Sperner, and K. Fuchs, 2003. A new method for smoothing oriented data and its application to stress data, in: Ameen, M. (ed.) Fracture and in-situ stress characterization of hydrocarbon reservoirs, *Geol. Soc. Lond. Spec. Publ.*, 209, 107-126.
- Oliver, J., 1986. Fluids expelled tectonically from orogenic belts: Their role in hydrocarbon migration and other geologic phenomena, *Geology*, v.14, 99-102.
- Parsons, T., R. S. Stein, R. W. Simpson and P. A. Reasenberg, 1999. Stress sensitivity of fault seismicity: A comparison between limited-offset oblique and major strike-slip faults, *J. Geophys. Res.*, 104, pp. 20,183-20,202.

- Parsons, T., 2006. Tectonic stressing in California modeled from GPS observations, *J. Geophys. Res.*, 111, B03407, doi :10.1029/2005JB003946.
- Price, M., 1985. Introducing groundwater: London, Allen and Unwin, 195p.
- Price, N.J., 1966. Fault and joint development in brittle and semi-brittle rock, Pergamon Press, Oxford.
- Price, N.J. and J.W. Cosgrove, 1990. Analysis of geological structures. Cambridge University Press, Cambridge, pp. 502.
- Provost, A.-S., and H. Houston, 2003. Stress orientations in northern and central California: Evidence for the evolution of frictional strength along the San Andreas plate boundary system, *J. Geophys. Res.*, 108(B3), 2175, doi :10.1029/2001JB001123.
- Ramsay, J.G., 1967. Folding and fracturing of rocks. New York, McGraw-Hill, 568 p.
- Ramsay, J.G. and R.J. Lisle, 2000. The techniques of modern structural geology Vol.3, Academic Press, London.
- Ranalli, G., 1995, Rheology of the earth, Chapman & Hall, London.
- Rice J.R., 1992. Fault stress states, pore pressure distributions, and the weakness of the San Andreas Fault, in Fault Mechanics and Transport Properties of Rocks, edited by B. Evans, and T.-F. Wong, pp. 475-503, Academic, San Diego, Calif.
- Richards-Dinger, K.B., and P.M. Shearer, 1997. Estimating crustal thickness in southern California by stacking PmP arrivals, *J. Geophys. Res.*, 102, 15,211-15,224.
- Richardson, R.M., and L.M. Reding, 1991. North American plate dynamics, *J. Geophys. Res.*, 96, 12,201, 12,223.
- Roquemore, G., 1980. Structure, tectonics, and stress field of the Coso Range, Inyo County, California, *J. Geophys. Res.*, 85, p. 2434-2440.
- Rutqvist J, Birkholzer J, Cappa F, Oldenburg C, Tsang C, 2006. Shear-slip analysis in multiphase fluid-flow reservoir engineering application using Tough-Flac, in: TOUGH Symposium 2006, pp. 1-9, Lawrence Berkeley National Laboratory, Berkeley, California.
- Savage, J.C., Lisowski, M. and Prescott, W.H., 1990. An apparent shear zone trending north-northwest across the Mojave Desert into Owens Valley, Eastern California, *Geophys. Res. Lett.*, Vol. 17, No. 12, p. 2113-2116.
- Scholz, C. H., 2000. Evidence for a strong San Andreas fault, *Geology*, 28, 163-166.
- Sheridan, J., K. Kovac, P.E. Rose, C. Barton, J. McCulloch, B. Berard, J.M. Moore, S. Petty, and P. Spielman, 2003. In situ stress, fracture and fluid flow analysis – East Falnk of the Coso Geothermal Field, Proceedings 28<sup>th</sup> Workshop on Geothermal Reservoir Engineering, Stanford University, 16p.
- Sheridan, J.M., and S.H. Hickman, 2004. In situ stress, fracture, and fluid flow analysis in well 38C-9: an enhanced geothermal system in the Coso Geothermal Field, Proceedings 29<sup>th</sup> Workshop on Geothermal Reservoir Engineering, Stanford Univ., 8p.
- Sheorey, P. R., 1994. A theory for In Situ Stresses in Isotropic and Transversely Isotropic Rock, *Int. J. Rock Mech. Min. Sci. & Geomech. Abstr.* Vol. 31, No.1, 23-34.
- Sibson, R.H., 1990. Faulting and fluid flow. In: Nesbitt, B.E. (ed.) Fluids in tectonically active regimes of the continental crust. Mineralogical Association of Canada, Short Course Notes, 18, 93-132.

- Simpson, R. W., 1997. Quantifying Anderson's fault types, *J. Geophys. Res.*, 102, 17,909-17,919.
- Sonder, L.J., and C.H. Jones, 1999. Western United States extension: How the west was widened, *Annu. Rev. Earth Planet Sci.*, 27, 417-462.
- Stein, R.S., 1999. The role of stress transfer in earthquake occurrence, *Nature*, 402, pp. 605-609.
- Stein, S. and Wysession, M., 2003. An introduction to seismology, earthquakes, and earth structure. Blackwell Publishing, Malden, MA, USA.
- Stock J.M., J.H. Healy, S.H. Hickman, and M.D. Zoback, 1985. Hydraulic fracturing stress measurements at Yucca Mountain, Nevada, and relationship to regional stress field, *J. Geophys. Res.*, v.90, p. 8691-8706.
- Taylor, T.R., and J.F. Dewey, 2006. Triaxial deformation of the brittle crust in transtension: Coso-China Lake region, eastern margin of the Sierra Nevada Microplate, southeastern California, American Geophysical Union, Fall Meeting 2006, abstract #T11C-0452.
- Timoshenko, S., and J.N. Goodier, 1970. Theory of Elasticity (3<sup>rd</sup> ed.), McGraw-Hill Inc., New York.
- Townend J., and M.D. Zoback, 2000. How faulting keeps the crust strong, *Geology*, 28, 399-402.
- Townend J., and M. D. Zoback, 2004. Regional tectonic stress near the San Andreas fault in central and southern California, *Geophys. Res. Lett.*, 31, L15S11, doi:10.1029/2003GL018918.
- Turcotte, D.L., and G. Schubert, Second Edition, 2002. Geodynamics, Cambridge Univ. Press, London.
- Unruh, J., S. Pullammanappallil, B. Honjas, and F. Monastero, 2001. New seismic imaging of the Coso geothermal Field, eastern California. 26<sup>th</sup> Workshop geothermal Reservoir Engineering, Proc. 26, pp.7.
- Unruh, J.R., Hauksson, E., Monastero, F.C., Twiss, R.J. and Lewis, J.C., 2002. Seismotectonics of the Coso-Indian Wells Valley region, California: Transtensional deformation along the southeastern margin of the Sierran microplate, *Geol. Soc. Of America, Memoir* 195, 277-298.
- Unruh, J.R., J. Humphrey, and A. Barron, 2003. transtensional model for the Sierra Nevada frontal fault system, eastern California, *Geology*, v.31, no.4, 327-330.
- Vetter, U. and Ryall, A., 1983. Systematic change of focal mechanism with depth in the Western Great Basin. *Journal of Geophysical Research* 88(B10), 8237-8250.
- Walter, A.W., and Weaver, C. S., 1980. Seismicity of the Coso Range, *J. Geophys. Res.*, 85, p. 2441-2458.
- Wesnousky, S.G., and C. H. Jones, 1994. Oblique Slip, Slip Partitioning, Spatial and Temporal Changes in the Regional Stress Field, and the Relative Strength of Active Faults in the Basin and Range, Western United States, *GEOLOGY*, 22, 1031-1034.
- Wesnousky, S. G., 2005. The San Andreas and Walker Lane fault systems, western North America: transpression, transtension, cumulative slip and the structural evolution of a major transform plate boundary, *Journal of Structural Geology*, 27, 1505-1512.

- Wicks, C., W. Thatcher, F. Monastero and M. Hasting, 2001. Steady-State Deformation of the Coso Range, East-Central California, Inferred from Satellite Radar Interferometry, *J. Geophys. Res.*, 106, pp. 13,769 – 13,780.
- Whitmarsh, R.S., 1998. Geologic map of the Coso Range: Geological Society of America on-line map, doi: 10.1130/1998-whitmarsh-coso.
- Zhang, X, D. J. Sanderson and A.J. Barker, 2002. Numerical study of fluid flow of deforming fractured rocks using dual permeability model. *Geophys. J. Int.*, 151, 452-468.
- Zhu, L., and H. Kanamori, 2000. Moho depth variation in southern California from teleseismic receiver functions, *J. Geophys. Res.*, 105, B2, 2969-2980.
- Zienkiewicz, O.C. and Taylor, R.L., 1994. The finite element method, Vol. 1&2, McGraw-Hill Book Company, London.
- Zoback, M. D., and J. H. Healy, 1992. In situ stress measurements to 3.5km depth in the Cajon Pass scientific research borehole: Implications for the mechanics of crustal faulting, *J. Geophys. Res.*, 97, 5039-5057.
- Zoback, M. D. et al., 1987. New evidence on the state of stress of the San Andreas fault system, *Science*, 238, 1105-1111.
- Zoback, M. L., 1989. State of stress and modern deformation of the northern Basin and Range Province, *J. Geophys. Res.*, 94, 7105-7128.
- Zoback, M. L., 1992. First- and second-order patterns of stress in the lithosphere: The world stress map project, , *J. Geophys. Res.*, 97, 11703-11728.
- Zoback, M. L., and M.D. Zoback, 1989. Tectonic stress field of the continental U.S., in Parkiser, L., and W. Mooney, eds., *Geophysical Framework of the Continental United States*, *Geol. Soc. Amer. Memoir* 172, 523-539.